

DOCTORAL THESIS

---

**A Unified Mathematical Framework  
for Link Budget Analysis and Optimization  
in Satellite Communications Systems**

---

by

**Tony Colin<sup>\*</sup>**

<sup>\*</sup>Chair of Signal Processing  
Institute of Information Technology  
Faculty of Electrical Engineering and Information Technology  
Bundeswehr University Munich

**Doctoral committee**

Chairman: Prof. Dr. Christian Hofmann<sup>\*</sup>  
1. Reviewer: Prof. Dr. Andreas Knopp<sup>\*</sup>  
2. Reviewer: Prof. Dr. Bernd Friedrichs<sup>†</sup>  
3. Reviewer: Prof. Dr. Barry Evans<sup>‡</sup>

<sup>†</sup>Karlsruhe Institute of Technology

<sup>‡</sup>University of Surrey

DECEMBER 2022



DOKTORARBEIT

---

# **A Unified Mathematical Framework for Link Budget Analysis and Optimization in Satellite Communications Systems**

---

**Tony Colin**

Vollständiger Abdruck der von der Fakultät für Elektrotechnik und  
Informationstechnik der Universität der Bundeswehr München zur Erlangung des  
akademischen Grades eines

**Doktor-Ingenieurs  
(Dr.-Ing.)**

genehmigten Dissertation.

## **Promotionsausschuss**

Vorsitzender:	Prof. Dr.-Ing. Christian Hofmann
1. Gutachter:	Prof. Dr.-Ing. Andreas Knopp (Betreuer)
2. Gutachter:	Prof. Dr.-Ing. Bernd Friedrichs
3. Gutachter:	Prof. Dr.-Ing. Barry Evans

Die Dissertation wurde am 02.06.2022 bei der Universität der Bundeswehr München eingereicht  
und durch die Fakultät für Elektrotechnik und Informationstechnik am 16.11.2022 angenommen.

Die mündliche Prüfung fand am 15.12.2022 statt.



# Abstract

---

This thesis addresses two fundamental improvements of satellite link budgets. On the one hand, a refinement of contemporary link budgets is proposed. Impairments crucial to satellite communications systems are characterized mathematically. Within the presented framework, the corresponding carrier-to-impairment power ratio formulas are derived. In particular, the formulas provide a faster, more accurate, and more reliable method of characterization than any other existing approaches. In this way, the assessment of the amplifier distortions contribution in the link budget is enhanced. Moreover, novel expressions for waveform imperfections, filter distortions, and oscillator noise are exposed to complement and further improve today's link budget analyses. Ultimately, all theoretical results are thoroughly validated through numerical simulations.

On the other hand, a resources optimization strategy for next-generation satellite communications systems is proposed. Indeed, ultra high-throughput satellite systems will play an essential role in future 5G-and-beyond networks with sum throughputs passing the symbolic threshold of 1 Tbits/s. Since it is especially well-suited to mobile applications such as aircraft and vessels, this work demonstrates the feasibility of real-time dynamic carrier allocation optimization. An in-depth analysis of the allocation gain, complexity, and accuracy is performed. In the end, it is highlighted that an average capacity increase per user of up to 69.7 Mbits/s can be expected in a typical scenario.



# Kurzfassung

---

Diese Doktorarbeit befasst sich mit zwei grundlegenden Verbesserungen des Satelliten-Link-Budgets. Zum einen wird eine Präzisierung des heutigen Link-Budgets vorgeschlagen, wobei die für Satellitenkommunikationssysteme entscheidenden Störfaktoren mathematisch charakterisiert werden. Innerhalb des vorgestellten Rahmens werden die entsprechenden Formeln für das Leistungsverhältnis zwischen Träger und Störung abgeleitet. Das Berechnungsverfahren bietet eine schnellere, genauere und zuverlässigere Methode zur Charakterisierung als alle bisherigen Ansätze. Auf diese Weise wird die Erfassung des Einflusses von Verstärkerverzerrungen auf das Link-Budget optimiert. Darüber hinaus werden neuartige Modelle für Wellenformstörungen, Filterverzerrungen und Oszillatorrauschen vorgestellt, welche die heutigen Link-Budget-Analysen ergänzen und weiter verbessern. Letztendlich werden alle theoretischen Ergebnisse durch numerische Simulationen gründlich validiert.

Zum anderen wird eine Strategie zur Ressourcenoptimierung für Satellitenkommunikationssysteme der nächsten Generation vorgeschlagen. Satellitensysteme mit ultrahohem Durchsatz werden in zukünftigen 5G Netzen und darauffolgenden Netzwerk-Generationen eine wesentliche Rolle spielen. Der Gesamtdurchsatz dieser Systeme wird die symbolische Schwelle von 1 Tbits/s überschreiten. Diese Arbeit demonstriert die Realisierbarkeit einer dynamischen Echtzeit-Optimierung der Trägerallokation, die sich besonders gut für Mobilitätsanwendungen wie Flugzeuge und Schiffe eignet. Es wird eine eingehende Analyse des Allokationsgewinns, der Komplexität und der Genauigkeit durchgeführt. Abschließend wird gezeigt, dass in einem typischen Szenario eine durchschnittliche Kapazitätssteigerung von bis zu 69.7 Mbits/s pro Nutzer erwartet werden kann.





*Mathematics, rightly viewed, possesses not only truth, but supreme beauty—a beauty cold and austere, like that of sculpture, without appeal to any part of our weaker nature, without the gorgeous trappings of painting or music, yet sublimely pure, and capable of a stern perfection such as only the greatest art can show. The true spirit of delight, the exaltation, the sense of being more than Man, which is the touchstone of the highest excellence, is to be found in mathematics as surely as poetry.*

— Bertrand Russell



# Acknowledgments

---

On the path towards this degree, I had three motivations in mind: The will to contribute to the society and the space industry; the wish to push the limits of knowledge and my own limits; and the childish hope of becoming one day an astronaut. These motivations gave me a great deal of strength necessary to overcome five years of hardship. But this work would not have been possible with motivations alone.

In fact, the right elements had to be there to make it happen: the right mentors, the right working environment and the right supports. Thomas, you have always been here for me from day one until the very end. You opened the way to walk in your steps and even cheered me up in difficult times. I have also learned substantially from discussing ideas with you. *Merci*. Andreas, I am glad that we could orientate my doctorate towards this out-of-the-box topic, which is a way of thinking important to me. This especially happened thanks to your valuable experience with the satellite industry. Besides that, you supported me throughout the ESA astronaut application process and gave me the chance to present my first TEDx Talk about space. For all the support and opportunities, *Danke*. Special credits to my past and present colleagues: Ovais, thank you for the company; Flo, thank you for the tips and your team spirit; Chri, thank you for the stimulating coffee discussions; Wolfgang H., thank you for being the backbone of the institute; Constanze, thank you for your efficiency and the kicker time; Alejandro, thank you for your daily good mood; Eri, thank you for your constant support; Sertac, thank you for bringing the Acta Astronautica paper back to life. Special credits to my friends and to the persons that made my stay in Munich brighter: Mathieu, Mélanie, Sindre, Juyeong, Lisa, Manas, Thida, Karina, Brice and Jun, you are the best! Last but not least, to my family: Pépé, Mémé and Éric, thank you always supporting me and providing me with a safe and comforting place to go to when wanting to forget about this doctorate; Papa, Maman, Rico, Baptiste, Eugénie, Aloïs simply thank you for being here and I hope we can catch up some of the time that has been invested in this crazy project.

Finally, this work would also not have been possible without the teachers who contributed extensively to my scientific education and kept me curious to know *more*. Along with the scientific education, I also want to thank the people that brought me space education and inspiration including the staff of the Advanced Master SCS and the International Space University.

To all the persons that made this journey possible: *Thank you*.

Tony Colin,  
Munich, 2<sup>nd</sup> of June 2022.



# Contents

---

<b>Abbreviations</b>	<b>iii</b>
<b>Notation</b>	<b>vii</b>
<b>1 Introduction</b>	<b>1</b>
1.1 History of satellite communications systems . . . . .	1
1.1.1 The birth of satellite communications systems . . . . .	1
1.1.2 The development of the satellite industry . . . . .	2
1.1.3 The advent of high-throughput satellites . . . . .	4
1.2 Future of satellite communications systems . . . . .	6
1.2.1 Overview and major directions . . . . .	6
1.2.2 Key technologies and new performance trade-offs . . . . .	8
1.3 Shaping the future of link budget analysis . . . . .	9
1.3.1 Critical impairments . . . . .	9
1.3.2 The satellite expert perspective . . . . .	11
1.3.3 The research literature perspective . . . . .	11
1.4 Contributions of this thesis . . . . .	13
1.4.1 Summary of results . . . . .	13
1.4.2 Outline of the thesis . . . . .	14
1.4.3 List of publications . . . . .	15
<b>2 Prerequisites</b>	<b>17</b>
2.1 Methodology for link budget analysis . . . . .	17
2.1.1 General characterization of impairments . . . . .	17
2.1.2 Basics on additive Gaussian impairments . . . . .	18
2.1.3 Basics on non-additive Gaussian impairments . . . . .	19
2.1.4 Impairments domination and asymptotes . . . . .	21
2.1.5 Extension to linear time-invariant systems . . . . .	22
2.2 Mathematical system model . . . . .	23
2.2.1 Modulation scheme . . . . .	23
2.2.2 Filters . . . . .	24
2.2.3 Amplifiers . . . . .	32
2.2.4 Oscillators . . . . .	36
<b>3 Mathematical Characterization</b>	<b>39</b>
3.1 Waveform imperfections . . . . .	39
3.2 Filter distortions . . . . .	41
3.2.1 General considerations . . . . .	41

3.2.2	Exponential polynomial representation . . . . .	42
3.2.3	Pole-zero representation . . . . .	50
3.3	Amplifier distortions . . . . .	52
3.3.1	General considerations . . . . .	52
3.3.2	Single-carrier mode . . . . .	52
3.3.3	Multi-carrier mode . . . . .	57
3.4	Oscillator noise . . . . .	63
3.4.1	General considerations . . . . .	63
3.4.2	Analysis . . . . .	64
3.5	Summary and future works . . . . .	69
<b>4</b>	<b>Applications</b>	<b>71</b>
4.1	Link budget refinement . . . . .	71
4.1.1	Scenario . . . . .	71
4.1.2	Link budget enhancement . . . . .	72
4.1.3	Link budget complements . . . . .	76
4.2	Link budget optimization . . . . .	78
4.2.1	Problem formulation . . . . .	78
4.2.2	Methodology of performance evaluation . . . . .	81
4.2.3	Numerical results . . . . .	83
4.3	Summary and future works . . . . .	86
<b>5</b>	<b>Conclusions and Future Research Directions</b>	<b>87</b>
5.1	Concluding remarks . . . . .	87
5.2	Directions for future research . . . . .	88
<b>A</b>	<b>Useful Definitions</b>	<b>89</b>
A.1	Raised-cosine filter . . . . .	89
A.2	Useful functions and generalized functions . . . . .	90
<b>B</b>	<b>Useful Identities</b>	<b>91</b>
B.1	Series . . . . .	91
B.2	Integrals . . . . .	92
B.3	Limits . . . . .	93
B.4	Stochastic processes . . . . .	93
B.5	Fourier transforms . . . . .	94
B.6	Miscellaneous . . . . .	94
<b>C</b>	<b>Proofs</b>	<b>95</b>
C.1	General carrier-to-interference ratios . . . . .	95
C.2	Waveform imperfections . . . . .	99
C.3	Filter distortions . . . . .	100
C.4	Amplifier distortions . . . . .	101
C.5	Oscillator noise . . . . .	102
<b>D</b>	<b>Data</b>	<b>103</b>

# Abbreviations

---

<b>3GPP</b>	3rd generation partnership project. 6
<b>ACI</b>	adjacent channel interference. 24
<b>ACM</b>	adaptive coding and modulation. 4
<b>ADC</b>	analog-to-digital converter. 7, 8
<b>AG</b>	additive Gaussian. i, 10, 11, 18, 19, 22, 23, 26, 29, 56, 67, 71, 72, 75, 79, 82, 85, 86
<b>ALC</b>	automatic level control. 35
<b>APSK</b>	amplitude-and-phase-shift keying. viii, 5, 12, 24
<b>BER</b>	bit error rate. 11
<b>CCSDS</b>	consultative committee for space data systems. 11
<b>CIR</b>	carrier-to-impairment power ratio. ix, 9, 10, 11, 12, 13, 14, 15, 17, 18, 19, 20, 21, 22, 24, 26, 27, 29, 32, 34, 35, 39, 40, 41, 42, 43, 44, 45, 46, 47, 48, 50, 51, 52, 53, 55, 56, 57, 59, 62, 63, 64, 65, 66, 67, 68, 69, 70, 71, 72, 74, 75, 76, 77, 78, 79, 80, 81, 82, 83, 84, 85, 86, 87, 88, 95, 97, 98, 100, 101, 102, 103, 104
<b>DAC</b>	digital-to-analog converter. 7, 11
<b>DCA</b>	dynamic carrier allocation. 14, 15, 71, 78, 79, 80, 81, 82, 83, 84, 85, 86, 87, 88
<b>DTH</b>	direct-to-home. 32, 36, 76
<b>DVB-S</b>	digital video broadcasting – satellite. 4
<b>DVB-S2</b>	DVB-S second generation. 5
<b>DVB-S2X</b>	DVB-S2 extensions. 8, 9, 36, 65, 71, 72, 73, 76
<b>ECSS</b>	European cooperation for space standardization. 11
<b>EIRP</b>	effective isotropic radiated power. 5, 103, 104
<b>ETSI</b>	European telecommunications standards institute. 4
<b>Eutelsat</b>	European telecommunications satellite organization. 3, 5, 6
<b>EVM</b>	error vector magnitude. 13, 18, 65
<b>FM</b>	frequency modulation. 3, 4
<b>FSK</b>	frequency-shift keying. 12
<b>HPA</b>	high-power amplifier. viii, ix, 1, 2, 3, 4, 6, 8, 12, 30, 31, 32, 33, 34, 35, 52, 53, 54, 55, 56, 57, 58, 59, 60, 61, 70, 72, 73, 74, 75, 77, 78, 96, 103, 104

<b>HTS</b>	high-throughput satellite. 4, 5, 6, 10, 14, 71, 72, 75, 86
<b>IAPR</b>	instantaneous-to-average power ratio. vii, 20, 24, 33, 34, 54, 55
<b>IFE</b>	in-flight entertainment. 79
<b>IMUX</b>	input multiplexer. 7, 30, 31, 50
<b>Intelsat</b>	international telecommunications satellite consortium. 2, 3
<b>ISI</b>	inter-symbol interference. ix, 12, 24, 25, 26, 27, 29, 32, 33
<b>ITU</b>	international telecommunication union. 3, 6
<b>LNA</b>	low-noise amplifier. 7
<b>LNB</b>	low-noise block. 7, 32, 36, 76, 104
<b>LO</b>	local oscillator. 9, 36, 37
<b>LS</b>	least-squares. 43, 44, 49
<b>LTI</b>	linear time-invariant. 23, 29, 33, 39, 41, 42, 52, 69, 77, 95, 98
<b>MODCOD</b>	modulation and coding. 71, 75, 103
<b>MSE</b>	mean squared error. 12, 13
<b>NTI</b>	nonlinear time-invariant. 33, 52, 57, 75, 96
<b>NTN</b>	non-terrestrial network. 6
<b>OBO</b>	output back-off. 73, 103
<b>OBP</b>	on-board processor. 5, 6, 8, 9, 31, 58, 78
<b>OFDM</b>	orthogonal frequency-division multiplexing. 13, 70
<b>OMUX</b>	output multiplexer. 7, 8, 30, 31, 44, 47, 49, 50, 51, 54, 75, 79, 80, 103
<b>PAPR</b>	peak-to-average power ratio. vii, 20
<b>PDF</b>	probability density function. 12
<b>PEB</b>	power equivalent bandwidth. 103, 104
<b>PSK</b>	phase-shift keying. 4, 12
<b>QAM</b>	quadrature amplitude modulation. 12
<b>RC</b>	raised-cosine. viii, 24, 25, 26, 27, 89
<b>RF</b>	radio-frequency. 3, 4, 8, 9, 31
<b>RR</b>	radio regulations. 3
<b>SC</b>	square-root-raised-cosine. viii, 11, 12, 13, 26, 27, 28, 29, 39, 40, 41, 42, 54, 70, 77, 89, 99
<b>SES</b>	société européenne des satellites. 3
<b>SSPA</b>	solid-state power amplifier. 31, 33
<b>TWTA</b>	traveling-wave tube amplifier. 31, 33, 72
<b>UHF</b>	ultra high-frequency. 1
<b>UHTS</b>	ultra high-throughput satellite. 6, 7, 8, 9, 10, 14, 15, 71, 78, 79, 85, 86, 87



---

<b>VHF</b>	very high-frequency. <a href="#">1</a>
<b>VHTS</b>	very high-throughput satellite. <a href="#">6</a>
<b>WSS</b>	wide-sense stationary. <a href="#">36</a> , <a href="#">64</a> , <a href="#">98</a>
<b>WWW</b>	world wide web. <a href="#">4</a>
<b>ZMWGP</b>	zero-mean white Gaussian process. <a href="#">13</a>



# Notation

---

## Sets

$\mathbb{N}$	nonnegative integers.
$\mathbb{Z}$	integers.
$\mathbb{Z}^*$	integers without the element 0.
$\mathbb{R}$	real numbers.
$\mathbb{R}_+$	nonnegative real numbers.
$\mathbb{R}_+^*$	positive real numbers.
$\mathbb{C}$	complex numbers.
$\mathbb{C}^*$	complex numbers without the element 0.

## Complex numbers

$j$	imaginary unit.
$z^*$	complex conjugate of complex number $z$ .
$ z $	complex modulus of complex number $z$ .
$\arg(z)$	argument of complex number $z$ (rad).
$\Re(z)$	real part of complex number $z$ .

## Stochastic processes

$\mathbb{E}[\mathcal{Z}]$	expectation of a complex random variable $\mathcal{Z}$ .
$\mathbb{E}[\mathcal{Z} \mathcal{Y} = y]$	conditional expectation of $\mathcal{Z}$ given $\mathcal{Y} = y$ .
$\mathbb{V}[\mathcal{Z}]$	variance of a complex random variable $\mathcal{Z}$ .
$\mathbb{V}[\mathcal{Z} \mathcal{Y} = y]$	conditional variance of $\mathcal{Z}$ given $\mathcal{Y} = y$ .
$\mathbb{C}[\mathcal{Z}_1; \mathcal{Z}_2]$	covariance between complex random variables $\mathcal{Z}_1$ and $\mathcal{Z}_2$ .
$\mathbb{I}_z(\mathcal{Z}) =  z /\mathbb{E}[\mathcal{Z}]$	instantaneous-to-average power ratio of $\mathcal{Z}$ given $z$ .
$\mathbb{P}(\mathcal{Z}) = \max_z(\mathbb{I}_z[\mathcal{Z}])$	peak-to-average power ratio of $\mathcal{Z}$ .
$\mathcal{Z} \sim \mathcal{N}(\mu, \sigma^2)$	random variable $\mathcal{Z}$ is normally distributed with mean $\mu$ and variance $\sigma^2$ .
$\mathcal{Z} \sim \mathcal{U}\{z_1, z_2, \dots\}$	random variable $\mathcal{Z}$ is uniformly distributed with elements $z_1, z_2, \dots$

## Operators and transforms

$f(n) \rightarrow g(n),$ as $n \rightarrow 0$	function $f(n)$ is asymptotically equivalent to function $g(n)$ , as $n$ tends towards small values.
--	---

$\mathcal{F}[h(t)](f)$	Fourier transform of time function $h(t)$ .
$\mathcal{F}^{-1}[H(f)](t)$	inverse Fourier transform of frequency function $H(f)$ .
$(h * g)(t)$	continuous convolution of functions $h$ and $g$ .
$(h * g)[n]$	discrete convolution of functions $h$ and $g$ .
$(\cdot)_{\text{dB}} = 10 \cdot \log_{10}(\cdot)$	quantity converted to the decibel scale.
$E_{\%}(\cdot)$	percent error between exact and approximate values.
$A_{\%}(\cdot) = 10^2 - E_{\%}(\cdot)$	accuracy between exact and approximate values.
$a \propto b$	$a$ is proportional to $b$ .
$\text{mod}(a, b)$	modulo operator returning the remainder of the Euclidean division of $a$ by $b$ .

## Functions and generalized functions

See Appendices A and B.5 for more details on the definitions and related identities.

$\delta(t)$	Dirac delta function.
$\text{III}_T(t)$	Dirac comb with period $T$ .
$\Pi_T(t)$	rectangular function defined on the interval $[-T; T]$ .
$\Omega_T(f)$	sine cardinal with period $2T\pi$ and peak amplitude $2T$ .
$h_{\text{RC}}(t, \alpha, T_s)$	raised-cosine filter.
$h_{\text{SC}}(t, \alpha, T_s)$	square-root-raised-cosine filter.
$h_{\text{SC}}^{\sim}(t, \alpha, T_s, ST_s, F_s)$	sampled time-limited square-root-raised-cosine filter.
$h_{\text{CH}}(t)$	channel impulse response.
$h(t)$	system impulse response.
$h^{\rightarrow}(t)$	pre-high-power amplifier system impulse response.
$h^{\leftarrow}(t)$	post-high-power amplifier system impulse response.
$g_{\text{HP}}(\cdot)$	high-power amplifier function.

## Constant

$\xi = \ln(10)/20$	conversion factor related to the decibel scale ( $\xi \approx 0.11513$ ).
--------------------	---

## Most used variables

$T_s$	carrier symbol period (s).
$R_s = 1/T_s$	carrier symbol rate (Bauds).
$\zeta^{(q,i)} = T_s^{(q)}/T_s^{(i)}$	symbol period ratio between the $q^{\text{th}}$ - and $i^{\text{th}}$ -users.
$F_s$	sampling frequency (Hz).
$N_{\text{S/s}} = F_s/R_s$	number of samples per symbol.
$f_{\Delta}$	carrier frequency offset (Hz).
$S$	square-root-raised-cosine one-sided span.
$\alpha$	square-root-raised-cosine roll-off factor.
$B = (1 + \alpha)R_s$	carrier bandwidth (Hz).
$B_N$	channel nominal bandwidth (Hz).
$f_c$	distortions filter cut-off frequency (Hz).
$\varrho = R_s/f_c$	distortions bandwidth ratio.
$\{R_k\}_{k \in \mathbb{N}^*}$	ring radii of amplitude-and-phase-shift keying modulations.

$v_1 = R_2/R_1$	1 <sup>st</sup> -order ring radius ratio.
$v_2 = R_3/R_1$	2 <sup>nd</sup> -order ring radius ratio.
$\{r_k\}_{k \in \mathbb{N}^*}$	modulation coefficients.
$\tau$	decision instant offset relative to the symbol period $T_s$ .
$\tau^*$	decision instant offset relative to the symbol period $T_s$ maximizing the carrier-to-impairment power ratio.
$N_{\text{FD}}$	order of filter distortions.
$\{g_k\}_{0 \leq k \leq N_{\text{FD}}}$	gain coefficients (dB/MHz <sup>k</sup> ).
$\{d_k\}_{0 \leq k \leq N_{\text{FD}}}$	group delay coefficients ( $\mu\text{s}/\text{MHz}^k$ ).
$\{x_k\}_{0 \leq k \leq N_{\text{FD}}}$	gain distortions coefficients (dB/MHz <sup>k</sup> ) $\cdot$ (Mbauds) <sup>k</sup> .
$\{y_k\}_{0 \leq k \leq N_{\text{FD}}}$	group delay distortions coefficients ( $\mu\text{s}/\text{MHz}^k$ ) $\cdot$ (Mbauds) <sup>k+1</sup> .
$N_{\text{AD}}$	order of amplifier distortions.
$\{\gamma_{2k+1}(\bar{P}_{\text{HP}}^{\text{in}})\}_{0 \leq k \leq N_{\text{AD}}}$	complex coefficients of the high-power amplifier polynomial representation defined at mean input power per symbol $\bar{P}_{\text{HP}}^{\text{in}}$ .
$P_{\text{HP}}^{\text{in}}$	instantaneous power at the high-power amplifier input (V <sup>2</sup> ).
$P_{\text{HP}}^{\text{out}}$	instantaneous power at the high-power amplifier output (V <sup>2</sup> ).
$\Psi_{\text{HP}}^{\text{out}}$	phase offset at the high-power amplifier output (°).
$\bar{P}_{\text{HP}}^{\text{in}}(t)$	mean power per symbol at a given time $t$ at the high-power amplifier input (V <sup>2</sup> ).
$\bar{\bar{P}}_{\text{HP}}^{\text{in}}$	mean power per symbol at the high-power amplifier input (W) (including temporal mean).
$\bar{\bar{P}}_{\text{HP}}^{\text{in}(i)}$	mean power per symbol at the high-power amplifier input of the $i^{\text{th}}$ -user (W) (including temporal mean).
$\lambda_{\text{HP}}^{(i)} = \bar{\bar{P}}_{\text{HP}}^{\text{in}(i)} / \bar{\bar{P}}_{\text{HP}}^{\text{in}}$	power sharing ratio at the high-power amplifier input of the $i^{\text{th}}$ -user.
$\lambda_{\text{HP}}^{(q,i)} = \bar{\bar{P}}_{\text{HP}}^{\text{in}(q)} / \bar{\bar{P}}_{\text{HP}}^{\text{in}(i)}$	power ratio at the high-power amplifier input between the $q^{\text{th}}$ - and $i^{\text{th}}$ -users.
$\sigma_{\text{N}}^2$	additive white Gaussian noise variance (W).
$\sigma_{\Phi}^2$	oscillator phase noise variance (W).
$\varepsilon_{\Phi, \text{tot}}$	energy of the phase noise mask (W).
$C$	carrier power (W).
$I$	impairment power (W).
$(C/I)$	carrier-to-impairment power ratio.
$(C/I)^*$	carrier-to-impairment power ratio defined at optimal decision instant offset $\tau^*$ .
$L$	inter-symbol interference partial sum limit.



# 1 | Introduction

---

## Contents

<b>1.1</b>	<b>History of satellite communications systems . . . . .</b>	<b>1</b>
<b>1.2</b>	<b>Future of satellite communications systems . . . . .</b>	<b>6</b>
<b>1.3</b>	<b>Shaping the future of link budget analysis . . . . .</b>	<b>9</b>
<b>1.4</b>	<b>Contributions of this thesis . . . . .</b>	<b>13</b>

---

This chapter sets the landscape for the contributions of this thesis. Section 1.1 addresses satellite communications systems from a historical perspective for a better understanding of contemporary systems. In particular, the key innovations and drivers in the technological evolution of satellite communications systems are exposed. Section 1.2 makes the transition between contemporary systems and future systems. It lays the foundations for the key technologies and new performance trade-offs. On this basis, Section 1.3 expresses the needs in link budget analysis for future satellite communications systems. Thus, it formulates the knowledge gaps and introduces the state-of-the-art in this domain. Finally, the contributions of this thesis are emphasized in Section 1.4.

## 1.1 History of satellite communications systems

### 1.1.1 The birth of satellite communications systems

Operation Moon Bounce, 24<sup>th</sup> July 1954: James H. Trexler, an engineer at the radio antenna facility of the U.S. Naval Research Laboratory, speaks into a microphone. Two and a half seconds later, his words come back to him after traveling 800,000 km bouncing off the Moon. For the first time ever, the sound of a human voice has been transmitted beyond the ionosphere and returned back to Earth. Communication relays beyond Earth were born due to the Cold War. With the U.S. Navy's fleets encircling the globe, secure and reliable communication links were considered critical to national security. The success of this project quickly led to the development of a fully operational Moon relay communications system between Washington and Hawaii in 1959. Since the first demonstration, the system was further optimized in frequency, power, and antenna size. The frequency transitioned from very high-frequency (30 MHz – 300 MHz) to ultra high-frequency (300 MHz – 3 GHz), the power of the high-power amplifier (HPA) transmitter increased from 10 kW to 100 kW and

the antennas' diameter was scaled from an initial 183 m down to 28 m. The communication link could now accommodate up to 16 teleprinter channels at a rate of 60 words/min [1].

In parallel to this development, the *space race* raged between the U.S. and the Soviet Union. Based on nationalistic competition, both superpowers developed ballistic missiles that could launch objects into space. The launch in 1957 of Sputnik 1, the first artificial satellite to orbit the Earth, triggered a series of groundbreaking achievements in satellite communications technologies. This led to the rapid transition from using a natural satellite to using an artificial satellite for relay communications systems. Satellite communications evolved from being *passive*, i.e. by the reflection of radio waves, to being *active*. As such, the satellite Telstar 1 in 1962 was able to perform two major actions: It could downconvert a received signal from 6 GHz to 4 GHz, thus avoiding interference; and it could re-amplify the signal by a factor of 100 using an HPA powered by solar cells, thus improving the quality of the signal before sending it back to Earth. This technological step enabled the world's first transatlantic television signal. However, the contact was limited to approximately 30 minutes every 2 hours 25 minutes due to the satellite's orbit [2]. Therefore, one problem remained to be solved: the link availability.

As early as 1895, the Russian rocket scientist Konstantin Tsiolkovsky identified that any object with the same rotational speed as the Earth reaching the altitude of 35,790 km possesses a fascinating property: The object would have enough velocity to remain in orbit and appear fixed in the sky. While Tsiolkovsky imagined a gigantic free-standing tower to reach this height [3], the first idea of satellites in geostationary orbit through rocketry is attributed to Herman Potočnik and this work of 1929 [4]. Extending this idea, the British science fiction writer Arthur C. Clarke suggested in 1945 that a group of three manned space stations in geostationary orbit arranged in a triangle could cover the whole Earth<sup>1</sup> and thus, be used for broadcasting and communication relays [5]. Twenty-one years later, fiction became reality with the world's first geostationary communication satellite, Syncom 3 [6]. Following in its footsteps, the first group of three geostationary communications satellites able of achieving global coverage was completed in 1969 by the international telecommunications satellite consortium (Intelsat). Later that year, 500 million television viewers all over the world witnessed the first step of Neil Armstrong on the Moon via live broadcasting of Intelsat satellites [7].

### 1.1.2 The development of the satellite industry

The space race provided a fertile ground for a booming satellite industry. After Intelsat comes Telesat: a commercial company established in 1969 with a mandate to provide satellite communications services to Canada. Three years later, the world's first commercial domestic communications satellite in geostationary orbit, Anik A1, was launched by Telesat [8]. In 1977, it was the turn of Europe. Out of the ambition to build a European industry in the manufacture, launch, and operation of satellites,

---

<sup>1</sup>Three satellites are in line-of-sight with all Earth's surface between latitudes 81° S and 81° N.



the European telecommunications satellite organization (Eutelsat) was created. Eutelsat's first fleet of five commercial satellites in geostationary orbit was completed in 1988 [9]. Although the first satellite operators like Intelsat, Telesat, and Eutelsat had a governmental origin, they later became privatized [7, 8, 9].

From the end of the 1970s, the success story of satellite communications systems was driven by the broadcast of television. As a result, satellite communications systems were optimized such as to reduce the size of satellite television dishes and *a fortiori* reduce the cost of the user terminal receiver. In 1979, Soviet civil satellites, Gorizont, were already able to deliver television programs with a terminal size reduced to 2.5 m [10]. A decade later, the newly formed Luxemburgish satellite operator, société européenne des satellites (SES), launched its first satellite Astra 1A [11]. The technology of this satellite enabled the reception of television with dishes as small as 90 cm from 1989. The transition from C-band (4 GHz – 8 GHz) to Ku-band (12 GHz – 18 GHz) took place. In particular, the satellite communication payload could accommodate 16 different Ku-band communication channels. Each channel was associated with a 26 MHz-bandwidth, equipped with a 45 W-HPA, and capable of broadcasting one television program to Western Europe continuously [12]. For illustration purposes, the simulated footprint of Astra 1A is depicted in Fig. 1-1 based on the data of [12] and the footprint theory of [13]. Lastly, frequency modulation (FM) was used due to its resilience to high signal variations, noise, and interference [14].

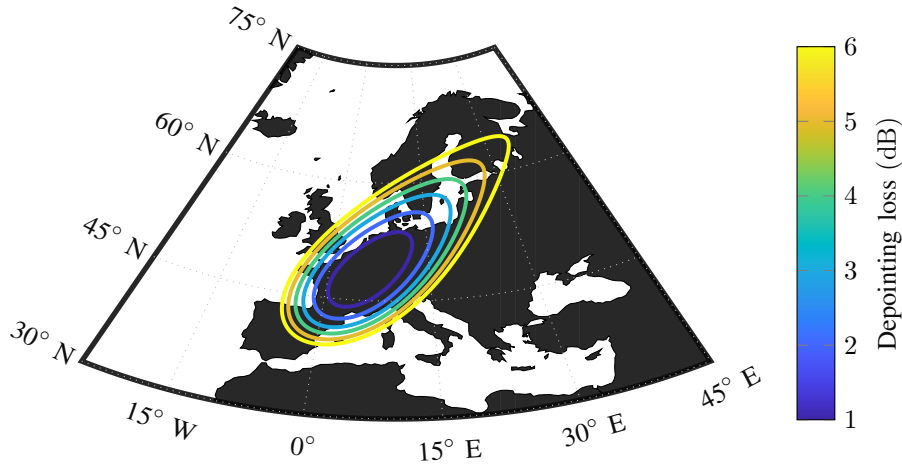


Figure 1-1: Estimated footprint of Astra 1A

Along with the growth of the satellite industry came regulations for the fair use of resources. In particular, the international telecommunication union (ITU) radio regulations (RR) has been regulating the allocation of the radio-frequency (RF) spectrum from 8.3 kHz up to 3 THz<sup>2</sup> to ensure interference-free operations of communication systems and provides ITU Member States with equitable access to the radio spectrum since 1906 [15, 16]. In the context of ITU's organization, the World Administrative Radio Conference on the Use of the Geostationary-Satellite Orbit and the Planning

<sup>2</sup>Since the frequency range of allocation has changed over time, this specific range applies to the latest edition of 2020 [15].

of the Space Services Utilizing It was held in 1985. This conference had the difficult task to reconcile the principle of guaranteed and equitable access with that of the efficient and economic use of two limited natural resources: the geostationary orbit and the RF spectrum [17]. As a result of this conference, mandatory technical parameters were defined to prevent harmful interference. Among others, they include the spacing of geostationary satellites and geometrical power radiation constraints [18]. At the satellite communication payload level, this implies the use of filters to limit out-of-band radiation. Indeed, since the HPA entails a spectral regrowth [19] and frequency conversion causes an image frequency [20], these leakages must be kept under control using bandpass filters at least at the output of the satellite<sup>3</sup>. Similarly, bandpass filters at the input of the satellite are used to prevent external out-of-band radiation from leaking into the system.

Along with regulations came standardizations. In 1988, the standardization organization, European telecommunications standards institute (ETSI), was created. It especially developed the popular open standard, digital video broadcasting – satellite (DVB-S), whose first version was released in 1995. This standard specified physical layer characteristics such as channel coding, modulation, pulse shaping as well as satellite input and output filters [21]. This milestone also marked the evolution from analog to digital communications. In particular, a transition from analog FM to digital phase-shift keying (PSK) modulation was made to achieve further power and spectrum efficiency [22]. It is in this context that the European satellite communications industry notably started the 2000s with an estimated turnover of 1.5 B€, meaning at that time one-third of the overall European space industry<sup>4</sup> [23]. But it was still the early years of a flourishing industry.

### 1.1.3 The advent of high-throughput satellites

In July 2004, another achievement was conceded to Telesat. Through the quest for higher throughputs, the satellite Anik F2 was created. With its first commercialized use of Ka-band (18 GHz – 30 GHz), the Canadian satellite reached a total throughput of about 2 Gbits/s [24, 25]. From this point, satellites of this type were referred to as high-throughput satellites (HTSs). Although Anik F2 still provided voice, data, and broadcast services, a new important service was delivered: the two-way broadband Internet access. Indeed, with the rapid growth of the Internet<sup>5</sup> in the year 2000s, Internet access became an essential part of modern satellite communications. Along with the need for higher throughputs came more heterogeneous users' demand, which required flexibility. Also, the increase in frequency meant more sensitivity to atmospheric perturbations. Innovative algorithms were developed such as adaptive coding and modulation (ACM). This algorithm was exposed in the first 2005 release of the DVB-S second generation (DVB-S2) standard [27] and enabled a dynamic

<sup>3</sup>Most of the satellite architectures also use a bandpass filter after the frequency conversion.

<sup>4</sup>Other satellite applications existed at that time such as science, Earth observation, navigation, etc. By contrast, they only represent an estimated 0.2 B€ of the turnover.

<sup>5</sup>This particularly includes the booming of the world wide web (WWW) and search engines like Google. In 2003, about 11 % of the world population had already Internet access [26].

adaptation of the system depending on atmospheric weather conditions. As another improvement, amplitude-and-phase-shift keying (APSK) modulation schemes were introduced to further enhance the spectrum efficiency when a higher power margin is available.

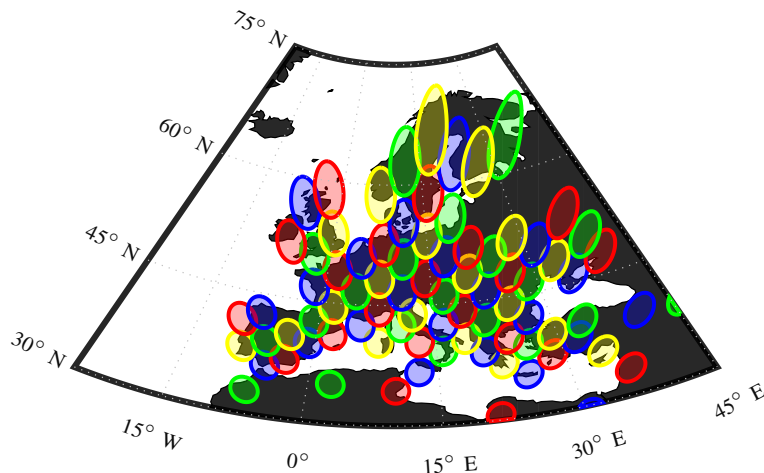


Figure 1-2: Estimated footprint of KA-SAT

In 2010, the total throughput of Eutelsat's KA-SAT satellite<sup>6</sup> could already exceed 70 Gbits/s thanks to an innovative multibeam communications system [25, 29]. Equipped with four multi-feed deployable antennas, the satellite was able to generate narrow spotbeams that led to two major advantages. On the one hand, the frequency can be re-used for non-neighboring spotbeams. In this way, the throughput gain coming from the re-use of bandwidth substantially outweighs the loss due to inter-beam interference. On the other hand, narrower beams lead to higher antenna gains and thus, to an increase in satellite effective isotropic radiated power (EIRP). Additionally, services could be better distributed throughout Europe based on the users' location and demand. For the sake of illustration, Fig. 1-2 shows the simulated footprint of KA-SAT based on current satellite pointing data [30] and footprint theory of [13]. This typical multibeam HTS system applies a four-color scheme where each color corresponds to a specific bandwidth and polarization. Each ellipse represents the 3 dB depointing loss with respect to the spotbeam center. By contrast with single-spotbeam traditional satellites, KA-SAT was configured with 82 spotbeams. Each spotbeam with about 250 km diameter supported a 250 MHz wideband channel in uplink and downlink [31]. This paradigm shift marked the transition from *bent-pipe* analog transparent payloads to digital transparent payloads [32, 33, 34]. Indeed, innovations in space-qualified on-board processors (OBPs) [35, 36] enabled channelization filtering as well as routing between beams digitally. By contrast, interconnectivity was traditionally achieved using analog filters and switch networks with limited flexibility. Based on these fundamental principles, dozens of HTSs were developed and launched in the next years [25].

<sup>6</sup>In 2021, Eutelsat transferred the satellite's ownership to Viasat [28].

After a decade of HTSs, a new generation of satellites arose with even higher throughputs, more beams as well as more flexible and digitalized payloads: very high-throughput satellites (VHTSs). Launched in October 2021, SES-17 was set to be the first Ka-band geostationary satellite to embark a fully digital payload powered by one of the most powerful OBPs<sup>7</sup>. This OBP especially enables unique features such as unlimited traffic routing and frequency conversions. Combined with flexible HPAs, it can better meet the users' changing demands in real-time by adapting the path, bandwidth and power. In particular, nearly 200 user spotbeams can be connected to any other spotbeam at any time [38]. In response to SES-17, the launch of two notable VHTSs has been announced by Eutelsat and Viasat: Konnekt VHTS and ViaSat-3 satellites<sup>8</sup>. They are expected to reach a total throughput of 500 Gbits/s [41] and 1 Tbits/s [42], respectively. In particular, the latter will be configured with 1,000 spotbeams [43]. With throughputs foreseen beyond the symbolic Tbits/s mark, the evolution of these satellites has already a name: ultra high-throughput satellite (UHTS).

## 1.2 Future of satellite communications systems

### 1.2.1 Overview and major directions

Along with UHTS development comes a new key application: The next generation of wireless technology for mobile cellular communication. In particular, it is the 3rd generation partnership project (3GPP), a consortium of telecommunication standards organizations and partners, that is currently developing 5G-and-beyond systems [44]. As such, the Release 17 of global standards<sup>9</sup> will be the first to include input from non-terrestrial network (NTN) groups and address satellites' role in the 5G ecosystem [45]. More broadly, the main requirement of the 5G-and-beyond endeavor is to guarantee a ubiquitous geographical coverage to connect the remaining unconnected population<sup>10</sup>. For this purpose, an increased integration of satellites into terrestrial networks is envisioned [47]. In the context of 5G-and-beyond systems, the most relevant satellite applications include broadband internet services to fixed remote locations and to mobile applications (e.g., aircraft, ships, trains, and cars) as well as complementary services via backhauling (e.g., delivery to the edge or cloud) [48]. Other use cases also include emergency and disaster relief [49].

Two important evolutionary steps are foreseen for the next-generation UHTS communications systems. On the one hand, the bandwidth will increase to meet the future target data rate of future applications. It will be possible to obtain from 500 MHz

<sup>7</sup>It is the 5<sup>th</sup> generation of Thales's digital transparent processor and so-called SpaceFlex™ VHTS processor [37].

<sup>8</sup>As of February 2022, both ViaSat-3 and Konnekt VHTS launches have been delayed by the COVID-19 pandemic disruption [39, 40]. They are planned for summer 2022 and second half of 2023, respectively.

<sup>9</sup>As of February 2022, the Release 17 is in the stage 3 of production [45].

<sup>10</sup>The ITU estimates that approximately 2.9 billion people – or 37 % of the world's population – have still never used the Internet according to the latest 2021 statistic [46].

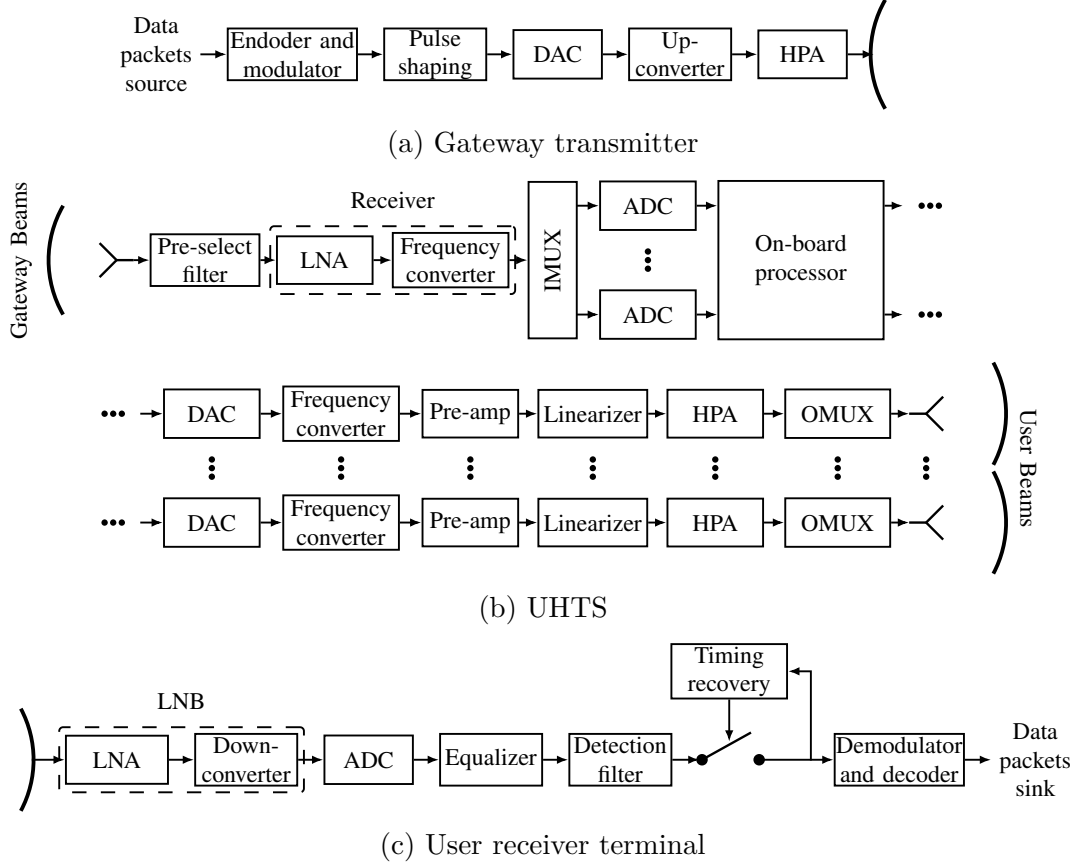


Figure 1-3: Block diagram of UHTS communications system

up to 2.9 GHz of downlink bandwidth per polarization by shifting feeder links to the Q/V-band (42.5 GHz – 51.4 GHz) and exploiting the available Ka-band resources (17.3 GHz – 21.2 GHz) in the user links [50]. On the other hand, the allocation of the payload resources (e.g., bandwidth, time, power, and coverage) will become increasingly flexible. This will enable to adapt to more heterogeneous communication services and their evolution [51]. For the sake of illustration, the block diagram of a forward link<sup>11</sup> UHTS communications system is depicted in Fig. 1-3. More specifically, an instance of gateway transmitter, the UHTS multipoint-to-multipoint relay and an instance of user receiver terminal are presented in Fig. 1-3a, Fig. 1-3b and Fig. 1-3c, respectively. Furthermore, the notations DAC, ADC, IMUX, OMUX<sup>12</sup>, LNA, LNB denotes digital-to-analog converter, analog-to-digital converter, input multiplexer, output multiplexer, low-noise amplifier, and low-noise block, respectively. For the reader eager to learn more details about the system components, it is advised

<sup>11</sup>The forward link is directed from the gateway transmitters to the users and is especially known to be more demanding than the return link.

<sup>12</sup>Although traditional satellites combine a demultiplexing operation (respectively multiplexing operation) with the input filters (respectively output filters) to remove the out-of-band emissions, it is not always the case with recent architectures [32]. In this work, the terminology of multiplexing and demultiplexing is conserved and considered as optional.

to refer to [19, 20]. In particular, two main readings considered as a support for this thesis are the DVB-S2 extensions (DVB-S2X) standard in its latest 2021 release [52] and the satellite payload engineer perspective provided by [53]. In the following, key technologies for UHTS communications systems and new trade-offs are discussed to lay the groundwork for the contributions of this thesis.

### 1.2.2 Key technologies and new performance trade-offs

The OBP is at the heart of an enhanced satellite flexibility and enables the smart allocation of on-board resources. However, this enhancement does not come without costs. On the one hand, the OBP increases the power consumption of the satellite. On the other hand, the digitalization performed by the ADC is impairing the signal's waveform to some extent. Thus, the *waveform imperfections*<sup>13</sup> should be closely monitored.

On another side, the wideband OMUX filter appears as a key technology for future satellite communications payloads. Novel wideband technologies offer several advantages. Firstly, it enables to reduce the complexity of the RF hardware and save dry mass [54]. Secondly, the spectrum utilization is also enhanced by eliminating guard bands between the transponder channels. Thus, it offers a multicarrier environment, where the different communication services can coexist, while still allowing for high-rate single-carrier operation. However, the *filter distortions* belong to the new challenges coming with such technology. They are caused by the nonideal channel frequency response of the satellite filters, but do not give rise to spectral regrowth as opposed to nonlinear distortions. That is why they are also referred to as linear distortions. From a filter theory standpoint, increasing the bandwidth of the satellite filters does not change their filter distortions characteristic. However, the ratio between the carriers' bandwidth and the channel bandwidth tends to decrease. This makes the carriers more prone to higher variations of distortions, especially in the presence of passband ripples and close to the edge of the filters. Therefore, it becomes crucial to determine how to optimally place these carriers within the channel bandwidth. Although these filters are typically based on Chebyshev and elliptic transfer functions [19, 55, 56], the theoretical characteristic cannot be exactly met due to challenging design constraints. From a practical standpoint, the design of the OMUX filters is especially difficult. At a physical level, they are required to handle high power: typically more than 120 W per channel [57]. Thus, the current technology inherently involves heavy and bulky hardware components. The insertion loss must also be minimized since it leads directly to a reduction of radiated power. At a signal level, the OMUX must comply with a minimum out-of-band attenuation and stringent in-band specifications. In the end, this results in a complex and critical trade-off involving physical considerations and acceptable levels of filter distortions.

Since the carriers are sharing the same wideband HPA, it is paramount to monitor *amplifier distortions*. In particular, the nonlinear characteristic of the HPA leads to intermodulation products between the carriers. Even though the OBP enables the

<sup>13</sup>The concept of waveform imperfections is further detailed in the next chapter.



implementation of novel sophisticated compensation mechanisms, such as on-board adaptive digital pre-distortion [58, 59], impairments are still remaining and considered critical.

Besides that, particular attention should be given to frequency converters. They are commonly composed of a multiplicative device, the RF mixer, and a so-called local oscillator (LO). The LO typically generates a sinewave set to a specific frequency. When this sinewave is multiplied with the signal through the mixer device, the desired frequency conversion is performed. The noise entailed by the oscillator has always been a critical source of impairments in communication systems and especially in the context of satellite communications systems. It is notably recognized as being one of the main limiting performance factors for higher order modulations (16-APSK and above for low roll-off factors) in standards such as the DVB-S2X [52]. Since the noise is dominant in phase, it is more commonly referred to as phase noise. As UHTS systems are moving towards higher frequencies to obtain more bandwidth, higher noise power is expected. From a physics standpoint, this scaling effect can be observed in the semi-empirical Leeson phase noise model [60]. From a technological standpoint, it becomes more challenging to design LOs with low phase noise as the frequency increases.

Thus, it has become of high interest to precisely characterize impairments such as waveform imperfections, filter distortions, amplifier distortions, and oscillator noise for future UHTS systems. Keeping this in mind, the next section takes the perspective of a hypothetical link budget analysis in future satellite communications systems. On this basis, it is exposed how such impairment would be characterized nowadays and the knowledge gaps are identified.

## 1.3 Shaping the future of link budget analysis

### 1.3.1 Critical impairments

In this thesis, the umbrella term *impairment* is used to designate both noise and interference. Thus, the impact of any impairment on the system can more generally be characterized by a carrier-to-impairment power ratio (CIR). As support for the explanation, the following simplified and idealistic<sup>14</sup> UHTS link budget is presented:

$$\left(\frac{C}{I}\right)^{-1} = \left(\frac{C}{I}\right)_{\text{UL}}^{-1} + \left(\frac{C}{I}\right)_{\text{DL}}^{-1} + \left(\frac{C}{I}\right)_{\text{AB}}^{-1} + \left(\frac{C}{I}\right)_{\text{WI}}^{-1} + \left(\frac{C}{I}\right)_{\text{FD}}^{-1} + \left(\frac{C}{I}\right)_{\text{AD}}^{-1} + \left(\frac{C}{I}\right)_{\text{ON}}^{-1}, \quad (1.3.1)$$

which from left to right denote the system CIR, the uplink noise CIR, the down-link noise CIR, the adjacent beams CIR, the waveform imperfections CIR, the filter distortions CIR, the amplifier distortions CIR, and the oscillator noise CIR. In other words, it is a common approach to resort to such decomposition to express the system CIR as a function of the CIR of the individual impairments [61]. Of course, the list

<sup>14</sup>As presented in the next chapters of this thesis, such decomposition is only valid depending on the nature of the impairments and precise conditions must met.

is non-exhaustive<sup>15</sup> and highly dependent on the considered satellite communications system architecture. Uplink and downlink noises are well-known to be additive Gaussian (AG) [61]. With the advent of HTSs, the CIR resulting from the interference of adjacent beams has become critical. In search of improving this CIR for UHTS communications systems, precoding has been an active area of research and particularly in the context of full-frequency re-use [62]. However, this CIR – by its nature – can be considered as AG [63] and will not be the focus of this thesis. It is worth noting that the improvement of link budgets using regenerative payloads is also not the primary focus. Based on the arguments exposed in Section 1.2.2, four non-AG impairments have been identified for typical UHTS link budget analysis. For the sake of visualization, these impairments are illustrated in Fig. 1-4. It is worth pointing out

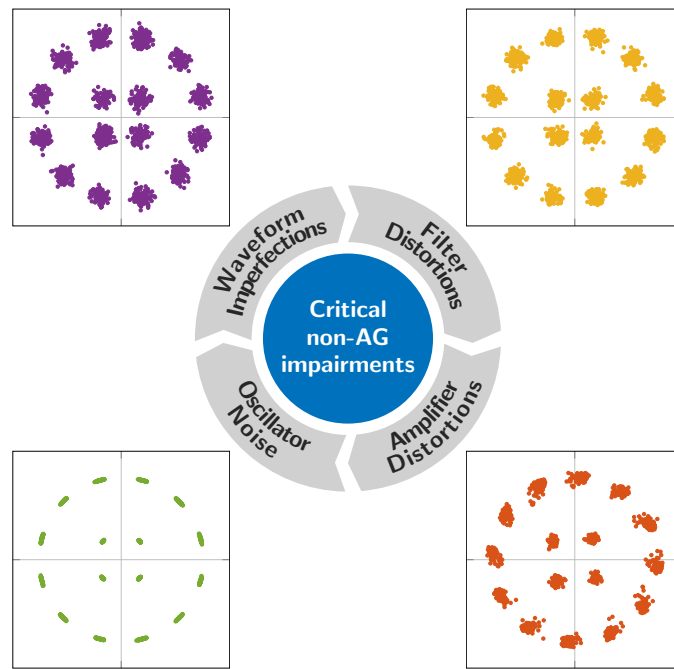


Figure 1-4: Overview on the critical non-AG impairments

that even the most sophisticated software tools such as [64, 65], commonly used for satellite link budget determination, do not include impairments caused by waveform imperfections, filter distortions, and oscillator noise. Furthermore, amplifier distortions are presumably characterized based on an empirical approach. This raises two questions: How do satellite experts, such as operators, manufacturers, and equipment suppliers, take into account such impairment in practice? Is there any mathematical characterization available in the research literature? The answers to these questions are developed in the next sections.

<sup>15</sup>Although often considered less critical, other well-known impairments such as antenna cross-polarization CIR or adjacent satellite CIR may be incorporated as well.



### 1.3.2 The satellite expert perspective

One of the primary situations, where a characterization of impairments is needed, is during the initial phases of a satellite development following the widespread standard issued by the European cooperation for space standardization (ECSS) [66]. Indeed, these design phases are dedicated to identifying the key drivers of the system design in terms of cost and performance. At this stage, it is of paramount importance to identify the critical carrier parameters. However, satellite payload engineers have to resort to empirical heritage rules to assess impairments such as the filter distortions entailed by each satellite component [67]. It is then crucial to derive novel mathematical expressions enabling an accurate – and preferably low-complexity – characterization of such impairment. This also leads to a clear identification of the impact of the carrier parameters.

In the later stages of development, satellite experts resort to time-consuming and cumbersome transmission chain simulations to estimate CIRs (typically resulting from non-AG impairments). In particular, it is challenging to model and generate numerically accurate impairments such as the oscillator noise due to its physical nature [68]. Conventional frequency-domain software simulations require a fine resolution (in the order  $10^{-7}$  with respect to the sampling frequency for typical phase noise masks [69]) that can lead to a significant simulation time. In this context, it is also more difficult to characterize the behavior of the oscillator noise and understand the influence of key transmission chain parameters. In the end, all estimated CIRs are combined in the same fashion as (1.3.1).

### 1.3.3 The research literature perspective

The research literature on the mathematical characterization of each of the considered impairments is detailed below. In particular, the key underlying assumptions, the key elements of the communications system model, and the selected characterization method are exposed.

#### Waveform imperfections

In satellite communications systems, the waveform is traditionally based on the square-root-raised-cosine (SC) filter. In this context, Rohit *et al.* discussed the trade-offs between the digital-to-analog converter (DAC) oversampling factor and the SC roll-off [70]. More specifically, they characterize the performance of the SC in terms of bit error rate (BER) as part of the consultative committee for space data systems (CCSDS) 131.2-B-1 standard [71]. More recently, Pilato *et al.* expanded the study of the SC by taking into account the impact of time finiteness with the SC span. They characterized the performances in terms of sidelobe attenuation [72]. To the best of the author's knowledge, no mathematical characterization of SC-based waveform imperfections is available in the literature.

## Filter distortions

In satellite communications systems, a wide variety of filter distortions are possible. Thus, most of the available mathematical characterizations focus on a particular model of filter distortions. As such, Bobilin and Lindenlaub modeled the distortions as first-, second-, and third-order Butterworth filters [73]. In this context, they characterized mathematically the CIR entailed by these distortions. However, their system model is limited to binary frequency-shift keying (FSK) modulation and rectangular pulse shaping. On the other hand, Gobbi analyzed thoroughly the impulse response of a system, which includes filter distortions in the form of a gain slope [74]. The system model is limited to PSK modulation and rectangular pulse shaping. In the same year, Moreira and Brandao characterized mathematically cubic, quadratic, and sinusoidal amplitude distortions in terms of mean squared error (MSE) [75]. However, their system model is limited to quadrature amplitude modulation (QAM) and rectangular pulse shaping. Metzger and Valentin provide a recursive algorithm to characterize the probability density function (PDF) of inter-symbol interference (ISI) caused by the distortions of a two-path channel [76]. Although their system model is based on SC pulse shaping, it is nonetheless restricted to QAM. It is worth noting that Sadr and Hurd [77] derived a CIR lowerbound depending on the amplitude of filter distortions ripples. Overall, the most advanced work on this topic can be attributed to Jones [78]. Indeed, it not only includes a generalized formulation of the CIR that is applicable to any kind of filter distortions, but also takes into account the impact of the decision instant, which is widely omitted in the literature. However, his analysis is still limited to PSK modulation and rectangular pulse shaping. Consequently, scant attention has been paid to meet the characteristics of the present and future satellite communications systems, which include – among others – a wide range of linear modulation techniques and the SC pulse shaping. To the best of the author’s knowledge, no mathematical characterization of filter distortions taking into account the needs of the satellite community is available in the literature.

## Amplifier distortions

Benedetto and Biglieri provided a mathematical expression of the MSE resulting from single-carrier amplifier distortions [79]. In particular, they consider PSK modulation, a nonlinear HPA characteristic, and include the impact of filters. As such, an example is given with a four-pole Butterworth filter before the HPA (on top of the pulse shaping) and a two-pole Butterworth filter after the HPA. However, the results are still limited to the third-order polynomial approximation of the HPA characteristic. An extension of this work has been proposed by Beidas for multi-carrier amplifier distortions [80]. In this analysis, a low-complexity<sup>16</sup> expression of the resulting MSE is formulated. Like the aforementioned work, it is obtained by using the third-order polynomial approximation of the HPA characteristic and truncating the impulse responses of filters. Moreover, it takes into account PSK and APSK modulations as

---

<sup>16</sup>Although the expression is quite extensive, it can still be regarded as low-complexity in the case of multi-carrier amplifier distortions.

well as SC pulse shaping. To this date, it can be considered as the most advanced mathematical characterization of amplifier distortions for satellite communications systems. However, the expression assumes identical characteristics among the carriers (symbol rate and roll-off) and is not adapted to link budget calculations like the CIR.

### Oscillator noise

To characterize the oscillator noise, several simulations, measurements and estimations of error vector magnitude (EVM) have been proposed in the literature [81, 82, 83]. Recently, a few EVM mathematical expressions have been derived as well. For instance, Höhne and Ranki derived an expression measuring the impairment entailed by the oscillators' noise in beamforming [84]. However, the oscillator noise corresponding to each antenna element is modeled as a zero-mean white Gaussian process (ZMWGP) and the derived expression is approximated based on low oscillator noise power. Furthermore, the modulation and pulse shaping are not taken into account in the analysis. On the other hand, Georgiadis also modeled the oscillator noise by a ZMWGP and characterized it mathematically – along with other impairments – using the EVM [85]. In this context, it is shown that the expression is valid for any linear modulation techniques. Nevertheless, the pulse shaping is still not accounted for. Finally, it is important to mention the work of Muschallik [86], who derived a CIR approximation as opposed to the widespread EVM. More specifically, the expression assumes a colored oscillator noise, a low power approximation, an orthogonal frequency-division multiplexing (OFDM) signal and does not consider the impact of the symbol rate through the pulse shaping. To the best of the author's knowledge, no expression is available that can efficiently be used in the context of satellite communications systems. In other words, an expression that relies on a predefined phase noise mask that models a colored noise and accounts for SC pulse shaping.

## 1.4 Contributions of this thesis

### 1.4.1 Summary of results

In light of the present literature, this thesis proposes a unified mathematical framework in which any model-based impairment can be characterized. As opposed to the wide range of characterization methods used in the literature (CIR, MSE, EVM, etc.), this work presents a single, harmonized, and generalized characterization method oriented toward satellite link budget calculations. Within the proposed framework, four different types of impairments are thus characterized<sup>17</sup> mathematically: Waveform imperfections, filter distortions, amplifier distortions, and oscillator noise. More precisely, the characterization of these impairments addresses the needs of the satellite

---

<sup>17</sup>Any of the proposed models and expressions can be further refined and generalized depending on the availability of new models or the formulation of new needs.

community and fills the knowledge gaps discussed in the previous section. In this way, it enables all satellite experts to quantify rigorously and quickly their respective impact on present and future satellite communications systems.

Thus, novel CIR expressions are derived for each type of impairment. On the one hand, general formulations of CIR are proposed that can be used for accurate link budget calculations. On the other hand, low-complexity formulations of CIR are proposed to enable quicker assessments of the impact of an impairment on the satellite link. All CIR expressions are carefully validated through numerical simulations. Moreover, new valuable insights are gained on each impairment by analyzing thoroughly the derived expressions and the influence of the involved parameters. Therefore, key engineering trade-offs are exposed that can serve to further optimize future UHTS communications systems. As such, the derived CIR expressions enable a novel technique: The real-time dynamic carrier allocation (DCA) optimization. In particular, the analysis emphasizes that an average capacity increase per user of up to 69.7 Mbits/s can be envisioned in a realistic UHTS scenario. As a last note, the key definitions, findings, and formulas are highlighted to further facilitate the reading of this thesis.

### 1.4.2 Outline of the thesis

**Chapter 2** introduces several concepts treated as prerequisites for a deeper understanding of this thesis. This chapter notably provides the reference framework. As a first step, the considered characterization methodology for the performance evaluation of a satellite communications system is specified. Different definitions of CIR are investigated and their respective subtleties are exposed. Moreover, properties are discussed to develop an intuition on the different types of impairment. The notion of impairment domination and asymptote is also defined. Finally, the system mathematical model is detailed with a particular focus set on the components causing the critical impairments.

**Chapter 3** addresses the mathematical characterization of the critical impairments within the proposed framework. Based on the prerequisites, the waveform imperfections are first characterized. The corresponding CIR is derived and carefully analyzed. In this way, a trade-off is exposed based on the defined parameters. Secondly, the filter distortions are characterized. Two representations of distortions are exposed: The exponential polynomial representation and the pole-zero representation. The different advantages of both representations in terms of CIR applications are shown and valuable insights into the nature of this impairment are gained. Thirdly, the amplifier distortions are characterized. In this context, the single-carrier and multi-carrier CIRs are derived and thoroughly studied. Fourthly, the oscillator noise is characterized. The influence of relevant parameters such as the phase noise mask filter and symbol rate are analyzed in more detail. Approaches to reduce further the complexity of the CIR are also exposed.

**Chapter 4** is dedicated to applications of the derived CIR expressions. Firstly, an example of a contemporary HTS link budget is considered. In this context, it is

emphasized how the amplifier distortions CIR can efficiently be used to further refined link budget calculations. Furthermore, it is shown that the CIRs of the waveform imperfections, filter distortions, and oscillator noise can conveniently complement contemporary link budgets. Besides that, the feasibility of real-time DCA optimization for future UHTS scenarios is demonstrated. An in-depth analysis of allocation gain, speed, and accuracy is performed depending on the considered CIR formula. In the end, the expected UHTS capacity performances are highlighted.

**Chapter 5** contains the conclusions and outlines several directions for future research.

### 1.4.3 List of publications

Part of the results presented in the Chapters 3 and 4 have been published in conference proceedings and journals. The references for these works are listed below. The connection between the papers and the chapters is shown in Table 1.1.

#### Journal papers

- [J1] T. Colin, T. Delamotte and A. Knopp, "Filter Distortions in Ultra High-Throughput Satellites: Models, Parameters and Multicarrier Optimization," in *IEEE Transactions on Signal Processing*, vol. 70, pp. 292-306, 2022, doi: [10.1109/TSP.2021.3138238](https://doi.org/10.1109/TSP.2021.3138238).

#### Conference papers

- [C1] T. Colin, T. Delamotte, R. T. Schwarz and A. Knopp, "Linear Distortions in the Communication Satellite Payload: An Analytical Characterization," *2020 10th Advanced Satellite Multimedia Systems Conference and the 16th Signal Processing for Space Communications Workshop (ASMS/SPSC)*, 2020, pp. 1-8, doi: [10.1109/ASMS/SPSC48805.2020.9268818](https://doi.org/10.1109/ASMS/SPSC48805.2020.9268818).
- [C2] T. Colin, T. Delamotte and A. Knopp, "Distortions Characterization for Dynamic Carrier Allocation in Ultra High-Throughput Satellites," *2021 29th European Signal Processing Conference (EUSIPCO)*, 2021, pp. 1-5, doi: [10.23919/EUSIPCO54536.2021.9616360](https://doi.org/10.23919/EUSIPCO54536.2021.9616360).
- [C3] T. Colin, T. Delamotte and A. Knopp, "Phase Noise Characterization for Ultra High-Throughput Satellite Systems," *2022 International Conference on Communications (ICC)*, 2022, *accepted for publication*.

Table 1.1: Connection between the papers and the chapters

	[J1]	[C1]	[C2]	[C3]
<b>Chapter 2:</b>				
2.2.2 Filters	✓	✓		
2.2.3 Amplifiers			✓	
2.2.4 Oscillators				✓
<b>Chapter 3:</b>				
3.2 Filter distortions	✓	✓		
3.3 Amplifier distortions			✓	
3.4 Oscillator noise				✓
<b>Chapter 4:</b>				
4.1 Link budget refinement	✓	✓	✓	✓
4.2 Link budget optimization	✓	✓	✓	

## 2 | Prerequisites

### Contents

2.1	Methodology for link budget analysis . . . . .	17
2.2	Mathematical system model . . . . .	23

## 2.1 Methodology for link budget analysis

### 2.1.1 General characterization of impairments

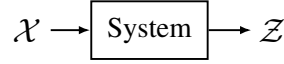


Figure 2-1: General system model

This section is designed to give a first intuition on the performance evaluation of a communications system. By defining different types of impairments and characterizing them in terms of CIR, basic rules and properties follow. They lay the foundations for the next chapters. In this section, the general system model depicted in Fig. 2-1 is considered. The input  $\mathcal{X}$  carries the useful information and is seen from the perspective of a random variable. The output  $\mathcal{Z}$  is the observed impaired information, which is the result of the transformed useful information and a combination of multiple impairments. In this work, the output can be represented as  $\mathcal{Z} = f(\mathcal{X}, \mathcal{Y}_1, \mathcal{Y}_2, \dots)$ , where  $\mathcal{Y}_1, \mathcal{Y}_2, \dots$  are impairments seen as random variables and  $f(\cdot)$  is the system function mixing these random variables together. This, of course, can make us wonder about the definition of useful information. What is left of  $\mathcal{X}$  at the output? Is it possible to separate mathematically the useful information from the impairments? As a first step, the CIR measured at the system output is defined for a given instance of useful information.

#### Definition 1: Instantaneous Carrier-to-Impairment Power Ratio

The instantaneous CIR corresponding to the presented system can be defined for a given realization  $x$  of  $\mathcal{X}$  as follows:

$$\left(\frac{C}{I}\right)(x) = \frac{|\mathbb{E}[\mathcal{Z}|\mathcal{X} = x]|^2}{\mathbb{V}[\mathcal{Z}|\mathcal{X} = x]}$$

This helps to understand the dynamics of the impairment depending on the useful information instance. With this definition, the useful information power corresponds to the power of the average output measured for the same instance  $x$ . Furthermore, the interference power corresponds to the average instantaneous output power away from the average output power, i.e. the variance of the output, for the same instance  $x$ . It is then obvious that, if the system is free of impairments, the denominator is zero and the CIR infinite. To go further, and by considering all possible instances of useful information, a generalized CIR can be expressed.

### Definition 2: Generalized Carrier-to-Impairment Power Ratio

The generalized CIR corresponding to the presented system can be defined as follows:

$$\left(\frac{C}{I}\right) = \frac{\mathbb{E} [|\mathbb{E}[\mathcal{Z}|\mathcal{X}]|^2]}{\mathbb{E} [\mathbb{V}[\mathcal{Z}|\mathcal{X}]]}$$

This definition encompasses all realizations of  $\mathcal{X}$  in a single measure of performance. The generalized CIR averages the useful information power and the interference power. In fact, it corresponds exactly to the inverse of the average EVM defined relative to the average useful information power<sup>1</sup>.

### 2.1.2 Basics on additive Gaussian impairments

To better grasp Definition 2, the most common type of impairments is first discussed: the AG impairment. It is worth reminding that in the specific case of a zero-mean white AG noise, the well-known Shannon-Hartley theorem shows that the CIR is directly linked to the channel capacity [87]. The link is less trivial when considering an arbitrary type of impairment [87].

To start with a first representation of a satellite communications system, a simplified model of a transparent satellite communications system is provided in Fig. 2-2. The complex scalars  $\beta_1$  and  $\beta_2$  represent the linear gains (antennas, amplifiers, etc.), linear losses (free-space, depointing, etc.), and phase shifts (slant path geometry, etc.) in the satellite communications system. The system impairments are denoted

<sup>1</sup>The EVM method is also used to measure the performance of a system, however, it has multiple definitions. Different normalizations with respect to the useful information are sometimes used e.g.  $\max_{\mathcal{X}} (|\mathbb{E}[\mathcal{Z}|\mathcal{X}]|^2)$  as well as different units e.g. % or dB. It can be either defined over one symbol or multiple symbols. In the latter case, the minimum, average and maximum values are used.

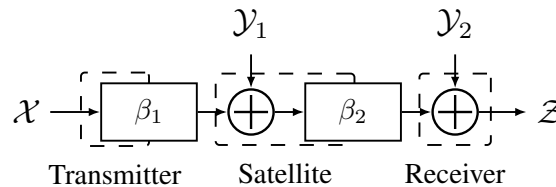


Figure 2-2: Simplified model of a transparent satellite communications system



by  $\mathcal{Y}_1$  and  $\mathcal{Y}_2$ . They are uncorrelated zero-mean AG random variables (either real or complex) with variances  $\sigma_1^2$  and  $\sigma_2^2$ , respectively. Finally, the system output can be expressed as  $Z = \beta_1 \cdot \beta_2 \cdot \mathcal{X} + \beta_2 \cdot \mathcal{Y}_1 + \mathcal{Y}_2$ . By using Definition 2, and assuming that  $\mathbb{E}[|\mathcal{X}|^2] = P$ , the observed output CIR can be developed as:

$$\left(\frac{C}{I}\right) = \frac{|\beta_1|^2 \cdot |\beta_2|^2 \cdot P}{|\beta_2|^2 \cdot \sigma_1^2 + \sigma_2^2}. \quad (2.1.1)$$

This expression enables the introduction of the fundamental decomposition rule of AG impairments below.

### Corollary 1: Decomposition Rule

Let  $\mathcal{X}$ ,  $\mathcal{Y}_1$ , and  $\mathcal{Y}_2$  be three pairwise uncorrelated random variables, which represent the useful information and two additive Gaussian impairments, respectively. If the system is linear, the observed output noise is also Gaussian and the corresponding CIR has the following property:

$$\left(\frac{C}{I}\right)^{-1} = \left(\frac{C}{I_1}\right)^{-1} + \left(\frac{C}{I_2}\right)^{-1}$$

Note that this rule is understood in the sense of generalized CIR. In this example, the CIRs corresponding to respective AG impairments are:

$$\left(\frac{C}{I_1}\right) = \frac{|\beta_1|^2 \cdot \cancel{|\beta_2|^2} \cdot P}{\cancel{|\beta_2|^2} \cdot \sigma_1^2}, \quad \left(\frac{C}{I_2}\right) = \frac{|\beta_1|^2 \cdot |\beta_2|^2 \cdot P}{\sigma_2^2}. \quad (2.1.2)$$

It can be observed that any multiplying complex scalar located after a given AG impairment does not affect its CIR. The first powerful advantage of this rule is that the system can virtually be interpreted as two uncorrelated subsystems, one with impairment  $\mathcal{Y}_1$  and the other with impairment  $\mathcal{Y}_2$ , each with an individual CIR, and which add up at the observed output. The second powerful advantage is that it can be applied to any number of AG impairments. It enables to consider and analyze separately any number of AG impairments whatever the complexity of the system. Finally, a third advantage is that the distribution of the resulting total impairment is known. This is particularly useful for the calculation of the system error probability.

Victim of its success, this rule is widely *overused* – in practice and in the literature – to combine any number of impairments that are not necessarily AG without justification [88, 89, 90].

### 2.1.3 Basics on non-additive Gaussian impairments

To develop further an intuition on the different types of impairments, the two most basic non-AG impairments are now exposed. The most trivial impairment, the *additive impairment*, is defined next.

### Corollary 2: Additive Impairment

Let  $\mathcal{X}$  and  $\mathcal{Y}$  be two uncorrelated random variables, where  $\mathcal{X}$  and  $\mathcal{Y}$  represent the useful information and zero-mean impairment, respectively. If the observed information is  $\mathcal{Z} = \mathcal{X} + \mathcal{Y}$ , then the corresponding generalized CIR given  $\mathcal{X}$  is:

$$\left(\frac{C}{I}\right) = \frac{\mathbb{E}[|\mathcal{X}|^2]}{\mathbb{E}[|\mathcal{Y}|^2]}$$

Additive impairments include, for instance, linear intersymbol interference and adjacent channel interference. Moreover, the instantaneous-to-average power ratio (IAPR)<sup>2</sup> of  $\mathcal{X}$  given  $x$  can be defined as:

$$\mathbb{I}_x[\mathcal{X}] = \frac{|x|^2}{\mathbb{E}[|\mathcal{X}|^2]} . \quad (2.1.3)$$

Since the instantaneous CIR of the additive impairment is  $(C/I)(x) = |x|^2/\mathbb{E}[|\mathcal{Y}|^2]$ , one condition for it to be equal to the generalized CIR is to have a unit IAPR. In case the IAPR is unit for all instances, there is no distinction to be made between both CIR definitions.

Besides additive impairments, a second type of impairment is defined below, which is the *multiplicative impairment*.

### Corollary 3: Multiplicative Impairment

Let  $\mathcal{X}$  and  $\mathcal{Y}$  be two uncorrelated random variables, where  $\mathcal{X}$  and  $\mathcal{Y}$  represent the useful information and impairment, respectively. If the observed information is  $\mathcal{Z} = \mathcal{X} \cdot \mathcal{Y}$ , then the corresponding generalized CIR given  $\mathcal{X}$ :

$$\left(\frac{C}{I}\right) = \frac{|\mathbb{E}[\mathcal{Y}]|^2}{\mathbb{V}[\mathcal{Y}]}$$

Multiplicative impairments include, for instance, oscillator phase noise and amplitude scintillation. In this case, instantaneous and generalized CIRs are equal and there is no distinction to be made between them. In this case, the useful information power is dependent on the statistic of the impairment. This formulation may be a source of misconception since in the literature a unit useful information power is often considered and  $1/\mathbb{V}[\mathcal{Y}]$  is computed as a measure of performance instead [82].

For the sake of visualization, additive and multiplicative impairments are illustrated in Fig. 2-3a and Fig. 2-3b. The interference power  $I$  for a given useful information instance  $x$  is depicted by a dashed circle with its corresponding expression. Fundamentally, it is a measure of the size of uncertainty, illustrated by a *cloud* of scattered points, around the received useful information instance.

<sup>2</sup>The well-known peak-to-average power ratio (PAPR) can be expressed based on this measure as  $\mathbb{P}[\mathcal{X}] = \max_x (\mathbb{I}_x[\mathcal{X}])$ . However, the concept of IAPR is introduced and used because it contains by definition more information than the PAPR.

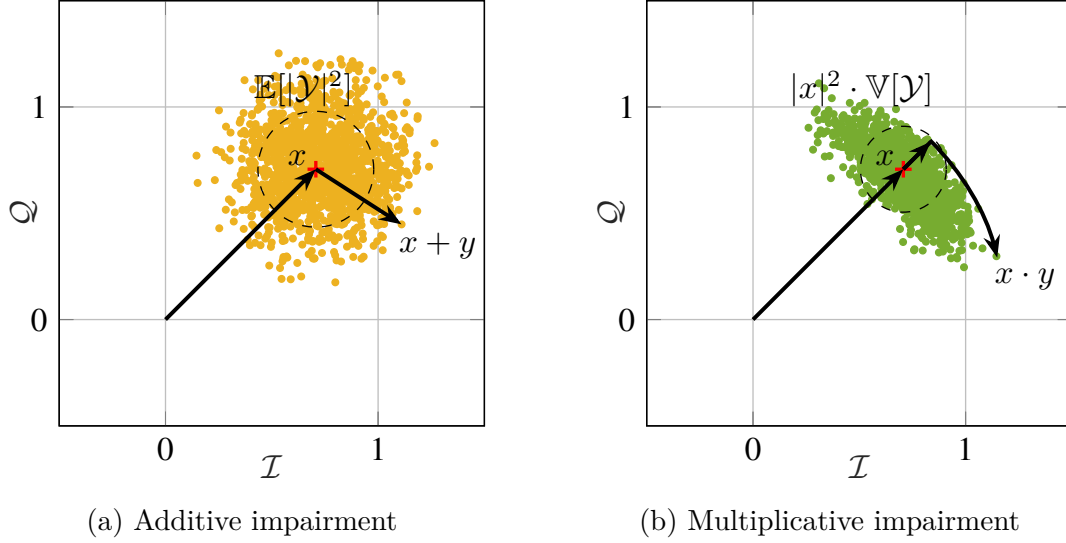


Figure 2-3: Elementary types of impairments

Finally, it should be noted that any system where transformed useful information and impairment are intertwined, leads to *nonlinear impairments*. This is the case, for instance, of  $f(\mathcal{X}, \mathcal{Y}) = \mathcal{X} + \mathcal{Y} \cdot |\mathcal{X}|^2$  (closely related to nonlinear distortions of order 3). In such a case, there is no trivial simplification of the generalized CIR.

### 2.1.4 Impairments domination and asymptotes

After having laid the groundwork for different types of impairments, one last point is to be made. Indeed, in the case of a high number of impairments in the communications systems: Is it possible to derive a CIR characterizing all impairments? Should all impairments actually be taken into account? If not, which impairments can be considered relevant? To answer these questions, the system depicted in Fig. 2-2 is again considered. Typically, when assuming that the uplink noise can be neglected, the total CIR can be denoted as follows:

$$\left(\frac{C}{I}\right) \rightarrow \left(\frac{C}{I_2}\right), \text{ as } \left(\frac{I_2}{I_1}\right) \rightarrow +\infty. \quad (2.1.4)$$

To go into deeper details, an uplink-downlink noise trade-off is exposed in Fig. 2-4. The uplink CIR<sup>3</sup> is arbitrarily chosen equal to  $(C/I_1)_{\text{dB}} = 30$  dB. Establishing the dominance of an impairment over others depends fundamentally on the accepted level of error. In this scenario, the simplification of (2.1.4) is only valid given a maximum error on the total CIR. The notion of percent error is then introduced to measure how close the total CIR is from the asymptote of the downlink CIR. It is defined as follows:

$$E_{\%}(V_{\text{true}}, V_{\text{approx}}) = \left| \frac{V_{\text{true}} - V_{\text{approx}}}{V_{\text{true}}} \right| \cdot 100, \quad (2.1.5)$$

<sup>3</sup>Due to common convention, the logarithmic-scale conversion  $10 \cdot \log_{10}(\cdot)$  is used and denoted by  $(\cdot)_{\text{dB}}$  for compact notations.

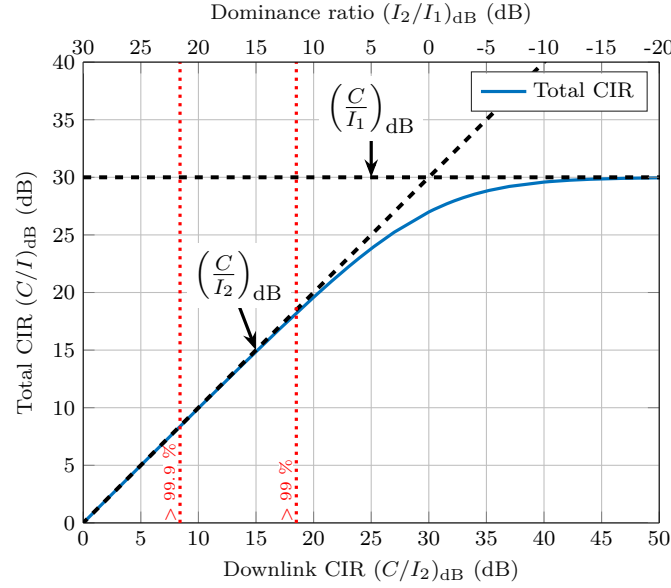


Figure 2-4: Impairment trade-off and domination of CIR

where  $V_{\text{true}}$  and  $V_{\text{approx}}$  are the true value and the approximate value, respectively. Based on this definition, the accuracy can then be expressed as  $A_{\%}(\cdot) = 100 - E_{\%}(\cdot)$ . As reference, the accuracy levels  $A_{\%}((C/I)_{dB}, (C/I_2)_{dB}) = \{99\%, 99.9\%\}$  are displayed with red dotted lines. In other words, a link budget accuracy of 99 % requires a ratio between impairments power of  $(I_2/I_1)_{dB} \approx 11.5$  dB. This implies that all impairments beyond this margin can be neglected. High link budget accuracy can still be achieved when considering only the most critical impairments. In this work, the most critical impairments identified for present and future satellite systems (see Introduction) are considered within this framework. This comprises the AG white noise, waveform imperfections, filter distortions, amplifier distortions, and oscillator noise. Since their respective domination depends – among others – on the considered satellite system architecture and scenario, their behavior in terms of CIR is studied given the relevant impairment parameters and meaningful ranges of values. An investigation is also carried out on meaningful asymptotes since they are a pathway to lower complexity formulas as well as more convenient to apply in practice.

### 2.1.5 Extension to linear time-invariant systems

The primary step toward a characterization of impairments has been based on stochastic theory. To go one step further and be more realistic, an extension to filter theory is required. This allows expanding on the notions of time and frequency. In particular, the useful information instances are defined over a finite period of time and the measurement of the CIR is performed at a given decision instant. Moreover, random processes and sequences of random variables are now considered. Overall, this extension is explained progressively throughout the system description and mathematical model of the next section. Last but not least, two important properties enable

to extend the fundamental decomposition rule (Corollary 1) to linear time-invariant (LTI) systems based on [91]:

- 1) A filtered Gaussian random process remains Gaussian.
- 2) The variance of a filtered Gaussian random process is the variance of the process times the energy of the filter.

## 2.2 Mathematical system model

The next step towards obtaining practical formulas is to explicitly define the system function  $f(\cdot)$ . Due to the wide range of satellite architectures, only the most fundamental *blocks* are described and modeled mathematically<sup>4</sup>. This includes the modulation scheme, filters, amplifiers, and oscillators. These transmission chain blocks are intimately related to the most critical impairments<sup>5</sup>. Thus, the link between them will be made explicit.

### 2.2.1 Modulation scheme

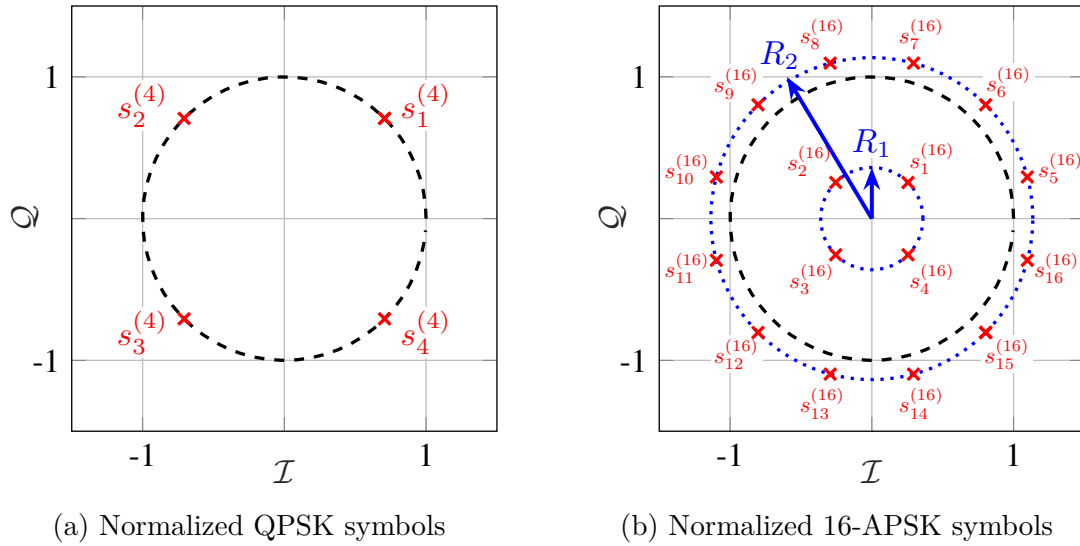


Figure 2-5: Examples of typical satellite modulations [71]

In practical systems, the useful information instances are complex symbols. They rely on a mapping with information bits, which may include an encoding step. More precisely, the information is carried by a sequence of symbols seen as random variables

<sup>4</sup>Some of the most representative and widely accepted mathematical models are presented. If novel superior models are made available, the corresponding updates must be performed. That is why the terminology and concept of *framework* is employed.

<sup>5</sup>From this point, the focus is switched on blocks that are a source of non-AG impairments, since the behavior and decomposition of AG impairments has been made trivial.

$\mathcal{S}_1, \mathcal{S}_2, \dots, \mathcal{S}_{N_s}$ , where  $N_s$  is the number of symbols. Each symbol is assumed to follow a uniform distribution and to be pairwise uncorrelated with other symbols. PSK and APSK modulations can be considered the most common modulations in satellite communication systems and are widely adopted by standards [71, 52].

An example of normalized QPSK and 16-APSK symbol realizations are depicted in Fig. 2-5a and Fig. 2-5b, respectively. Since QPSK and 16-APSK symbols are assumed to follow a uniform distribution, it can be written that  $\mathcal{S}_p \sim \mathcal{U}\{s_1^{(4)}, s_2^{(4)}, s_3^{(4)}, s_4^{(4)}\}$  and  $\mathcal{S}_p \sim \mathcal{U}\{s_1^{(16)}, s_2^{(16)}, \dots, s_{16}^{(16)}\}$ ,  $\forall p \in \{1, 2, \dots, N_s\}$ . The possible symbol realizations for QPSK and 16-APSK modulations can be expressed in polar form as:

$$s_i^{(4)} = e^{j((i-1)\frac{\pi}{2} + \frac{\pi}{4})}, \quad i \in \{1, 2, 3, 4\}, \quad (2.2.1a)$$

$$s_i^{(16)} = \begin{cases} R_1 \cdot e^{j((i-1)\frac{\pi}{2} + \frac{\pi}{4})}, & i \in \{1, 2, 3, 4\} \\ R_2 \cdot e^{j((i-5)\frac{\pi}{6} + \frac{\pi}{12})}, & i \in \{5, 6, \dots, 16\} \end{cases}, \quad (2.2.1b)$$

respectively, where  $R_1$  and  $R_2$  represent the 16-APSK inner and outer ring radii. By definition,  $R_1 < 1$  and  $R_2 > 1$ . Both linear modulation schemes are designed with zero-mean,  $\mathbb{E}[\mathcal{S}_p] = 0$ , and normalized power,  $\mathbb{E}[|\mathcal{S}_p|^2] = 1$ ,  $\forall p \in \{1, 2, \dots, N_s\}$ . While most of the formulas derived in this work are independent of the linear modulation scheme being used, a distinction must be made in the case of nonlinear distortions. Indeed, although the QPSK IAPR is always unit, i.e.  $\mathbb{I}_{s_i^{(4)}}[\mathcal{S}_p] = 1$ ,  $\forall i \in \{1, 2, 3, 4\}$ ,  $\forall p \in \{1, 2, \dots, N_s\}$ , the 16-APSK IAPR is not. Indeed, it can be expressed as:

$$\mathbb{I}_{s_i^{(16)}}[\mathcal{S}_p] = \begin{cases} R_1^2, & i \in \{1, 2, 3, 4\} \\ R_2^2, & i \in \{5, 6, \dots, 16\} \end{cases}, \quad \forall p \in \{1, 2, \dots, N_s\}. \quad (2.2.2)$$

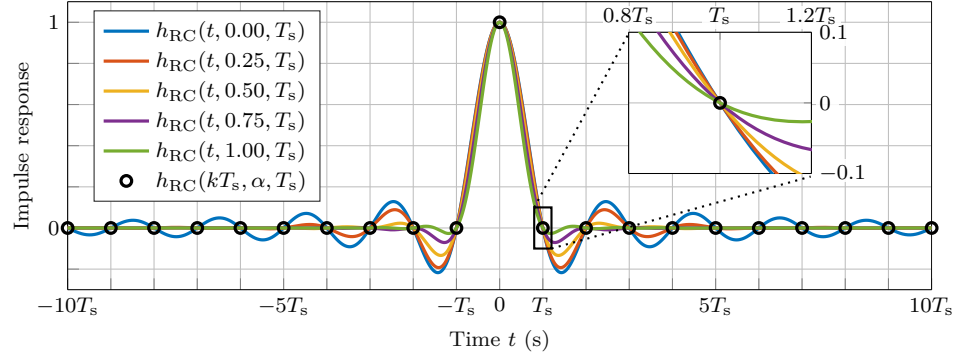
This leads to different modulation coefficients, as described in Appendix B.4, between both modulation schemes and thus, different CIR formulas in nonlinear cases. In the case of APSK modulation, the modulation coefficients are dependent on the IAPR. However, to be more rigorous, it should be noted that these expressions can be reduced to a single parameter and performance indicator, which is the ring ratio  $v_1 = R_2/R_1$ . In fact, it is the ring ratio that is usually optimized for a given configuration (coding rate, input back-off, etc.) [71]. For higher order modulations, multiple ring ratios need to be accounted for.

## 2.2.2 Filters

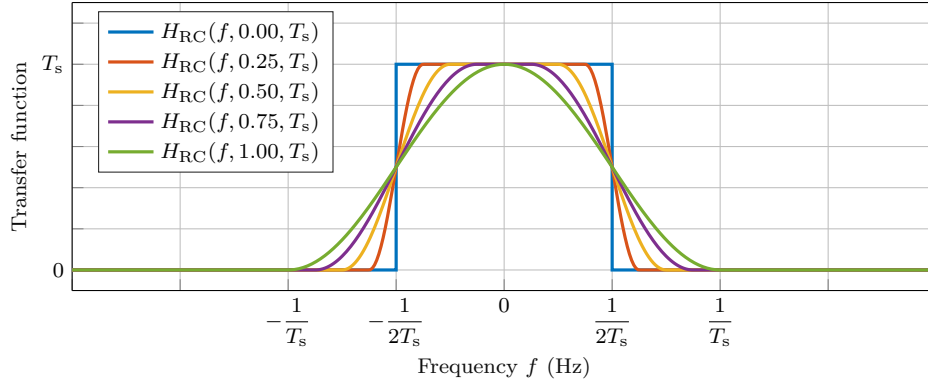
### Pulse shaping and detection

In practical systems, each symbol is associated to a pulse in order to carry the information over the transmission medium, the so-called *channel*. Indeed, two important requirements demand the use of a pulse shaping: limiting the ISI as well as limiting adjacent channel interference (ACI) by generating a band-limited carrier.

The pulse shaping traditionally used in satellite communication systems relies on the RC filter [71, 52], denoted by  $h_{RC}(t, \alpha, T_s)$ . For more details, its mathematical



(a) Impulse response



(b) Transfer function

Figure 2-6: raised-cosine (RC) filter characteristics

description is provided in Appendix A.1. The RC impulse response and transfer function are illustrated in Fig. 2-6. The primary property of the RC is to comply with the Nyquist ISI-free criterion [92], which can be expressed as follows:

$$h_{\text{RC}}(kT_s, \alpha, T_s) = \begin{cases} 1, & k = 0 \\ 0, & k \in \mathbb{Z}^* \end{cases}, \quad \forall \alpha \in [0; 1], \quad (2.2.3)$$

where  $T_s$  and  $\alpha$  represent the symbol period and roll-off, respectively. This property can be observed in Fig. 2-6a. The roll-off is an important parameter enabling the tuning of the pulse shaping. It is, by design, defined in the interval  $[0; 1]$  and expresses the excess bandwidth with respect to the Nyquist frequency as illustrated in Fig. 2-6b. Indeed, the carrier bandwidth is defined as  $B = (1 + \alpha)R_s$ , where  $R_s$  is the symbol rate. The roll-off plays a key role in the next chapter when introduced with new types

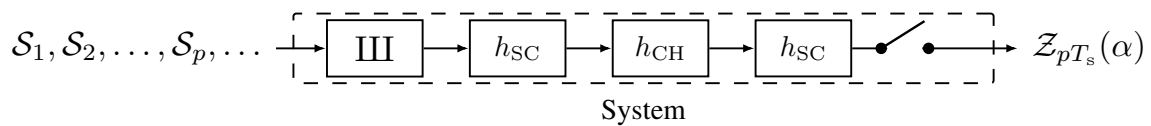


Figure 2-7: Simplified system model including pulse shaping and detection

of impairments.

To bring the RC property into the scope of CIR, the system model depicted in Fig. 2-7 is considered. Among the transmitted symbols, the useful information can be arbitrarily chosen as  $\mathcal{S}_p$ . The RC filter is decomposed into its pulse shaping and detection filter counterpart. Both are SC filters based on the convolution definition:  $h_{RC}(t, \alpha, T_s) = (h_{SC}(\cdot, \alpha, T_s) * h_{SC}(\cdot, \alpha, T_s))(t)$ . In the end, the output of the system fundamentally depends on the channel between these filters. Its impulse response is denoted by  $h_{CH}(t)$ . In the case of a simple channel with impulse response  $h_{CH}(t) = \beta \cdot \delta(t)$ ,  $\beta \in \mathbb{C}^*$ , the observed impaired information defined at optimal decision instant  $pT_s$  can be expressed and decomposed as follows:

$$\mathcal{Z}_{pT_s}(\alpha) = \underbrace{\beta \cdot \mathcal{S}_p \cdot h_{RC}(0, \alpha)}_{\text{Transformed useful information}} + \underbrace{\beta \cdot \sum_{\substack{k=p-(N_s-1) \\ k \neq 0}}^p \mathcal{S}_{p-k} \cdot h_{RC}(k, \alpha)}_{\text{Zero-mean additive impairment}} . \quad (2.2.4)$$

For more convenient calculations and compact notations, expressions are normalized by the symbol period whenever it is possible. Here,  $h_{RC}(k, \alpha)$  denotes  $h_{RC}(k, \alpha, 1) = h_{RC}(kT_s, \alpha, T_s)$ . Based on Corollary 2, the system CIR<sup>6</sup> is:

$$\left(\frac{C}{I}\right)(\alpha) = \frac{|h_{RC}(0, \alpha)|^2}{\sum_{k \in \mathbb{Z}^*} |h_{RC}(k, \alpha)|^2} \rightarrow +\infty , \quad (2.2.5)$$

which means that, for such a channel, the system is free of impairment thanks to the Nyquist ISI-free criterion (2.2.3),  $\forall \alpha \in [0; 1]$ ,  $\forall p \in \{1, 2, \dots, N_s\}$ , and for any linear modulation. On top of that, this CIR formula related to ISI is also valid for any channel composed of complex scalars and AG impairments<sup>7</sup> such as the aforementioned example of a simplified bent-pipe satellite system. In such a case, the total CIR is equal to the AG impairments CIR.

## System constraints

It is clear that the definition of SC pulse shaping and detection filters is based on idealistic premises, which do not take into account practical system constraints. In this work, the term *waveform imperfections* designates the impairment induced by the constraints applied to both the SC pulse shaping and detection filters.

The first constraint comes from the requirement of system causality. Indeed, there is a contradiction between the time infiniteness of the SC definition<sup>8</sup> and the time finiteness required to make the filter realizable and causal. In practical systems, the SC filters are shortened<sup>9</sup>. This shortening can be modeled mathematically by a

<sup>6</sup>The more general and rigorous CIR proof is provided in Appendix C.1.

<sup>7</sup>In case of AG impairments, the detection filter is a matched filter, which maximizes the CIR.

<sup>8</sup>Since one of the purposes of the SC is to generate a bandlimited carrier, the Heisenberg uncertainty principle implies that the impulse response must be infinite in time.

<sup>9</sup>They are also time-shifted, but the constant time delays do not play a role in the CIR expressions



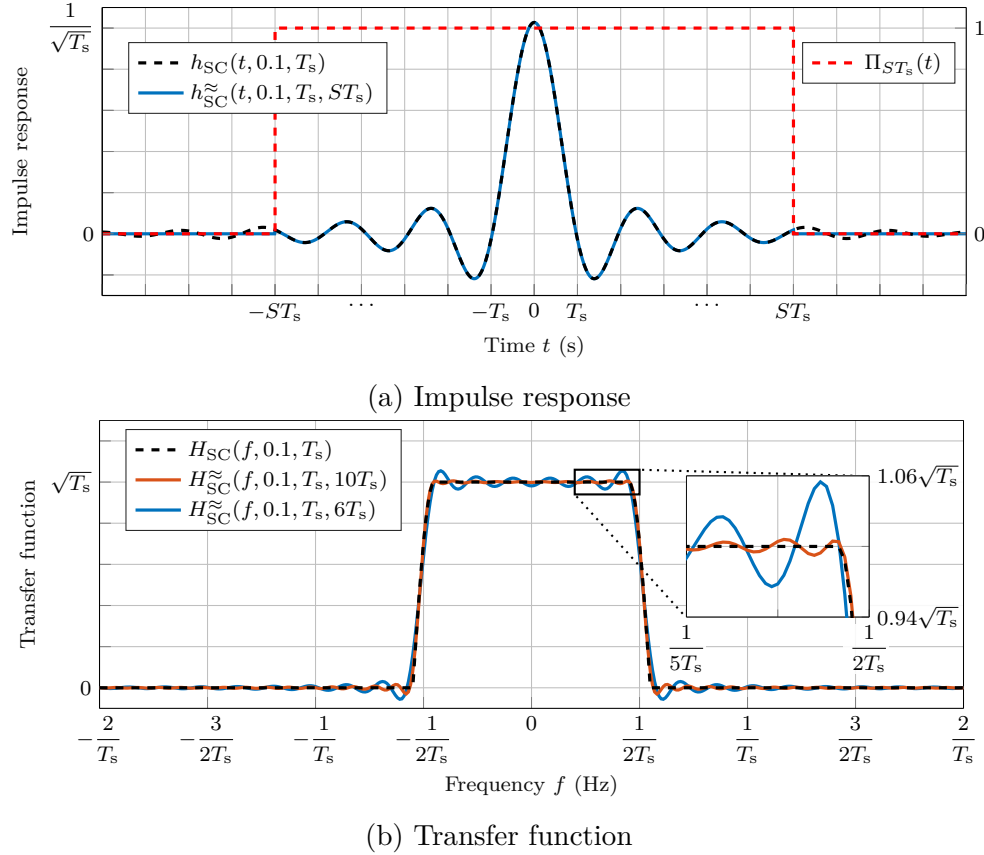


Figure 2-8: Time-limited SC filter characteristics

multiplicative function denoted by  $g_{\text{WI}}(t, \cdot)$ . This function is dependent on further parameters such as the length of the shortening. Thus, the constrained SC filter is denoted and defined by  $h_{\text{SC}}^{\approx}(t, \alpha, T_s, \cdot) = h_{\text{SC}}(t, \alpha, T_s) \cdot g_{\text{WI}}(t, \cdot)$ . By default, the rectangular function is commonly used, i.e.  $g_{\text{WI}}(t, ST_s) = \Pi_{ST_s}(t)$ , where  $S$  represents the one-sided span<sup>10</sup> and expresses the number of symbol periods  $T_s$  on which the SC is considered nonzero. The corresponding time-limited SC is illustrated in Fig. 2-8. Restricting the SC in time means that it only approximates the ideal characteristic both in time and frequency domains. In frequency domain, it leads to a Gibbs phenomenon visible for shorter spans. In time domain, it leads to an imperfect reconstruction of the RC in the receiver-side and thus, leads to ISI. In other words, the Nyquist ISI-free criterion (2.2.3) can no longer be fulfilled.

A second possible system constraint is the digitalization of the carrier that can occur on-board the satellite. Although it is possible to be free of impairment in the ideal case considering a sampled carrier fulfilling Nyquist-Shannon sampling theorem [93], it is no longer the case under a time constraint. In the presence of digitalization, the multiplicative function becomes  $g_{\text{WI}}(t, ST_s, F_s) = \Pi_{ST_s}(t) \cdot \frac{1}{\sqrt{F_s}} \cdot \text{III}_{\frac{1}{F_s}}(t)$ , where

due to the timing recovery loop compensation.

<sup>10</sup>This definition is more convenient for the CIR calculations as opposed to the double-sided span. For the sake of simplicity, the same span is used for the pulse shaping and detection filters.

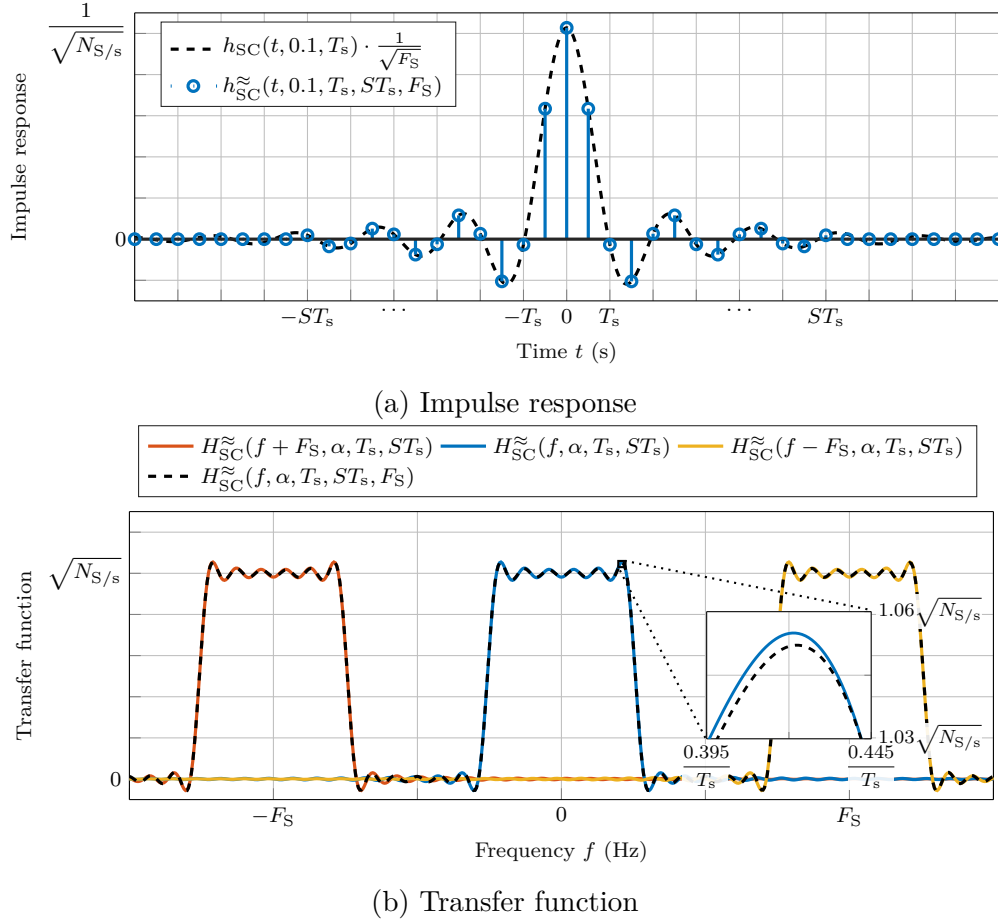


Figure 2-9: Sampled time-limited SC filter characteristics

$\text{III}_{\frac{1}{F_S}}(t)$  is a Dirac comb sampling the carrier every  $\frac{1}{F_S}$ . This enables to still describe and interpret expressions in a general analog continuous sense. Thus, a meaningful parameter can be introduced: the number of samples per symbol, which is denoted and defined by  $N_{S/s} = F_S/R_s$ . Indeed, the sampled time-limited SC can be reformulated in terms of  $N_{S/s}$  as follows:

$$\begin{aligned}
 h_{SC}^{\approx}(t, \alpha, T_s, ST_s, F_S) &\stackrel{\text{Definition}}{=} h_{SC}(t, \alpha, T_s) \cdot \left( \Pi_{ST_s}(t) \cdot \frac{1}{\sqrt{F_S}} \cdot \text{III}_{\frac{1}{F_S}}(t) \right) \\
 &\stackrel{\text{Dirac comb definition}}{=} \sum_{n \in \mathbb{Z}} h_{SC}\left(\frac{n}{F_S}, \alpha, T_s\right) \cdot \Pi_{ST_s}\left(\frac{n}{F_S}\right) \cdot \frac{1}{\sqrt{F_S}} \cdot \delta\left(t - \frac{n}{F_S}\right) \\
 &\stackrel{N_{S/s} \text{ reformulation}}{=} \sum_{n \in \mathbb{Z}} h_{SC}\left(n, \alpha, N_{S/s}\right) \cdot \Pi_{SN_{S/s}}(n) \cdot \delta\left(t - \frac{n}{F_S}\right) \\
 &\stackrel{\text{Sum truncation}}{=} \sum_{n=-SN_{S/s}}^{SN_{S/s}} h_{SC}\left(n, \alpha, N_{S/s}\right) \cdot \delta\left(t - \frac{n}{F_S}\right). \quad (2.2.6)
 \end{aligned}$$

This expression is used to derive the CIR related to waveform imperfections in the next chapter. The characteristic of the sampled time-limited SC is depicted in Fig. 2-9. In frequency domain, the sampling leads to a replication of the transfer function of the time-limited SC every  $F_s$ . Furthermore, time limitation leads to an infinite spectrum for each transfer function. Therefore, the carrier suffers from aliasing.

In the end, the parameters  $S$  and  $N_{S/s}$  are key parameters to control the waveform imperfections. In fact, although increasing these parameters directly mitigates the effects of the impairments, it also causes an increase in the system load and complexity. Therefore, an appropriate trade-off between accepted levels of impairments and accepted system constraints is required. It is worth noting that an approach to mitigate this type of impairment can be to use a window function [94], which means optimizing the function  $g_{WI}(t, \cdot)$ . However, when the channel is not trivial choosing the appropriate window function is also not trivial. Instead, filter compensation methods such as equalization tend to be more used in practice.

### Linear components and satellite filters

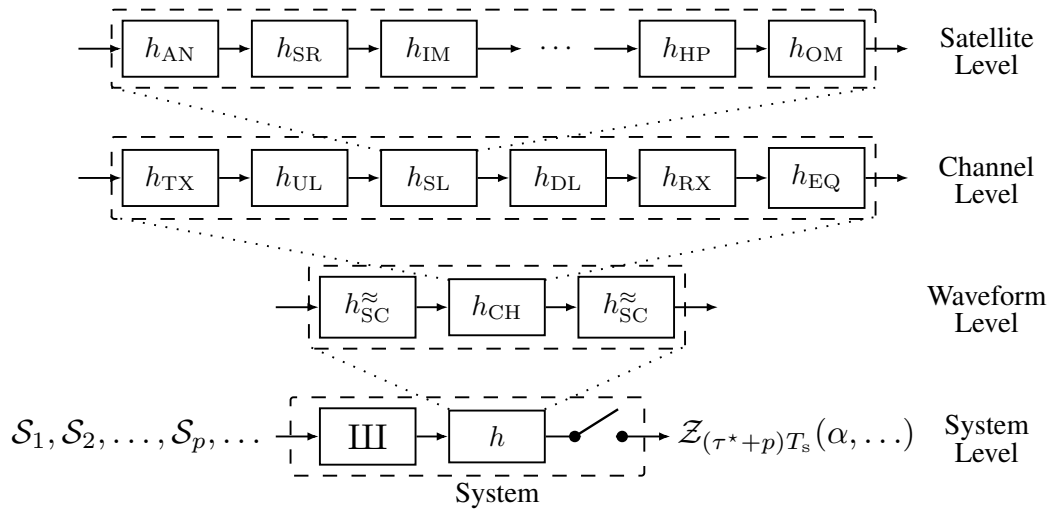


Figure 2-10: Overview of the filters encapsulation

In practical systems, the channel is not only composed of AG impairments, but also non-AG impairments, which can be as critical. Indeed, the channel of satellite systems is composed – among others – of multiple imperfect components. Some are filters or linear components modeled as filters. They are all distorting the information, which causes ISI at the system output<sup>11</sup>.

Fortunately, filters can be represented with as much refinement as it is necessary due to the LTI system property. A typical encapsulation of filters is depicted in Fig. 2-10. The system impulse response is denoted by  $h(t)$  and takes into account all *filter*

<sup>11</sup>Mechanisms do exist to compensate ISI such as the maximum-likelihood sequence estimator [92] (optimal) or the fractionally-spaced equalizer [52] (suboptimal). However, their implementation is restricted due to the involved cost and complexity added to the user receiver terminal.

*distortions* of the system. By definition, it is expressed as  $h(t) = (h_{\text{SC}}^{\approx}(\cdot, \alpha, T_s, \cdot) * h_{\text{SC}}^{\approx}(\cdot, \alpha, T_s, \cdot) * h_{\text{CH}}(\cdot))(t)$ . At the channel level,  $h_{\text{TX}}$ ,  $h_{\text{UL}}$ ,  $h_{\text{SL}}$ ,  $h_{\text{DL}}$ ,  $h_{\text{RX}}$  and  $h_{\text{EQ}}$  represent the transmitter, uplink channel, satellite, downlink channel, receiver, and optional equalization filter impulse responses, respectively. At the satellite level,  $h_{\text{AN}}$ ,  $h_{\text{SR}}$ ,  $h_{\text{IM}}$ ,  $h_{\text{HP}}$ ,  $h_{\text{OM}}$  represent the satellite antenna, the satellite receiver, the IMUX, the satellite HPA, and OMUX filter impulse responses, respectively. Table 2.1 lists the characteristics of typical filter distortions appearing in the satellite communication payload. By convention, filter distortions are characterized in frequency domain. The characteristic of most of the components is described in terms of a polynomial approximation of gain and group delay. Mathematically, the gain and group delay of a transfer function  $H(f)$  can be expressed as follows:

$$G_{\text{dB}}(f) = 10 \cdot \log_{10} (|H(f)|^2) , \quad (2.2.7a)$$

$$D(f) = - \frac{1}{2\pi} \frac{d(\arg(H(f)))}{df} . \quad (2.2.7b)$$

From this formulation, the transfer function  $H(f)$  can directly be reformulated in terms of gain and group delay as:

$$H(f) \stackrel{\text{Polar form}}{=} |H(f)| \cdot e^{j \cdot \arg(H(f))} \\ \stackrel{\substack{\text{Inversion} \\ \text{of (2.2.7a)} \\ \text{and (2.2.7b)}}}{=} e^{\xi \cdot G_{\text{dB}}(f) - j 2\pi \cdot \int D(f) df} , \quad (2.2.8)$$

where  $\xi = \ln(10)/20$  is a factor coming from the decibel-to-linear scale conversion of the gain. In other words, the gain and group delay are orthogonal to each other in frequency and associated with the real part and imaginary part, respectively, of an exponential representation of  $H(f)$ . Since accounting for the distortions of all linear components means multiplying their transfer function in frequency domain,

Table 2.1: Typical filter distortions characteristics

Components	Gain	Group delay	References
Antennas (AN), coaxes (CX), waveguides (WG)	Polynomial <sup>b</sup> + ripples	Polynomial <sup>b</sup> + ripples	[67]
Satellite receiver (SR)	Polynomial <sup>b</sup>	Polynomial <sup>b</sup>	[67]
IMUX (IM) filter <sup>a</sup>	10-4-4 <sup>c</sup> Chebyshev or elliptic		[95, 96, 97]
HPA (HP)	Polynomial <sup>b</sup> + ripples	Polynomial <sup>b</sup> + ripples	[67]
OMUX (OM) filter <sup>a</sup>	6-2-0 <sup>c</sup> Chebyshev or elliptic		[97, 55, 56]

<sup>a</sup>Satellite filters are critical sources of filter distortions.

<sup>b</sup>Polynomial's degree ranges typically from one to four.

<sup>c</sup>Poles, transmission zeros and additional zeros.

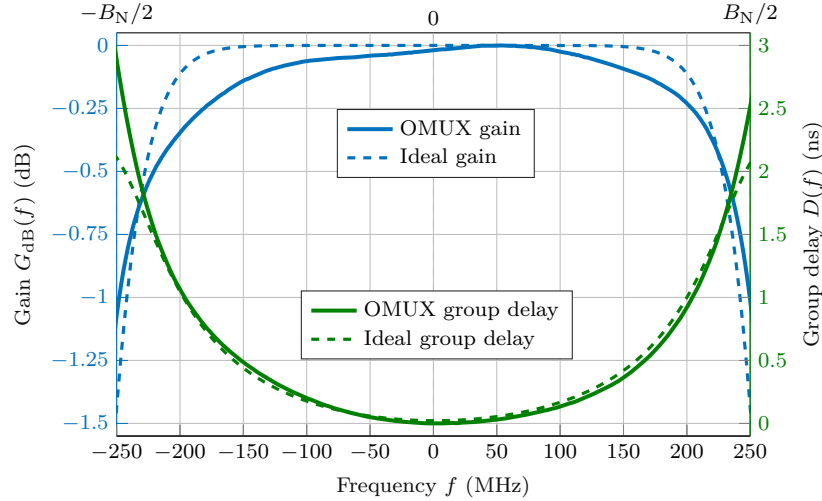


Figure 2-11: Typical wideband OMUX filter characteristics

the transfer function of the system can be obtained simply by adding up the gain and group delay of the components. More generally, the gain and group delay variations are measured or estimated over the whole channel bandwidth. For instance, it is common to observe a gain slope (first-degree polynomial) in antennas, coaxes, and waveguides components, whereas the group delay of these components can sometimes be described by a cubic characteristic (higher-degree polynomial) [67]. Gain and group delay ripples can arise from the mismatch between RF equipment, such as between a traveling-wave tube amplifier (TWTA)<sup>12</sup> and isolator, as well as from multipath between components.

As opposed to the previous approximations, the complete gain and group delay characteristics of the major sources of filter distortions must be taken into account, most generally the IMUX<sup>13</sup> and OMUX characteristics. The distortions characteristic of a typical wideband OMUX transfer function  $H_{OM}(f)$  is depicted in Fig. 2-11. This characteristic is based on the DVB-S2x data points [52] and has been re-scaled to a nominal bandwidth  $B_N = 500$  MHz using the recommended scaling formulas [98]. Furthermore, this characteristic is by design related to the conventional Chebyshev type II filter [99]. As a point of comparison, a five-pole Chebyshev type II filter characteristic is provided to highlight the asymmetry and imperfections of practical designs. Despite guiding principles in the design of IMUX and OMUX, each design is inherently unique in practice. Since analytical design techniques are more limited and computational power has been steadily increasing over the years, equipment suppliers tend to use computer-aided optimization to achieve the final design [55], which leads to very specific locations of poles and zeros.

Filter distortions are not specific to the satellite, they can arise in the user receiver

<sup>12</sup>The TWTA is one of the two most common types of satellite HPA along with the solid-state power amplifier (SSPA).

<sup>13</sup>In processing payloads, the IMUX filtering is performed at least partially by the OBP. It offers the possibility of improving the filtering and thus, limiting the impairments entailed by the IMUX.

equipment, which is often aimed at being low-cost [52]. In the context of direct-to-home (DTH) forward link, the LNB causes simultaneously gain ripple and gain slope, whereas the coax cable only introduces a gain slope, which is proportional to its length. On top of that, these filter distortions are particularly hard to predict, since the residual gain slope varies quite significantly depending on the model of the LNB, and the length and quality of the coax cable. However, these impairments are generally less critical than the ones of the satellite multiplexers filter. Therefore, the user receiver equipment filter distortions will not be the focal point of this work.

To extend the CIR to the concept of waveform imperfections and filter distortions, the following generic formula can be considered:

$$\left(\frac{C}{I}\right)^{\star}(\alpha, T_s, h) = \frac{|h(\tau^{\star}T_s)|^2}{\sum_{k \in \mathbb{Z}^{\star}} |h((\tau^{\star} + k)T_s)|^2}, \quad (2.2.9)$$

where  $\tau^{\star}$  is the optimal decision instant offset relative to the symbol period  $T_s$ , which maximizes the CIR. Indeed,  $\tau^{\star}$  is not necessarily zero anymore, since frequency asymmetries introduced by distortions can lead to a residual time offset. The CIR defined at optimal decision instant is denoted by  $(C/I)^{\star}$ . More details on the CIR proof are available in Appendix C.1. One feature of ISI impairments is that the interference power scales proportionally to the transmitted useful information power. Thus, increasing the transmitted information power does not improve the CIR. This effect can be recognized in (2.2.9) from the fact that the expression is independent of the linear modulations being involved. In the end, it is especially important to design components with gain and group delay as flat as possible, or put in another way, as independent of the frequency as possible.

### 2.2.3 Amplifiers

In practical systems, the satellite HPA is the component most commonly known for being one of the critical sources of impairment<sup>14</sup>. The HPA causes mostly nonlinear distortions and, to some extent, linear distortions<sup>15</sup>. In this work, the term *amplifier distortions* designate both types of distortions. The system including the satellite HPA is illustrated in Fig. 2-12. The HPA function is denoted by  $g_{\text{HP}}(\cdot)$ . Due to the

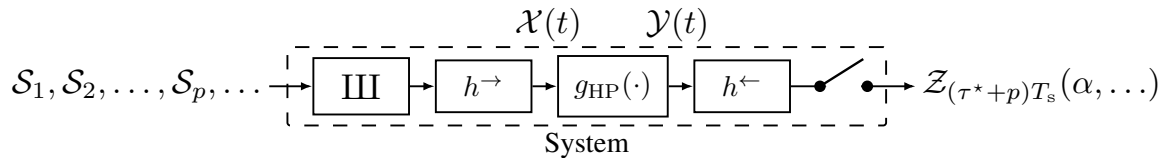


Figure 2-12: Simplified single-carrier system model including satellite HPA

<sup>14</sup>Other amplifiers exist in the system, such as the transmitter HPA, but are not the main focus of this work.

<sup>15</sup>As previously mentioned under the umbrella of filter distortions.

nonlinear nature of this function, a distinction between pre-HPA and post-HPA filters is required. The pre-HPA and post-HPA system impulse responses are represented by  $h^{\rightarrow}$  and  $h^{\leftarrow}$ , respectively. It means that, even though the system is nonlinear time-invariant (NTI), the pre-HPA and post-HPA subsystems are LTI and the same properties apply. It is worth noting that this simplified system model is compatible with Wiener-Hammerstein HPA model. This model not only takes into account the HPA nonlinear function, but also a pre-HPA and post-HPA filters, denoted by  $h_{\text{HP}}^{\rightarrow}$  and  $h_{\text{HP}}^{\leftarrow}$ . These filters model the filter distortions entailed by the HPA [58, 100]. A simple, yet an insightful model for  $g_{\text{HP}}(\cdot)$  is the memoryless<sup>16</sup> Saleh model. The HPA output based on the Saleh model can be expressed as:

$$\begin{aligned} \mathcal{Y}(t) &= g_{\text{HP}}(\mathcal{X}(t)) \\ &\stackrel{\text{Quadrature representation}}{=} \mathcal{X}(t) \cdot \left( r_{\text{HP}}(|\mathcal{X}(t)|^2) + j \cdot i_{\text{HP}}(|\mathcal{X}(t)|^2) \right) \\ &\stackrel{\text{Saleh definition}}{=} \mathcal{X}(t) \cdot \left( \frac{\alpha_r}{(1 + \beta_r |\mathcal{X}(t)|^2)} + j \cdot \frac{\alpha_i |\mathcal{X}(t)|^2}{(1 + \beta_i |\mathcal{X}(t)|^2)^2} \right), \end{aligned} \quad (2.2.10)$$

where  $\alpha_r = 1.90947$ ,  $\beta_r = 1.07469$ ,  $\alpha_i = 4.35023$ , and  $\beta_i = 2.33525$ . They are empirical coefficients proposed by Saleh in [101] for the modeling of a typical<sup>17</sup> normalized<sup>18</sup> TWTA<sup>19</sup> characteristic. The transformation can be decomposed into a real part and imaginary parts, which are represented by  $r_{\text{HP}}(\cdot)$  and  $i_{\text{HP}}(\cdot)$ , respectively.

Graphically, it is common to introduce the so-called AM/AM and AM/PM representations, which are depicted<sup>20</sup> in Fig. 2-13. On the one hand, the AM/AM corresponds to the conversion between the input instantaneous power  $P_{\text{HP}}^{\text{in}} = |\mathcal{X}(t)|^2$  and the output instantaneous power  $P_{\text{HP}}^{\text{out}} = |\mathcal{Y}(t)|^2$ . On the one hand, the AM/PM corresponds to the conversion between the input instantaneous power and output phase offset  $\Psi_{\text{HP}}^{\text{out}} = (\arg(\mathcal{Y}(t)) - \arg(\mathcal{X}(t))) \cdot (180/\pi)$ . From this perspective, two extreme regions can be identified. The *linear region* represents the region where the HPA function is quasi-linear. This means that  $\mathcal{Y}(t) \rightarrow \alpha_r \cdot \mathcal{X}(t)$  as  $P_{\text{HP}}^{\text{in}} \rightarrow 0$ . In this region, the amplifier's instantaneous output power is lower, but the output tends not to be impaired by the HPA. On another side, the *nonlinear region* represents the region where the HPA function is near-saturation. In the case of the present normalized characteristic, it is defined as  $P_{\text{HP}}^{\text{in}} \rightarrow 1$ . In this region, the amplifier instantaneous output power is higher, but the output tends to be more impaired by the HPA. To be more exact, input realizations with different non-unit IAPR get different instantana-

<sup>16</sup>In fact, the widespread qualification of *memoryless* can be misleading. Indeed, the function is always applied to a filtered signal (at least pulse-shaped) and thus, causes at least weak memory effects in the form of ISI.

<sup>17</sup>In the sense that no pre-compensation mechanisms is considered.

<sup>18</sup>As the normalized characteristic is considered, it implies that the scaling of the HPA, which corresponds to the output saturation power, is incorporated in the post-HPA filter.

<sup>19</sup>In the case of an SSPA, other models such as the Rapp model [102] are more realistic for the AM/AM conversion.

<sup>20</sup>For the sake of compactness, the notation  $(\cdot)_{\text{dB}}$  is dropped from this point for any asymptote displayed on a graph. The related quantities are implicitly converted to the decibel scale.

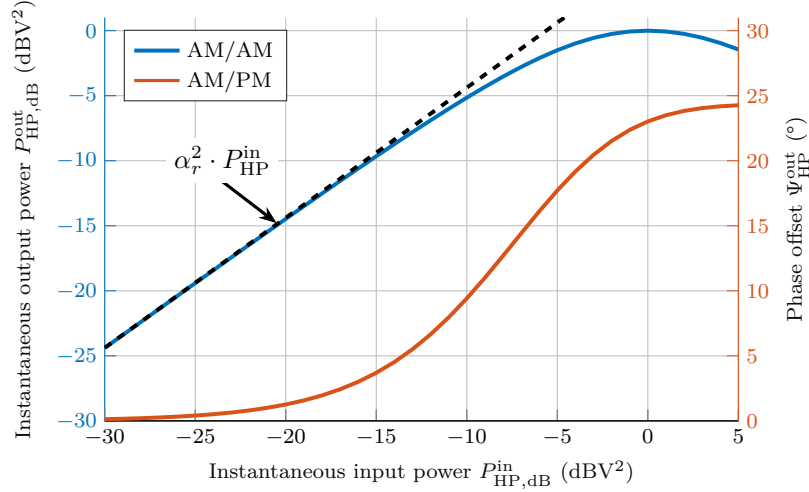


Figure 2-13: Typical normalized HPA characteristics

neous output powers and phase offsets. It is this asymmetry that is the essence of the nonlinear impairments<sup>21</sup>. That is why, a trade-off must be considered between the increase of the useful information power and the decrease of the impairment power. In the end, this trade-off is dependent on the selected input mean power<sup>22</sup>.

Although the calculation of the system CIR can be performed using the expression (2.2.10), it is particularly insightful to define the approximated polynomial representation of the Saleh model as follows:

$$\mathcal{Y}(t) \approx \mathcal{X}(t) \cdot \left( \sum_{k=0}^{N_{AD}} \gamma_{2k+1}(\bar{P}_{HP}^{in}(t)) \cdot |\mathcal{X}(t)|^{2k} \right), \text{ as } \begin{cases} |\mathcal{X}(t)|^2 \approx \bar{P}_{HP}^{in}(t) \\ N_{AD} \rightarrow +\infty \end{cases}, \quad (2.2.11)$$

where  $\{\gamma_{2k+1}(\bar{P}_{HP}^{in}(t))\}_{0 \leq k \leq N_{AD}}$  are the complex coefficients resulting from the Taylor approximation of (2.2.10) using  $|\mathcal{X}(t)|^2 \approx \bar{P}_{HP}^{in}(t)$ . To be more accurate, this latter condition is only true if the approximation holds for the instantaneous power of all realizations, i.e.,  $|x(t)|^2 \approx \bar{P}_{HP}^{in}(t)$ ,  $\forall x(t)$ . Thus, it is natural to define  $\bar{P}_{HP}^{in}(t)$  such as to correspond to the average input power, i.e.,  $\bar{P}_{HP}^{in}(t) = \mathbb{E}[|\mathcal{X}(t)|^2]$ . It means that equality in (2.2.11) can be achieved for a unit IAPR, else it is an approximation.

In fact, this approximation definition holds only for a given time  $t$ . For the sake of simplicity, the approximation is generalized to all  $t$  by defining the mean input power

<sup>21</sup>If all input realizations have a unit IAPR, they all have the same fixed output power and phase offset. In other words, they are theoretically free of impairments entailed by the HPA due to the scaling invariance of the CIR.

<sup>22</sup>The concept of input back-off may be equivalently used after normalizing the quantity by the input saturation power.



per symbol as follows:

$$\begin{aligned}
\bar{P}_{\text{HP}}^{\text{in}} &= \frac{1}{N_s} \cdot \int_{\mathbb{R}} \bar{P}_{\text{HP}}^{\text{in}}(t) dt \\
&= \frac{1}{N_s} \cdot \int_{\mathbb{R}} \mathbb{E}[|\mathcal{X}(t)|^2] dt \\
&= \frac{1}{N_s} \cdot \int_{\mathbb{R}} \mathbb{E} \left[ \left| \sum_{p=0}^{N_s-1} \mathcal{S}_q \cdot h^{\rightarrow}(t - qT_s) \right|^2 \right] dt \\
&\stackrel{\substack{|z|=zz^*, \\ \text{expectation} \\ \text{linearity}}}{=} \frac{1}{N_s} \cdot \int_{\mathbb{R}} \sum_{q_1=0}^{N_s-1} \sum_{q_2=0}^{N_s-1} \mathbb{E}[\mathcal{S}_{q_1} \mathcal{S}_{q_2}^*] \cdot h^{\rightarrow}(t - q_1T_s) h^{\rightarrow*}(t - q_2T_s) dt \\
&\stackrel{\substack{\text{Zero-mean,} \\ \text{unit-power,} \\ \text{uncorrelated} \\ \text{symbols}}}{=} \frac{1}{N_s} \cdot \sum_{q=0}^{N_s-1} \int_{\mathbb{R}} |h^{\rightarrow}(t - qT_s)|^2 dt \\
&\stackrel{\substack{\text{Time-shift} \\ \text{invariance}}}{=} \int_{\mathbb{R}} |h^{\rightarrow}(t)|^2 dt, \quad \forall N_s.
\end{aligned} \tag{2.2.12}$$

This implies that the mean input power per symbol corresponds exactly to the energy of the pre-HPA filter. This quantity is basically composed of all the gains and losses between the modulator output and HPA input. It is a tunable parameter thanks to the gain control element placed before the HPA. This element allows the link to be operated in either fixed gain mode where the pre-HPA satellite gain can be adjusted via ground control, or automatic level control (ALC) mode. In ALC mode, variations of power occurring between the modulator output and HPA input, such as the ones caused by rain fading, can be automatically compensated for by adjustment of the pre-HPA satellite gain. This results in a fixed  $\bar{P}_{\text{HP}}^{\text{in}}$ . Without loss of generality, the ALC mode is assumed.

Finally, the first coefficients of the HPA polynomial model<sup>23</sup>, based on the mean power per symbol  $\bar{P}_{\text{HP}}^{\text{in}}$  approximation, can be expressed as follows:

$$\gamma_1(\bar{P}_{\text{HP}}^{\text{in}}) = \frac{\alpha_r(1 + 2\beta_r\bar{P}_{\text{HP}}^{\text{in}})}{(1 + \beta_r\bar{P}_{\text{HP}}^{\text{in}})^2}, \tag{2.2.13a}$$

$$\gamma_3(\bar{P}_{\text{HP}}^{\text{in}}) = -\frac{\alpha_r\beta_r}{(1 + \beta_r\bar{P}_{\text{HP}}^{\text{in}})^2} + j \cdot \frac{\alpha_i}{(1 + \beta_i\bar{P}_{\text{HP}}^{\text{in}})^2}. \tag{2.2.13b}$$

These coefficients are directly involved in the CIR calculations of the next chapter. In this context, the impact of the HPA on a multi-carrier signal will also be exposed.

<sup>23</sup>When a carrier is modulated by a sinewave, additional factors are present per order of nonlinearity [19]. However, these correction factors are ignored here to provide clearer derivations and since it does not impact the generality of the results as considered in the state-of-the-art papers [80, 103].

### 2.2.4 Oscillators

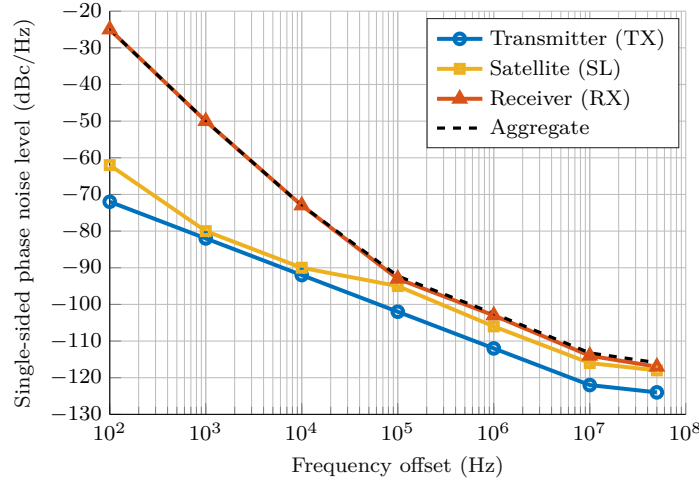


Figure 2-14: Typical Ka-band LOs characteristics

In practical systems, the oscillator noise is recognized as being one of the main limiting performance factors for higher order modulations (16-APSK and above for low roll-off factors) in typical satellite standards [52]. More precisely, the phase of the oscillator noise (dominant component) is defined as the difference between the phase of the carrier and the phase of the LO. The LOs frequency and phase instabilities are often the most critical sources of oscillator noise in satellite systems. On the one hand, the satellite LO is more critical in non-DTH services. On the other hand, the user terminal LNB LO is more critical in DTH services [52] as illustrated in Fig. 2-14. On this graph, typical Ka-band phase noise masks are depicted for DTH services as presented in the DVB-S2X standard. It can be observed that, when taking the aggregate<sup>24</sup> phase noise mask of the system, the mask of the user receiver terminal outweighs the other masks.

By design, the oscillator noise is a multiplicative impairment due to the frequency mixer operation. Two main models of oscillator noise are available in the literature [68, 104, 105]. The first one models an oscillator controlled by a phase-locked loop and approximates the oscillator noise process as a zero-mean colored Gaussian process that is wide-sense stationary (WSS) and has a finite variance. The second one models a free-running oscillator and assumes the oscillator noise process to be a Wiener process that is nonstationary and has a variance growing with time. In the context of this thesis, i.e. high-rate satellite communications, the oscillator noise process is typically assumed to be of the first type [52, 106]. It is worth noting that in the context of low-rate satellite communications, such as narrowband Internet of Things, the phase noise process must be modeled as the second type [107].

For each LO, the oscillator phase noise modeling goes as follows. As a first step, a real zero-mean unit-power white Gaussian process is considered and denoted by  $\Phi_{(\cdot)}(t)$ . In other words,  $\mathbb{E}[\Phi_{(\cdot)}(t)] = 0$  and  $\mathbb{V}[\Phi_{(\cdot)}(t)] = 1, \forall t$ . A phase

<sup>24</sup>The notion of aggregation is developed in more detail in the next chapter.

noise mask filter with transfer function  $H_{(\cdot)}^{\Phi}(f)$  is defined to shape the desired phase noise profile in frequency domain. In time domain, the resulting phase noise<sup>25</sup> is  $\Theta_{(\cdot)}(t) = \text{mod}((\Phi_{(\cdot)} * h_{(\cdot)}^{\Phi})(t), 2\pi)$ , where  $h_{(\cdot)}^{\Phi}(t)$  is the phase noise mask filter impulse response. Thus, the phase noise perturbation  $e^{j\Theta_{(\cdot)}(t)}$  follows a wrapped colored Gaussian distribution. An example of integration of receiver LO phase noise is illustrated in Fig. 2-15. In this context, the transmitter, satellite, and receiver phase noise mask impulse responses are denoted by  $h_{\text{TX}}^{\Phi}(t)$ ,  $h_{\text{SL}}^{\Phi}(t)$  and  $h_{\text{RX}}^{\Phi}(t)$ , respectively. At the mask output, the shaped phase noises of the transmitter, satellite, and receiver are denoted by  $\Theta_{\text{TX}}(t)$ ,  $\Theta_{\text{SL}}(t)$ , and  $\Theta_{\text{RX}}(t)$ , respectively.

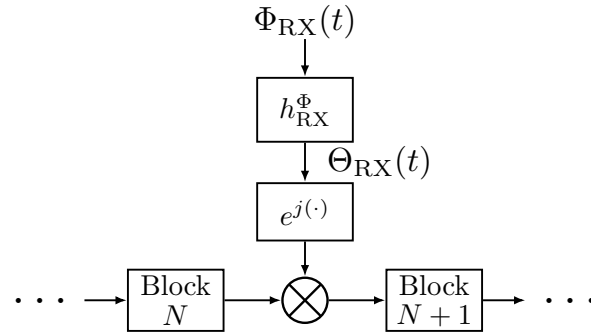


Figure 2-15: Integration of receiver LO phase noise between two system blocks

<sup>25</sup>The modulo operation is required for the disambiguation of the angle and thus, the study of the wrapped distribution.



# 3 | Mathematical Characterization

## Contents

<b>3.1</b>	<b>Waveform imperfections . . . . .</b>	<b>39</b>
<b>3.2</b>	<b>Filter distortions . . . . .</b>	<b>41</b>
<b>3.3</b>	<b>Amplifier distortions . . . . .</b>	<b>52</b>
<b>3.4</b>	<b>Oscillator noise . . . . .</b>	<b>63</b>
<b>3.5</b>	<b>Summary and future works . . . . .</b>	<b>69</b>

Based on the prerequisites, the core contributions of this work can be introduced. As such, this chapter is dedicated to the mathematical characterization of the critical impairments: Waveform imperfections, filter distortions, amplifier distortions, and oscillator noise. To define the key parameters and reveal their fundamental behavior, each impairment is analyzed separately from one another. *Novel* CIR formulas are derived for each impairment, ranging from more general expressions down to more practical asymptotic formulas. The interested reader can refer to the indicated complementary information for non-trivial calculation steps. In particular, lists of useful definitions, identities, and proofs are available in Appendices A, B, and C, respectively.

## 3.1 Waveform imperfections

To analyze the waveform imperfections, the LTI system in Fig. 2-10 is considered with channel  $h_{\text{CH}}(t) = \beta \cdot \delta(t)$ . Based on the generic CIR formula in LTI system (2.2.9) and the sampled time-limited SC expression  $h_{\text{SC}}^{\approx}(t, \alpha, T_s, ST_s, F_s)$  of (2.2.6), the CIR specific to waveform imperfections can be derived. Thus, the *novel* formula taking into account time finiteness and aliasing is defined below.

### Formula 1: Waveform imperfections

$$\left(\frac{C}{I}\right)_{\text{WI}}^{\star}(\alpha, S, N_{\text{S}/s}) = \frac{\left| \frac{1}{N_{\text{S}/s}} \sum_{m=-S \cdot N_{\text{S}/s}+1}^{S \cdot N_{\text{S}/s}} h_{\text{SC}}\left(\frac{m}{N_{\text{S}/s}}, \alpha\right) \right|^2}{2 \cdot \sum_{k=1}^{2S-1} \left| \frac{1}{N_{\text{S}/s}} \sum_{m=(k-S) \cdot N_{\text{S}/s}+1}^{S \cdot N_{\text{S}/s}} h_{\text{SC}}\left(\frac{m}{N_{\text{S}/s}}, \alpha\right) h_{\text{SC}}\left(k - \frac{m}{N_{\text{S}/s}}, \alpha\right) \right|^2}$$

In this expression, the key parameters impacting the CIR are the roll-off  $\alpha$ , the one-sided SC span  $S$  and the number of samples per symbol  $N_{S/s}$ . Interestingly, the convolution of imperfect pulse shaping and detection filters gives rise to a Riemann sum<sup>1</sup>. Using Riemann identity in Appendix B.3.2, the following property follows:

$$\left(\frac{C}{I}\right)_{\text{WI}}^*(\alpha, S, N_{S/s}) \rightarrow \left(\frac{C}{I}\right)_{\text{WI}}^*(\alpha, S), \text{ as } N_{S/s} \rightarrow +\infty, \quad (3.1.1)$$

where the CIR related to time finiteness is:

$$\left(\frac{C}{I}\right)_{\text{WI}}^*(\alpha, S) = \frac{\left|\int_{-S}^S h_{\text{SC}}(u, \alpha)^2 du\right|^2}{2 \cdot \sum_{k=1}^{2S-1} \left|\int_{k-S}^S h_{\text{SC}}(u, \alpha) h_{\text{SC}}(k-u, \alpha) du\right|^2}. \quad (3.1.2)$$

In other words, the time finiteness impairment is already contained in Formula 1. Choosing to work in analog or digital domain simply depends on the value of  $N_{S/s}$  to consider. Furthermore, this CIR converges as expected towards the Nyquist CIR (2.2.5) when the span becomes infinite, i.e.:

$$\left(\frac{C}{I}\right)_{\text{WI}}^*(\alpha, S) \rightarrow \left(\frac{C}{I}\right)_{\text{WI}}^*(\alpha) \rightarrow +\infty, \text{ as } S \rightarrow +\infty. \quad (3.1.3)$$

Moreover, Fig. 3-1 illustrates the fundamental behavior Formula 1 as a function of the key parameters. Theoretical results are validated through numerical simulations.

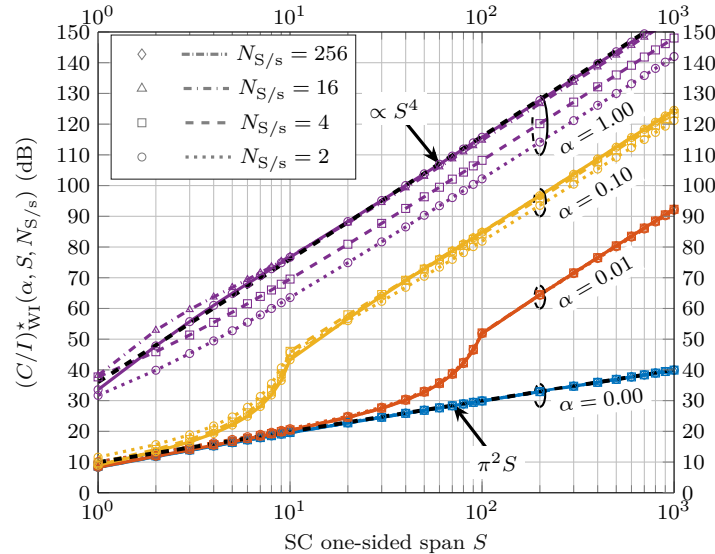


Figure 3-1: Waveform imperfections CIR

<sup>1</sup>To be rigorous, one point needs to be removed to obtain a Riemann sum. Here, arbitrarily  $m = (k-S) \cdot N_{S/s}$  can be removed to create a right Riemann sum (even though this point disappears when  $N_{S/s} \rightarrow +\infty$ ).

In this chapter, markers and lines represent numerical and theoretical results, respectively.

Firstly, the CIR is increasing with increasing  $\alpha$ , since a higher  $\alpha$  smoothens the frequency characteristic and progressively removes the Gibbs phenomenon. In fact, the impact of  $\alpha$  can be quite significant depending on  $S$ . For a given  $\alpha$ , the CIR makes the transition between a trend  $\propto S$  and a trend  $\propto S^4$ . To give further insight, the CIR asymptote for  $\alpha = 0$  can be computed as:

$$\left(\frac{C}{I}\right)_{\text{WI}}^*(0, S, N_{S/s}) \rightarrow \pi^2 S, \quad \text{as } (S, N_{S/s}) \rightarrow (+\infty, +\infty). \quad (3.1.4)$$

The corresponding proof can be found in Appendix C.2.1. It relies interestingly on another form of Riemann sum. On another side, the impact of  $N_{S/s}$  is rather weak for low roll-offs. For instance, the asymptote formula (3.1.4) has a minimum accuracy of 98.4 % for  $N_{S/s} \in \{2; 4\}$ ,  $S \geq 10$  and  $\alpha = 0$ . It can be interpreted in the sense that the Riemann sums involved have a fast convergence with increasing  $N_{S/s}$ . In fact,  $\pi^2 S$  can be considered as the CIR lowerbound of waveform imperfections.

In practical systems,  $\alpha$  is less flexible than  $N_{S/s}$  and  $S$ . Therefore, these latter parameters should be chosen wisely in order to minimize the system load and complexity. Thus, the analysis suggests that the number of samples per symbol can be reduced down to  $N_{S/s} = 2$  with most likely little added impairments. Furthermore, it is of interest to aim at the trend  $\propto S^4$  when selecting the SC span.

#### Main findings on waveform imperfections

To finalize this section, we can draw the following conclusions:

- Formula 1 provides an important insight into the waveform imperfections CIR that can be expected in more complex systems.
- Based on Fig. 3-1, the  $N_{S/s}$  and  $S$  can be chosen such as to balance maximization of the CIR and minimization of the system load and complexity.

## 3.2 Filter distortions

### 3.2.1 General considerations

To analyze the filter distortions, the LTI system in Fig. 2-10 is considered. The system especially contains the channel transfer function  $H_{\text{CH}}(f)$  characterizing the filter distortions, which are yet to be defined. For this study, waveform imperfections are neglected in the calculations<sup>2</sup>, i.e.  $(S, N_{S/s}) \rightarrow (+\infty, +\infty)$ . The carrier placement is denoted by  $f_{\Delta}$  and defined, by convention, with respect to the center of the channel characteristic. For more convenient calculations, the expression of the system impulse

<sup>2</sup>In numerical simulations,  $N_{S/s}$  and  $S$  are selected sufficiently high based on Fig. 3-1 such as to isolate the impairment under study.

response can be reformulated using the successive variables changes:  $f' = f - f_\Delta$  and  $\tilde{f} = f' \cdot T_s$ . Thus, the system impulse response defined as optimal decision instant can be expressed as:

$$h(\tau^* T_s) = \mathcal{F}^{-1} \left[ H_{RC}(\tilde{f}, \alpha) \cdot H_{CH}((\tilde{f} + \tilde{f}_\Delta)/T_s) \right] (\tau^*) , \quad (3.2.1)$$

where the normalized carrier placement is  $\tilde{f}_\Delta = f_\Delta \cdot T_s$ . Based on the generic CIR formula in LTI system (2.2.9), the CIR can be expressed in frequency domain representation and  $T_s$ -normalized as defined below.

#### Formula 2: Filter distortions

$$\left( \frac{C}{I} \right)_{\text{FD}}^* (\alpha, T_s, \tilde{f}_\Delta) = \frac{\left| \int_{\mathbb{R}} H_{RC}(\tilde{f}, \alpha) \cdot H_{CH}((\tilde{f} + \tilde{f}_\Delta)/T_s) \cdot e^{j2\pi \tilde{f} \tau^*} d\tilde{f} \right|^2}{\sum_{k \in \mathbb{Z}^*} \left| \int_{\mathbb{R}} H_{RC}(\tilde{f}, \alpha) \cdot H_{CH}((\tilde{f} + \tilde{f}_\Delta)/T_s) \cdot e^{j2\pi \tilde{f} (\tau^* + k)} d\tilde{f} \right|^2}$$

Indeed, due to the property of multiplying the transfer functions, it is more convenient to compute the CIR based on the frequency domain (as opposed to the waveform imperfections). This generic formula is in fact equivalent to Jones' formula [78] in the case  $\alpha = 0$ . The novelty comes from the inclusion of the SC as well as the determination of the CIR given a specific practical representation of  $H_{CH}(f)$ . As such, two representations are explored in the following: the exponential polynomial representation (Section 3.2.2) and the pole-zero representation (Section 3.2.3).

In this context of filter distortions<sup>3</sup>, one important point is the determination of the decision instant offset  $\tau$ , which maximizes the CIR. Indeed, this parameter can have a large impact on the value of the CIR depending on the considered scenario. In particular, its value can be determined from the expression of the CIR as follows:

$$\frac{\partial \left( \frac{C}{I} \right)_{\text{FD}} (\alpha, T_s, \tilde{f}_\Delta, \tau^*)}{\partial \tau} = 0 , \quad \frac{\partial^2 \left( \frac{C}{I} \right)_{\text{FD}} (\alpha, T_s, \tilde{f}_\Delta, \tau^*)}{\partial \tau^2} > 0 , \quad (3.2.2)$$

which may be challenging to obtain depending on how complex the channel is.

### 3.2.2 Exponential polynomial representation

#### Motivation

The idea behind the exponential polynomial representation is to express the gain and group delay in terms of frequency polynomials of degree  $N_{\text{FD}}$  as follows:

$$G_{\text{dB}}(f) = g_{N_{\text{FD}}} f^{N_{\text{FD}}} + \dots + g_2 f^2 + g_1 f + g_0 , \quad (3.2.3a)$$

$$D(f) = d_{N_{\text{FD}}} f^{N_{\text{FD}}} + \dots + d_2 f^2 + d_1 f + d_0 , \quad (3.2.3b)$$

<sup>3</sup>In the context of waveform imperfections, the optimal decision instant offset is implicitly  $\tau^* = 0$ .



where  $\{g_k\}_{0 \leq k \leq N_{\text{FD}}}$  and  $\{d_k\}_{0 \leq k \leq N_{\text{FD}}}$  are the gain and group delay coefficients, respectively. Assuming that the frequency is expressed in the conventional (MHz) unit, the coefficients are expressed in (dB/MHz<sup>k</sup>) and ( $\mu\text{s}/\text{MHz}^k$ ),  $0 \leq k \leq N_{\text{FD}}$ , respectively. In this work, both polynomials correspond to the so-called  $N_{\text{FD}}^{\text{th}}$ -order of filter distortions. The interested reader can refer to [J1] for more details on the least-squares (LS) approximation of the filter distortions, which leads to the gain and group delay coefficients. For further insight, the properties of the polynomials are presented in increasing order.

### Order $N_{\text{FD}} = 0$

Starting with the 0<sup>th</sup>-order of filter distortions, the gain, group delay, and corresponding channel transfer function can be expressed as:

$$G_{\text{dB}}(f) = g_0 , \quad (3.2.4a)$$

$$D(f) = d_0 , \quad (3.2.4b)$$

$$H_{\text{CH}}(f + f_{\Delta}, g_0, d_0, \varphi_0) = e^{\xi g_0 - j2\pi(d_0(f + f_{\Delta}) + \varphi_0)} , \quad (3.2.4c)$$

where  $\varphi_0$  is the phase offset coming from the integration of the group delay expressed in (rad). Thanks to the Fourier transform scaling property and time-shifting property (Appendices B.5.(1) and B.5.(2)), constant gain and group delay in frequency domain leads to the following effect in time domain:

$$h_{\text{RC}}(t - d_0, \alpha) \cdot e^{\xi g_0 - j2\pi(d_0 f_{\Delta} + \varphi_0)} \xleftrightarrow[\mathcal{F}^{-1}[\cdot]]{\mathcal{F}[\cdot]} H_{\text{RC}}(f, \alpha) \cdot H_{\text{CH}}(f + f_{\Delta}, g_0, d_0, \varphi_0) . \quad (3.2.5)$$

Furthermore, due to the scaling and time-shifting invariance of Formula 2, the filter distortions CIR is infinite and the system is free of filter distortions<sup>4</sup>.

### Order $N_{\text{FD}} = 1$

Continuing with the 1<sup>st</sup>-order of filter distortions, the gain, group delay, and corresponding channel transfer function can be expressed as:

$$G_{\text{dB}}(f) = g_1 f , \quad (3.2.6a)$$

$$D(f) = d_1 f , \quad (3.2.6b)$$

$$H_{\text{CH}}(f, g_1, d_1) = e^{\xi g_1 f - j\pi d_1 f^2} , \quad (3.2.6c)$$

once all the terms not source of filter distortions can be removed, i.e.,  $g_0 = 0$ ,  $d_0 = 0$ ,  $\varphi_0 = 0$  and  $f_{\Delta} = 0$ . It is worth noting that by definition the group delay slope  $d_1$  is a dimensionless quantity. However, when reasoning with frequencies in (MHz), it can be interpreted as ( $\mu\text{s}/\text{MHz}$ ) and requires a conversion factor of  $10^3$  when (ns/MHz) is considered. An example of LS fitting is illustrated in Fig. 3-2. In this scenario, the

<sup>4</sup>In that case, the system becomes limited by other impairments such as the waveform imperfections. Thus, another CIR formula must be used to characterize the system.

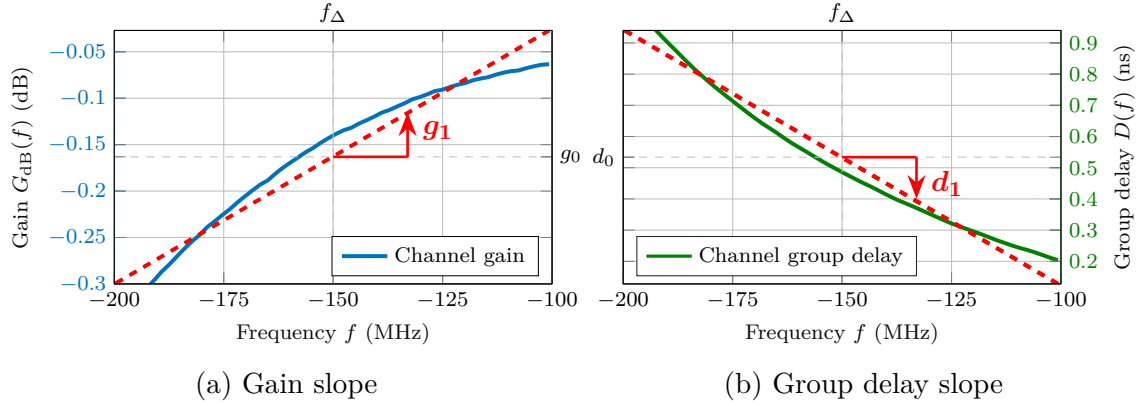


Figure 3-2: Example of slope fitting.

approximated channel corresponds to the wideband OMUX characteristics presented in Fig. 2-11. The LS fitting is performed over a carrier bandwidth  $B = 100$  MHz placed at frequency  $f_{\Delta} = -150$  MHz. It results in a gain slope of  $g_1 = +2.75 \cdot 10^{-3}$  dB/MHz and a group delay slope of  $d_1 = -8.21 \cdot 10^{-3}$  ns/MHz.

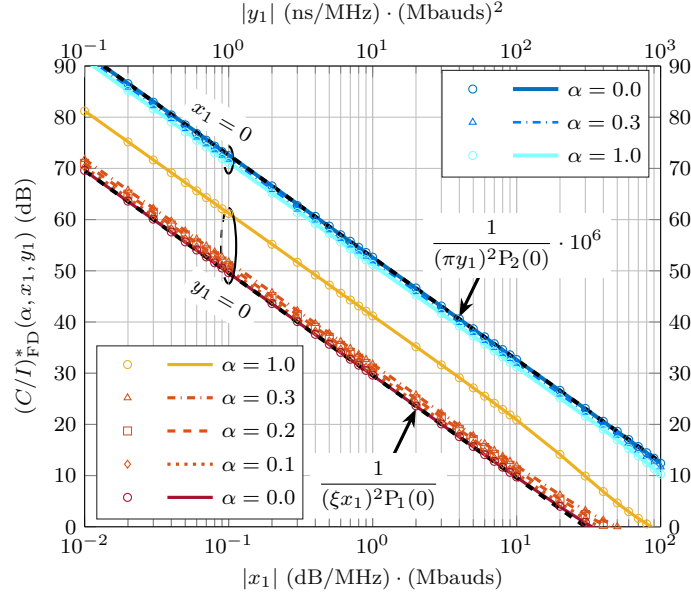
To compute the CIR formula corresponding to the 1<sup>st</sup>-order of filter distortions, it is convenient to reformulate the  $T_s$ -normalized channel transfer function as follows:

$$H_{CH}(\tilde{f}/T_s, g_1, d_1) = H_{CH}(\tilde{f}, x_1, y_1) = e^{\xi x_1 \tilde{f} - j\pi y_1 \tilde{f}^2}, \quad (3.2.7)$$

where  $x_1 = g_1 \cdot R_s$  and  $y_1 = d_1 \cdot R_s^2$  are in this work called the 1<sup>st</sup>-order gain and group delay distortions coefficients. They are expressed in (dB/MHz) · (Mbauds) and ( $\mu$ s/MHz) · (Mbauds)<sup>2</sup>, respectively. With this reformulation, the 1<sup>st</sup>-order filter distortions can be fully characterized by three parameters: The roll-off  $\alpha$ , the 1<sup>st</sup>-order gain distortions coefficient  $x_1$  and 1<sup>st</sup>-order group delay distortions coefficient  $y_1$ . Fig. 3-3 illustrates the fundamental CIR behavior with respect to the gain and group delay distortions. It is reminded that markers and lines represent numerical and theoretical results, respectively.

*Analysis of the distortions coefficients:* Firstly, the CIR is strictly decreasing both with increasing  $|x_1|$  and  $|y_1|$ . This has two implications. On the one hand, given a fixed symbol rate, increasing either the gain slope or group delay slope decreases the CIR. On the other hand, given fixed gain and group delay slopes, increasing the symbol rate also decreases the CIR. Secondly, the impact of the roll-off is more significant with the gain distortions than with the group delay distortions. In fact, to further reveal the behavior of the CIR, a *novel* asymptote formula has been computed and is provided next<sup>5</sup>.

<sup>5</sup>This formula belongs to one of the major discoveries of this thesis.

Figure 3-3: Filter distortions CIR ( $N_{\text{FD}} = 1$ )**Formula 3: Filter distortions asymptote ( $N_{\text{FD}} = 1$ )**

$$\left(\frac{C}{I}\right)_{\text{FD}}^*(\alpha, x_1, y_1) \rightarrow \frac{1}{(\xi x_1)^2 P_1(\alpha) + (\pi y_1)^2 P_2(\alpha)}, \quad \text{as } (x_1, y_1) \rightarrow (0, 0)$$

More details on the derivation of the asymptote is provided in Appendix C.3.1. Furthermore, the exact expressions of the so-called roll-off polynomials  $P_1(\alpha)$  and  $P_2(\alpha)$  are presented in Appendix B.1.3. Although their primary formulation is a series function of  $\alpha$ , they actually come down to polynomials. Values of interest for these polynomials are provided in Table 3.1. Furthermore, this asymptote leads to multiple properties:

- 1) The CIR is even with respect to the gain slope  $g_1$  and group delay slope  $d_1$ .
- 2) The impact of the roll-off  $\alpha$  and symbol rate  $R_s$  on the CIR can be considered independent of each other, when considering fixed gain slope  $g_1$  and group delay slope  $d_1$ . Under this condition, they can be optimized separately.

Table 3.1: Roll-off polynomials values of interest (rounded to the 5th decimals).

$\alpha$	0.00	0.05	0.10	0.15	0.20	0.25	0.30
$P_1(\alpha)$	0.08333	0.07720	0.07131	0.06565	0.06023	0.05504	0.05010
$P_2(\alpha)$	0.00556	0.00559	0.00570	0.00586	0.00606	0.00630	0.00656

- 3) The CIR can be decomposed into a gain slope CIR, and a group delay slope CIR, where each ratio corresponds to an impairment independent of the other. In other words, the CIR behaves according to the decomposition rule that can be expressed as follows:

$$\left(\frac{C}{I}\right)_{\text{FD}}^{\star-1}(\alpha, x_1, y_1) \rightarrow \left(\frac{C}{I}\right)_{\text{FD}}^{\star-1}(\alpha, x_1, 0) + \left(\frac{C}{I}\right)_{\text{FD}}^{\star-1}(\alpha, 0, y_1), \text{ as } (x_1, y_1) \rightarrow (0, 0). \quad (3.2.8)$$

*Analysis of the roll-off:* To further expand on the impact of the roll-off on the CIR, roll-off polynomials of orders 1 to 3 are depicted in Fig. 3-4. Indeed, each polynomial arises from a specific frequency behavior:  $P_1(\alpha)$  corresponds to a linear frequency  $f$  behavior like in the case of a gain slope,  $P_2(\alpha)$  corresponds to a parabolic frequency  $f^2$  behavior like in the case of a group delay slope (meaning parabolic phase) as well as in the case of a parabolic gain, etc. The main point is that there is no specific range of  $\alpha$  that improves the CIR. On the one hand, if  $x_1$  is dominant, then aiming toward higher roll-off may largely improve the CIR based on  $P_1(\alpha)$  characteristic. On the other hand, if  $y_1$  is dominant, then aiming toward lower roll-off improves slightly the CIR based on  $P_2(\alpha)$  characteristic. Thus, a trade-off needs always to be considered<sup>6</sup>. Finally, different values of the partial sum limit  $L$  are depicted to emphasize the influence of filter memory. In this context, it can especially be observed that  $P_1(\alpha)$  requires more memory for low roll-off values (in the order of  $L = 10$ ), whereas  $P_2(\alpha)$  has a relatively fast convergence (in the order of  $L = 2$ ).

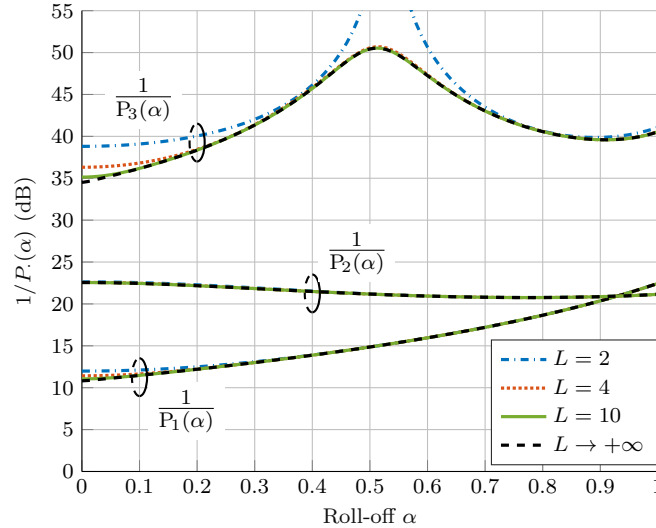
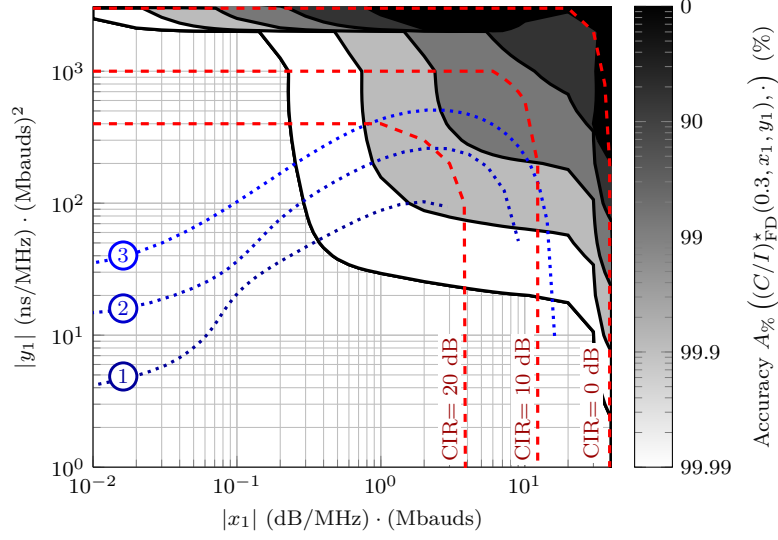


Figure 3-4: Roll-off polynomials.

*Analysis of the asymptote accuracy:* Besides the analysis of the roll-off, the accuracy of Formula 3 is given as a grayscale in Fig. 3-5. On this graph, lighter colors correspond to higher levels of accuracy. It is considered that beyond the last contour corresponding to an accuracy of 99.99 %, the area is free of approximation error.

<sup>6</sup>It is worth noting that in the case of higher order filter distortions and bandlimited carriers, the best roll-offs are often lower due to the impact of the bandlimitation.

Figure 3-5: Accuracy of Formula 3 ( $\alpha = 0.3$ ).

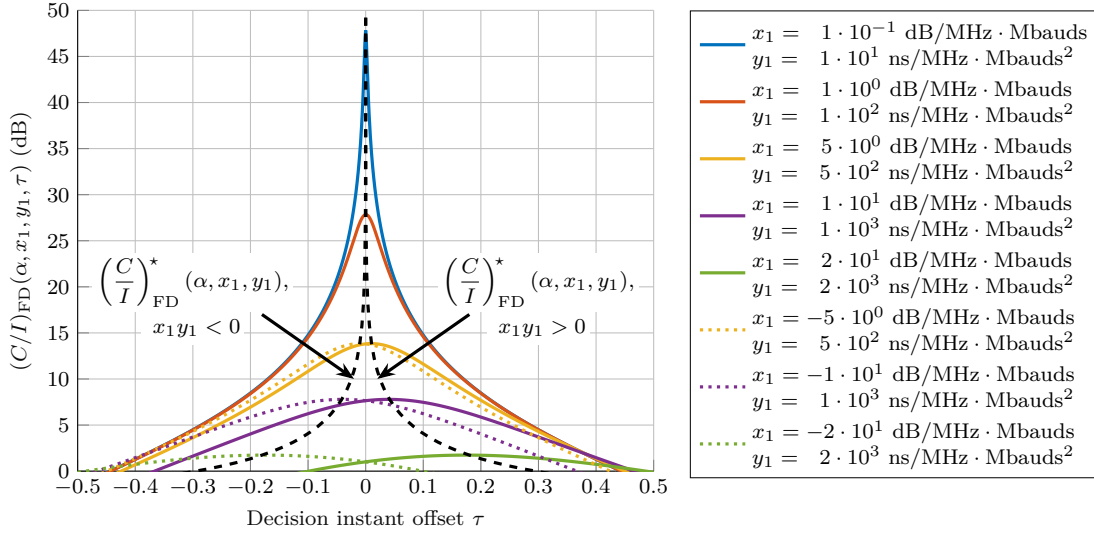
Since the most common roll-offs  $\alpha$  belong to the interval  $[0, 0.3]$ , the upperbound  $\alpha = 0.3$  is considered as a representative value. It is observed that for any CIR above 20 dB (red dashed line), Formula 3 leads in the worst-case scenario to an accuracy of about 99.5 %, which corresponds to a maximum approximation error of only 0.1 dB. Furthermore, this boundary is further extended for lower  $\alpha$ : For  $\alpha = 0.2$ , a maximum approximation error of 0.1 dB holds for any CIR above 13 dB, whereas for  $\alpha = 0.1$ , it corresponds to any CIR above 4 dB. On top of that, the accuracy of Formula 3 is also improved when  $|x_1|$  or  $|y_1|$  is more dominant than the other.

To highlight what can be expected in practice, typical  $(|x_1|, |y_1|)$  ranges are illustrated in dashed blue lines. In this scenario, the approximated channel is based again on the wideband OMUX characteristics presented in Fig. 2-11. Within this channel, three carriers are considered with the corresponding bandwidth ratios<sup>7</sup>  $R_s/B_N \in \{0.1, 0.2, 0.4\}$  that are indicated by the circled numbers 1, 2, 3, respectively. The  $(|x_1|, |y_1|)$  ranges correspond to the ranges of gain and group delay slopes from the center of the channel until the edges of the channel. It can be observed that for small carriers with respect to the channel bandwidth, Formula 3 can be applied with high accuracy. Typically, with  $R_s/B_N \leq 0.1$ , the CIR approximation error is less than 0.04 dB. However, with  $R_s/B_N \geq 0.2$  and a carrier placed at the edge of the channel, the CIR approximation error is at least 0.15 dB. This means that, even though Formula 3 is highly accurate in most cases, its application must still be done with care.

*Analysis of the decision instant offset:* Last but not least, an analysis of the decision instant offset is illustrated in Fig. 3-6. It shows the CIR as a function of  $\tau$  for  $\alpha = 0$  given a set of values<sup>8</sup> of  $(x_1, y_1)$ . A drift of the optimal decision instant

<sup>7</sup>The bandwidth ratio is introduced to express generally the carrier bandwidth with respect to the nominal bandwidth.

<sup>8</sup>To emphasize a consistent trend of CIR with  $\tau$ , the set of values is chosen such that the gain

Figure 3-6: Decision instant offset optimality ( $\alpha = 0$ ).

offset  $\tau^*$  can immediately be noticed for lower CIRs. This implies that the optimal decision instant offset  $\tau^*$  is not exactly zero, but a function of gain and group delay distortions coefficients  $x_1$  and  $y_1$ . In particular, the CIR corresponding to  $x_1 y_1 < 0$  is simply the reflection over the  $y$ -axis of the CIR corresponding to  $x_1 y_1 > 0$ . Therefore, the maximum value is conserved and the study of the CIR can be reduced to  $|x_1|$  and  $|y_1|$  (beyond the scope of Formula 3). In fact, it is only when the filter distortions are severe that the approximation  $\tau^* \rightarrow 0$  as  $(x_1, y_1) \rightarrow (0, 0)$  used in the derivations of Formula 3 is no longer valid. Typically, this happens for CIR less than 10 dB. It is only when the roll-off  $\alpha$  is higher or when  $x_1$  and  $y_1$  are equally dominant (as illustrated here) that the drift happens at slightly higher CIRs. In the end, this result coincides with the decrease of the accuracy of Formula 3 discussed previously and depicted in Fig. 3-5. Indeed, the drift coincides with cross terms becoming more dominant such as  $x_1 y_1$ . In that case, the gain and group delay are no longer orthogonal and the decomposition rule (3.2.8) does not apply anymore.

Paradoxically, the smaller  $|x_1|$  and  $|y_1|$  are, the more sensitive to  $\tau$  is the CIR. Thus, the tracking of the optimal decision instant is a critical matter, since even though there might be a high CIR defined at  $\tau^*$ , an imperfect estimation of the optimal decision instant can already significantly impact the CIR. This phenomenon was numerically observed in [108] in the presence of a non-constant group delay in the satellite communication chain. Finally, it is worth noting that in [J1], it is shown that the CIR can also be computed as the inverse of a polynomial in  $\tau$  using the series listed in Appendix B.1.1.

---

and group delay parameters keep the same dominance relative to each other, i.e.  $|x_1|/|y_1|$  is chosen constant.

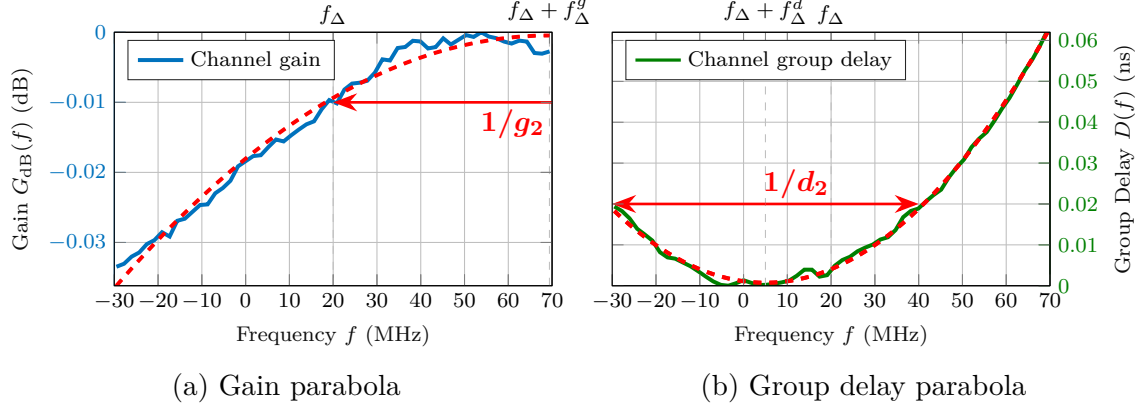


Figure 3-7: Example of parabola fitting.

### Order $N_{\text{FD}} \geq 2$

To give further intuitions about  $N_{\text{FD}} \geq 2$ , the 2<sup>nd</sup>-order of filter distortions are briefly discussed. In this case, the gain and group delay can be expressed as:

$$G_{\text{dB}}(f) = g_2 f^2 + g_1 f + g_0, \quad (3.2.9a)$$

$$D(f) = d_2 f^2 + d_1 f + d_0, \quad (3.2.9b)$$

which can be reformulated more meaningfully as follows:

$$G_{\text{dB}}(f) = g_2 (f + f_{\Delta}^g)^2, \quad (3.2.10a)$$

$$D(f) = d_2 (f + f_{\Delta}^d)^2, \quad (3.2.10b)$$

where  $f_{\Delta}^g$  and  $f_{\Delta}^d$  represent the frequency offset with respect to the carrier center frequency of the parabola vertex<sup>9</sup> of the gain and group delay, respectively. An example of LS fitting is illustrated in Fig. 3-7 based on the same wideband OMUX characteristics. The LS fitting is performed over a carrier bandwidth  $B = 100$  MHz placed at frequency  $f_{\Delta} = +20$  MHz. It results in an inverse gain parabola latus rectum of  $g_2 = -3.65 \cdot 10^{-6}$  dB/MHz<sup>2</sup>, an inverse group delay parabola latus rectum of  $d_2 = +1.47 \cdot 10^{-5}$  ns/MHz<sup>2</sup>, a gain parabola vertex frequency offset of  $f_{\Delta}^g = +49.4$  MHz and a group delay parabola vertex frequency offset of  $f_{\Delta}^d = -15.0$  MHz.

Similarly to the 1<sup>st</sup>-order of filter distortions, the  $T_s$ -normalized channel transfer function can be expressed as:

$$H_{\text{CH}}(\tilde{f} + \tilde{f}_{\Delta}, x_2, y_2, \tilde{f}_{\Delta}^g, \tilde{f}_{\Delta}^d) = e^{\xi x_2 (\tilde{f} + \tilde{f}_{\Delta} + \tilde{f}_{\Delta}^g)^2 - j \frac{2\pi}{3} y_2 (\tilde{f} + \tilde{f}_{\Delta} + \tilde{f}_{\Delta}^d)^3}, \quad (3.2.11)$$

where  $x_2 = g_2 \cdot R_s^2$  and  $y_2 = d_2 \cdot R_s^3$  are the 2<sup>nd</sup>-order gain and group delay distortions coefficients. They are expressed in (dB/MHz<sup>2</sup>) · (Mbauds)<sup>2</sup> and (μs/MHz<sup>2</sup>) · (Mbauds)<sup>3</sup>, respectively. Lastly, the frequency offsets corresponding to the vertexes

<sup>9</sup>This equivalence can be established by setting  $f_{\Delta}^g = g_1/(2g_2)$ ,  $f_{\Delta}^d = d_1/(2d_2)$ , and removing the terms that are not source of filter distortions.

are also expressed with regard to the symbol period as  $\tilde{f}_\Delta^g = f_\Delta^g \cdot T_s$  and  $\tilde{f}_\Delta^d = f_\Delta^d \cdot T_s$ .

A more detailed investigation of the 2<sup>nd</sup>-order of filter distortions has been carried out in [J1], which led to several conclusions. Firstly, using the order  $N_{\text{FD}} = 2$  is only useful to take into consideration cases where the 1<sup>st</sup>-order of filter distortions leads to large CIR approximation errors. This typically occurs around gain and group delay ripples, which can be caused by practical design imperfections. Such ripples are depicted in the example of Fig. 3-7. Indeed, approximating a gain ripple (respectively group delay ripple) by a slope can lead to a nearly flat gain (respectively flat group delay), which potentially causes a high CIR approximation error. These exact cases are covered by the 2<sup>nd</sup>-order of filter distortions. However, it is shown in [J1] that the characterization of ripple is very localized. Moreover, it may not be necessary in practice since it corresponds to ranges of gain and group delay with some of the highest CIRs where the filter distortions are most likely dominated by another impairment. Lastly, the 2<sup>nd</sup>-order of filter distortions cannot be used to characterize more than one localized ripple, which typically happens when elliptical satellite filters are implemented. Thus, a higher order  $N_{\text{FD}} \geq 2$  must be considered. Nevertheless, there does not appear to be an advantage in reducing the actual order of the channel due to the rapid increase in complexity of the CIR expressions. Therefore, another representation characterizing the exact order of filter distortions is introduced in the following.

### 3.2.3 Pole-zero representation

In practice, IMUX and OMUX filters are characterized by their number of poles (constraining the passband ripple), transmission zeros (constraining the stopband attenuation), and possible additional zeros (flattening the group delay). Since they are the major source of filter distortions it is reasonable to express a model given the poles and zeros. In practice, the linear distortions transfer function related to the complete system will be closely related to the one of the IMUX and OMUX filters with additional perturbations. Based on this representation, the channel transfer function can be defined as:

$$H_{\text{CH}}(f + f_\Delta, f_c) = \frac{\prod_{i=0}^{N_z-1} ((f + f_\Delta) - f_c \cdot z_i)}{\prod_{i=0}^{N_p-1} ((f + f_\Delta) - f_c \cdot p_i)}, \quad (3.2.12)$$

where  $\{z_i\}_{0 \leq i \leq N_z-1}$  and  $\{p_i\}_{0 \leq i \leq N_p-1}$  are the zeros and poles, respectively. It can be defined with respect to a reference frequency such as the one-sided cutoff frequency<sup>10</sup>  $f_c$ . From this expression, the  $T_s$ -normalized channel transfer function can be reformulated as:

$$H_{\text{CH}}(\tilde{f} + \tilde{f}_\Delta, \varrho) = \frac{\prod_{i=0}^{N_z-1} ((\tilde{f} + \tilde{f}_\Delta) - \tilde{z}_i)}{\prod_{i=0}^{N_p-1} ((\tilde{f} + \tilde{f}_\Delta) - \tilde{p}_i)}, \quad (3.2.13)$$

---

<sup>10</sup>By default, it is better to use this reference frequency rather than nominal bandwidth  $B_N$ . Indeed, it has an agreed-upon definition, whereas the nominal bandwidth remains system-dependent.



where  $\{\tilde{z}_i\}_{0 \leq i \leq N_Z-1}$  and  $\{\tilde{p}_i\}_{0 \leq i \leq N_P-1}$  are the normalized zeros and poles, respectively. They are defined as  $\tilde{z}_i = z_i/\varrho$  and  $\tilde{p}_i = p_i/\varrho$ , where the parameter  $\varrho = R_s/f_c$  is the main driver in the filter distortions behavior. This parameter is in fact a dimensionless quantity, but to make the connection with the previously defined exponential polynomial representation, the unit can also be interpreted as (Mbauds/MHz). Indeed, the powers  $\varrho$ ,  $\varrho^2$ ,  $\varrho^3$ , etc. are directly connected to the parameters  $x_1$ ,  $y_1$ ,  $x_2$ ,  $y_2$ , etc.

### Example

For the sake of illustration, the ideal Chebyshev type II filter given in Fig. 2-11 is considered. The zeros and poles of a Chebyshev type II filter are typically of the following form:

$$z_i = \kappa_1 \cdot \frac{1}{\cos(\kappa_2)} , \quad (3.2.14a)$$

$$p_i = \kappa_1 \cdot \frac{\cos(\kappa_2) \cosh(\kappa_3) + j \sin(\kappa_2) \sinh(\kappa_3)}{\cos(\kappa_2)^2 \cosh(\kappa_3)^2 + \sin(\kappa_2)^2 \sinh(\kappa_3)^2} , \quad (3.2.14b)$$

where  $\kappa_1$ ,  $\kappa_2$ , and  $\kappa_3$  are coefficients dependent on the filter order and stopband ripple  $\varepsilon$ . The stopband ripple can be reformulated as  $\varepsilon = 1/\sqrt{A_s^2 - 1}$  such as to define the filter with regards to the stopband attenuation. In order to have a realistic model,  $A_{s,\text{dB}} = 35.0$  dB is selected, which is above 30.0 dB as recommended by the DVB-S2x standard [52] and ensuring a characteristic close to the OMUX model.

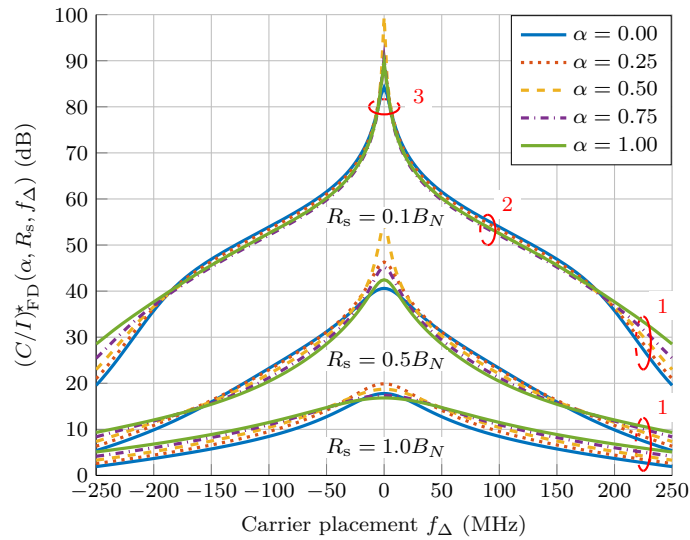


Figure 3-8: Chebyshev type II filter distortions CIR

The corresponding CIR can be computed by plugging 3.2.13 into Formula 2. It is illustrated in Fig. 3-8 as a function of the carrier placement. By showing the characteristic for various roll-offs, it is possible to identify specific filter distortions behaviors described in the exponential polynomial representation. These behaviors

are indicated by the numbers 1, 2, 3, which correspond to a domination of gain slope, group delay slope, and group delay parabola, respectively. They are directly related to the roll-off polynomials  $P_1(\alpha)$ ,  $P_2(\alpha)$ , and  $P_3(\alpha)$  presented in Fig. 3-4. Furthermore, the curves corresponding to  $R_s/B_N \in \{0.1, 0.5, 1\}$  are displayed to highlight the impact of the carrier bandwidth. In particular, the effect of the bandlimitation can be observed around the center of the channel. Indeed, although the optimal roll-off for narrow carriers is  $\alpha = 0.5$  at the peak CIR, the optimal roll-off tends to decrease for wider carriers due to the bandlimitation. Besides that, the optimal roll-off at the edges is  $\alpha = 1$  due to  $P_1(\alpha)$  characteristic related to the gain slope domination. When the carrier is wider, this domination happens with smaller  $f_\Delta$ .

#### Main findings on filter distortions

To finalize this section, we can draw the following conclusions:

- Low-complexity Formula 3 can be used to compute the filter distortions CIR for quasi-linear trends of gain and group delay over the frequency.
- The highest CIR accuracy can be achieved using the pole-zero representation based on (3.2.13) formulation at the cost of more complexity.

## 3.3 Amplifier distortions

### 3.3.1 General considerations

To analyze the amplifier distortions, the NTI system in Fig. 2-12 is considered. The HPA polynomial representation expressed in (2.2.11) is used to characterize HPA function  $g_{HP}(\cdot)$ . This is for two reasons. On the one hand, such a representation of the HPA function eases the calculations involved in the determination of the CIR by using a sum instead of a fraction. On the other hand, it enables to extract only the dominant relevant term by truncating the polynomial order to a given  $N_{AD}$ . In the following, the single-carrier mode is first explored before characterizing the multi-carrier mode.

### 3.3.2 Single-carrier mode

#### Order $N_{AD} = 0$

Starting with the 0<sup>th</sup>-order of amplifier distortions, the approximated polynomial representation can be expressed as:

$$\mathcal{Y}(t) \approx \gamma_1(\bar{P}_{HP}^{\text{in}}) \cdot \mathcal{X}(t) , \text{ as } |\mathcal{X}(t)|^2 \approx \bar{P}_{HP}^{\text{in}} , \forall t . \quad (3.3.1)$$

In other words, the HPA function is considered linear, the system comes down to an LTI as illustrated in Fig. 2-10. This means that the corresponding CIR formula comes down to the previous filter distortions CIR (Formula 2). In that case, it

is worth noting that the HPA still entails filter distortions as represented by the impulse response  $h_{\text{HP}}(t) = (h_{\text{HP}}^{\rightarrow}(\cdot) * h_{\text{HP}}^{\leftarrow}(\cdot))(t)$ . In other words,  $N_{\text{AD}} = 0$  is a subcase of filter distortions. To take into account nonlinear effects along with the filter effects,  $N_{\text{AD}} = 1$  is considered next.

### Order $N_{\text{AD}} = 1$

Continuing with the 1<sup>st</sup>-order of amplifier distortions, the approximated polynomial representation can be expressed as:

$$\mathcal{Y}(t) \approx \gamma_1(\bar{P}_{\text{HP}}^{\text{in}}) \cdot \mathcal{X}(t) + \gamma_3(\bar{P}_{\text{HP}}^{\text{in}}) \cdot \mathcal{X}(t)|\mathcal{X}(t)|^2, \text{ as } |\mathcal{X}(t)|^2 \approx \bar{P}_{\text{HP}}^{\text{in}}, \forall t. \quad (3.3.2)$$

At this stage, it is useful to make the dependency of the CIR on  $\bar{P}_{\text{HP}}^{\text{in}}$  more explicit. Using the derivation (2.2.12), the pre-HPA impulse response can be decomposed as follows:

$$h^{\rightarrow}(t) = \bar{P}_{\text{HP}}^{\text{in}\frac{1}{2}} \cdot \tilde{h}^{\rightarrow}(t), \quad (3.3.3)$$

where  $\tilde{h}^{\rightarrow}(t)$  is the pre-HPA filter impulse response normalized such as to be unit-energy. Thus, based on the expression (3.3.2), a *novel* formula taking into account the amplifier distortions can be derived and is defined below.

#### Formula 4: Single-carrier amplifier distortions ( $N_{\text{AD}} = 1$ )

$$\left(\frac{C}{I}\right)_{\text{AD}}^{\star}(\alpha, T_s, f_{\Delta}, \bar{P}_{\text{HP}}^{\text{in}}) = \frac{\bar{P}_{\text{HP}}^{\text{in}} \cdot |\gamma_1|^2 \cdot C_1 + \bar{P}_{\text{HP}}^{\text{in}^2} \cdot 2 \cdot \Re(\gamma_1^* \gamma_3 \cdot C_2) + \bar{P}_{\text{HP}}^{\text{in}^3} \cdot |\gamma_3|^2 \cdot C_3}{\bar{P}_{\text{HP}}^{\text{in}} \cdot |\gamma_1|^2 \cdot I_1 + \bar{P}_{\text{HP}}^{\text{in}^2} \cdot 2 \cdot \Re(\gamma_1^* \gamma_3 \cdot I_2) + \bar{P}_{\text{HP}}^{\text{in}^3} \cdot |\gamma_3|^2 \cdot I_3}$$

For the interested reader, more details on the proof are provided in Appendix C.1. For more compact notations, the dependency of the complex coefficients  $\gamma_1$  and  $\gamma_3$  on  $\bar{P}_{\text{HP}}^{\text{in}}$  is dropped. In this expression, the useful information and interference coefficients are defined as follows:

$$C_1 = |h^{\star}(0)|^2, \quad (3.3.4a)$$

$$C_2 = r_1 \cdot h^{\star\star}(0)h^{\star}(0, 0, 0) + 2 \cdot h^{\star\star}(0) \sum_{k \in \mathbb{Z}^*} h^{\star}(0, k, k), \quad (3.3.4b)$$

$$C_3 = r_2 \cdot |h^{\star}(0, 0, 0)|^2 + 4 \cdot r_1 \cdot \Re \left( h^{\star\star}(0, 0, 0) \sum_{k \in \mathbb{Z}^*} h^{\star}(0, k, k) \right) + 4 \cdot \left| \sum_{k \in \mathbb{Z}^*} h^{\star}(0, k, k) \right|^2, \quad (3.3.4c)$$

$$I_1 = \sum_{k \in \mathbb{Z}^*} |h^{\star}(k)|^2, \quad (3.3.4d)$$

$$I_2 = 2 \cdot \sum_{k_1 \in \mathbb{Z}^*} h^{\star\star}(k_1)h^{\star}(k_1, 0, 0) + \sum_{k_1 \in \mathbb{Z}^*} \sum_{\substack{k_2 \in \mathbb{Z}^* \\ k_1 \neq k_2}} h^{\star\star}(k_1)h^{\star}(k_1, k_2, k_2), \quad (3.3.4e)$$

$$I_3 = 3 \cdot r_1 \cdot \sum_{k \in \mathbb{Z}^*} (|h^{\star}(k, 0, 0)|^2 + |h^{\star}(0, k, k)|^2) + 3 \cdot \sum_{k_1 \in \mathbb{Z}^*} \sum_{\substack{k_2 \in \mathbb{Z}^* \\ k_1 \neq k_2}} |h^{\star}(0, k_1, k_2)|^2$$

$$+ \sum_{k_1 \in \mathbb{Z}^*} \sum_{\substack{k_2 \in \mathbb{Z}^* \\ k_1 \neq k_2}} \sum_{\substack{k_3 \in \mathbb{Z}^* \\ k_2 \neq k_3}} |h^*(k_1, k_2, k_3)|^2 + 2 \cdot \sum_{k_1 \in \mathbb{Z}^*} \sum_{\substack{k_2 \in \mathbb{Z}^* \\ k_1 \neq k_2}} \sum_{\substack{k_3 \in \mathbb{Z}^* \\ k_1 \neq k_3 \\ k_2 \neq k_3}} h^*(k_1, k_2, k_2) h^{**}(k_3, k_1, k_3) . \quad (3.3.4f)$$

These coefficients are based on the 1<sup>st</sup>-order and 3<sup>rd</sup>-order system impulse responses defined at optimal decision instant offset  $\tau^*$ . These impulse responses can be compactly defined as:

$$h^*(k_1) = \int_{\mathbb{R}} \tilde{h}^{\rightarrow}((\tau^* + k_1)T_s - u) h^{\leftarrow}(u) du , \quad (3.3.5a)$$

$$h^*(k_1, k_2, k_3) = \int_{\mathbb{R}} \tilde{h}^{\rightarrow}((\tau^* + k_1)T_s - u) \tilde{h}^{\rightarrow}((\tau^* + k_2)T_s - u) \tilde{h}^{\rightarrow*}((\tau^* + k_3)T_s - u) h^{\leftarrow}(u) du , \quad (3.3.5b)$$

which are closely related to the notion of Volterra kernel [109]. Finally, the modulation coefficients can be expressed as:

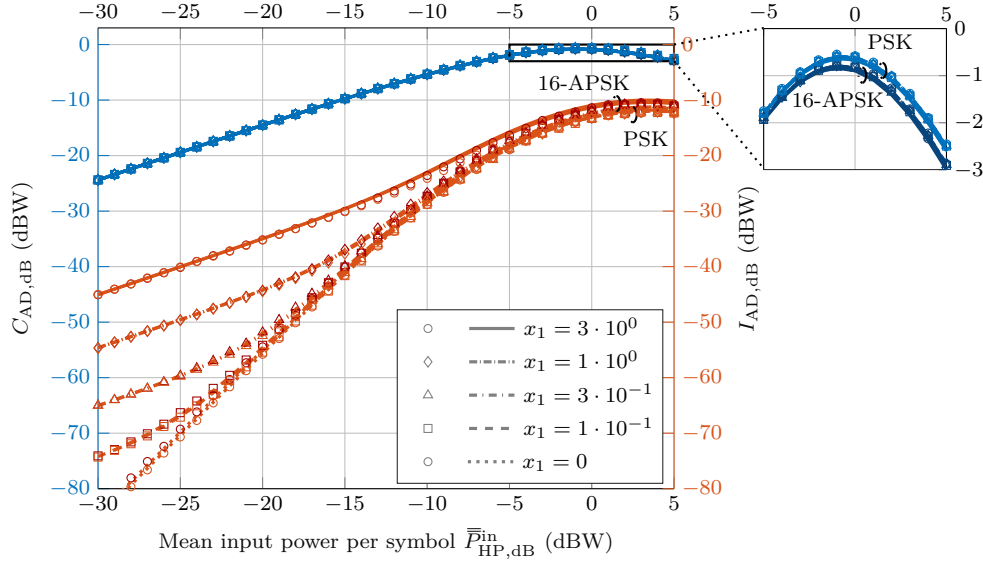
$$r_n = \begin{cases} 1, & \text{if PSK modulation} \\ 4^{n-1} \cdot \frac{1 + 3v_1^{2n}}{(1 + 3v_1^2)^n}, & \text{if 16-APSK modulation} \end{cases} , \quad n \geq 1 , \quad (3.3.6)$$

which are exposed in more detail in Appendix B.4. These coefficients translate the influence of non-unit IAPR for higher order modulations such as 16-APSK.

Due to the complex formulation of the amplifier distortions, it is important to first get an intuition on the behavior of the transformed useful information power  $C_{AD}$  and interference power  $I_{AD}$  separately. For this purpose, the two quantities are illustrated in Fig. 3-9 in the case of  $N_{AD} = 1$ . They are represented as a function of the mean input power per symbol and for PSK and 16-APSK modulations. For the sake of illustration, only post-HPA filter distortions are considered. It means that in this scenario the normalized pre-HPA filter can be simplified<sup>11</sup> to  $\tilde{h}^{\rightarrow}(t) = h_{SC}(t, \alpha, T_s)$ . It is assumed that the post-HPA filter  $\tilde{h}^{\leftarrow}(t)$  contains gain slope distortions. This scenario would typically occur when OMUX filter distortions are dominant and the carrier under study is placed at the edge of the channel nominal bandwidth. Thus, the filter distortions are characterized by  $x_1$  and expressed in (dB/MHz) · (Mbauds). Furthermore, a representative roll-off  $\alpha = 0.1$  and ring ratio  $v_1 = 3.15$  (used in [71] with coding rates 0.5925 and 0.6592) are considered. The decision instant offset  $\tau$  is set to zero, since it does not alter the conclusions and enables a more precise validation of the formulas numerically.  $x_1$  is expressed in (dB/MHz) · (Mbauds). Finally, each infinite sum is truncated to the partial sum limit  $L = 10$ .

It can be observed that the useful information power follows closely AM/AM curve of the HPA illustrated in Fig. 2-13 with some slight differences. As opposed to the instantaneous power of the AM/AM curve, the characterization relies on the mean input power per symbol. Thus, the impact of the IAPR can be observed.

<sup>11</sup>The SC filter is already defined as unit-energy.

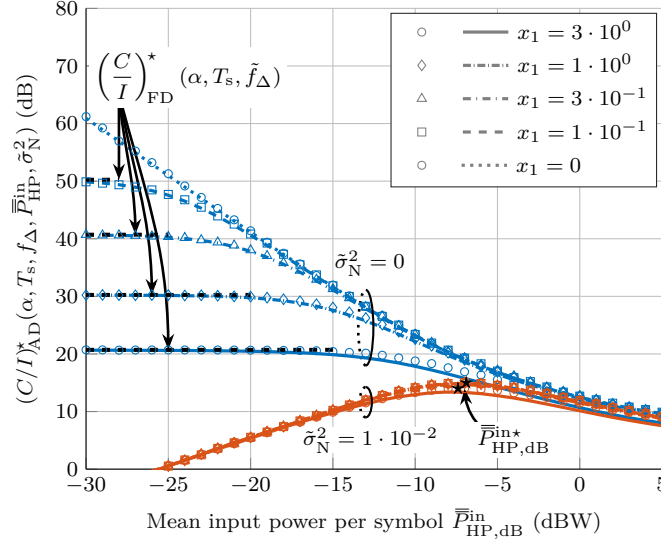
Figure 3-9: Amplifier distortions analysis ( $N_{AD} = 1$ )

First of all, the non-constant IAPR of the pre-HPA filter over time can be noticed, since the useful information power does not reach the saturation point at 0 dB for both modulation schemes. On top of that, the useful information power of PSK modulations is higher than the one of 16-APSK modulations in the nonlinear region, since the 16-APSK modulation has also a non-unit IAPR at a given time instant. Regarding the interference power, it is lower for PSK modulations than for 16-APSK modulations in the nonlinear region. This means that the impairment of the IAPR impacts both  $C_{AD}$  and  $I_{AD}$ . In the calculations, this effect is taken into account by modulation coefficients  $\{r_n\}_{n \geq 1}$ .

Moreover, the influence of post-HPA filter distortions on the useful information power can be considered negligible for all mean input powers. However, they do play an important role in the interference power. Indeed, the amplifier distortions CIR (Formula 4) tends towards the filter distortions CIR (Formula 2) as the mean input power gets lower, i.e.:

$$\left(\frac{C}{I}\right)_{AD}^* (\alpha, T_s, f_\Delta, \bar{P}_{HP}^{\text{in}}) \rightarrow \left(\frac{C}{I}\right)_{FD}^* (\alpha, T_s, f_\Delta), \text{ as } \bar{P}_{HP}^{\text{in}} \rightarrow 0. \quad (3.3.7)$$

This can be noticed by the influence of  $x_1$  on  $I$ . Besides that, the level of dominance of the filter distortions does not only depend on how low  $\bar{P}_{HP}^{\text{in}}$  is, but also on how high the coefficient  $I_1$  is. In other words, the linear region of the HPA (where filter distortions are dominant and which is independent of the linear modulation type) is variable. This variability is especially noticeable on the CIR as illustrated in Fig. 3-

Figure 3-10: Amplifier distortions CIR ( $N_{AD} = 1$ )

10 (blue curves). On this graph, the asymptote (3.3.7) is depicted given  $x_1 \in \{0, 1 \cdot 10^{-1}, 3 \cdot 10^{-1}, 1 \cdot 10^0, 3 \cdot 10^0\}$  dB/MHz  $\cdot$  Mbauds. It is observed that the filter distortions influence a wider range of  $\bar{P}_{HP}^{in}$  with higher  $x_1$ .

Moreover, it is worth noting that in a noiseless environment the CIR is strictly decreasing with increasing  $\bar{P}_{HP}^{in}$  until saturation. By contrast, introducing a post-HPA AG noise leads to a unique optimal mean input per symbol maximizing the CIR, which is denoted by  $\bar{P}_{HP}^{in*}$ . Indeed,  $\bar{P}_{HP}^{in*}$  constitutes a trade-off between the limitation of amplifier distortions impairment (in favor of a decrease of  $\bar{P}_{HP}^{in}$ ) and the limitation of noise impairment (in favor of an increase of  $\bar{P}_{HP}^{in}$ ). Here, the impact of a noise with a received normalized power at decision instant of  $\tilde{\sigma}_N^2 = 1 \cdot 10^{-2}$  W is illustrated. Accounting for the noise in the CIR expression simply means adding  $\tilde{\sigma}_N^2$  to the denominator. Thus, in the context of the single-carrier 1<sup>st</sup>-order amplifier distortions, optimizing the mean power at HPA input relies on the following equation:

$$\frac{\partial \left( \frac{C}{I} \right)_{AD}^* (\alpha, T_s, f_{\Delta}, \bar{P}_{HP}^{in*}, \tilde{\sigma}_N^2)}{\partial \bar{P}_{HP}^{in}} = 0, \quad (3.3.8)$$

which comes down to a quartic equation in  $\bar{P}_{HP}^{in}$  that can be solved analytically using radicals [110]. This leads to the mean input power maximizing<sup>12</sup> the CIR. For the proposed range of  $x_1 > 0$ ,  $\bar{P}_{HP,dB}^{in*}$  lies in the range [6.9, 7.4] dBW. While the optimal HPA input power (or input back-off) is almost exclusively determined through simulations in the literature [111], this type of derivation opens new possibilities of determination of more time-efficient mathematical solutions. As a last note, more information about the impact of the roll-off can be found in [C2].

<sup>12</sup>When  $N_{AD} \geq 2$ , the solution is an analytical estimate.

### Order $N_{AD} \geq 2$

In practical systems, compensation methods such as predistortion are used to limit the impairment caused by amplifier distortions [58, 112]. This makes the solution derived for  $N_{AD} = 1$  particularly attractive. In particular, the study of  $N_{AD} \geq 2$  does not seem necessary in the presence of lower levels of nonlinearities. However, if a cubic predistorter is implemented [113] and the HPA operates near saturation, it is recommended to derive the CIR formula for the 2<sup>nd</sup>-order amplifier distortions. Still, there is a significant limitation in complexity due to the quintuple sum of 5<sup>th</sup> order system impulse responses involved in the calculations<sup>13</sup>. In that case, the polynomial representation approximation of the HPA may no longer be beneficial. Thus, deriving the CIR based on the exact HPA function, as expressed in (2.2.10) in the context of the Saleh model, tends to become preferable.

### 3.3.3 Multi-carrier mode

#### General considerations

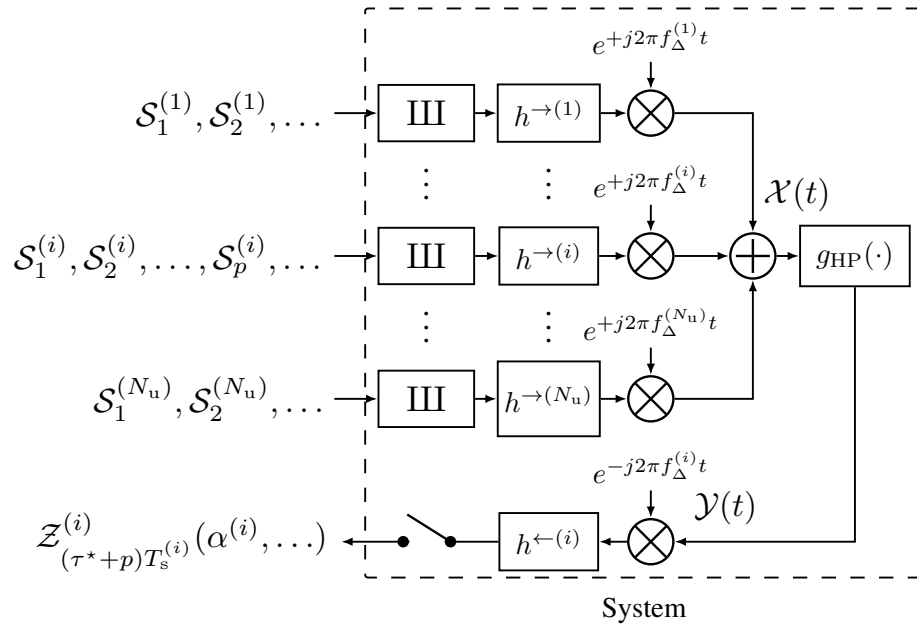


Figure 3-11: Multi-user system model from the perspective of the  $i^{\text{th}}$ -user

The multi-user NTI system model is illustrated in Fig. 3-11 as an extension of the single-user system model presented in Fig. 2-12. It is considered that the  $i^{\text{th}}$ -user transmit symbols, denoted by  $\{\mathcal{S}_q^{(i)}\}_{1 \leq q \leq N_s}$ , are pairwise uncorrelated with the symbols of other users,  $\forall i \in \{1, 2, \dots, N_u\}$ . For the sake of simplicity, transmitters are assumed to be synchronized. Furthermore, the  $i^{\text{th}}$ -user carrier placement, symbol

<sup>13</sup>This can theoretically be avoided if the exact value of the sums is determined (as performed with the roll-off polynomials in Formula 3), but it appears significantly more challenging.

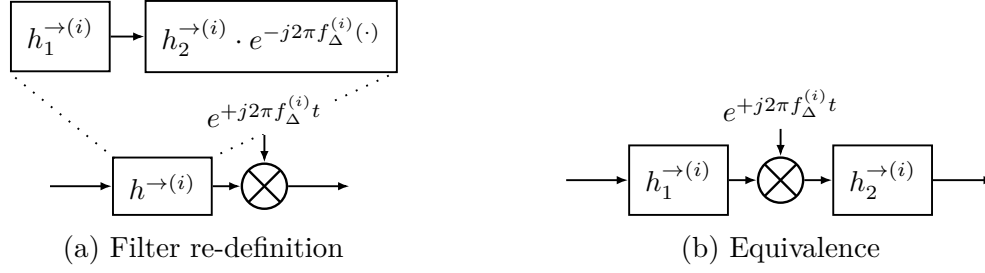


Figure 3-12: Example of pre-HPA filter insertion.

rate, roll-off, and modulation coefficients are denoted by  $f_{\Delta}^{(i)}$ ,  $T_s^{(i)}$ ,  $\alpha^{(i)}$ ,  $\{r_n^{(i)}\}_{n \geq 1}$ , respectively. It is assumed that the placement of the carrier is performed by the OBP. The corresponding downconversion is performed at the user receiver terminal. This system model is purposefully represented in a compact manner such as to simplify the definition of the 1<sup>st</sup>-order and 3<sup>rd</sup>-order multi-user system impulse responses. Indeed, only one pre-HPA filter impulse response is represented. However, an additional filter can still be taken into account between the upconversion and the HPA by re-defining the pre-HPA filter as illustrated in Fig. 3-12a. Thus, this leads to an equivalence with the subsystem presented in Fig. 3-12b. The same principle applies to a filter between the HPA and the downconversion.

By extension of the notation used for the single-carrier mode, the pre-HPA filter impulse response of the  $i^{\text{th}}$ -user is defined as:

$$h^{\rightarrow(i)}(t) = \bar{P}_{\text{HP}}^{\text{in}(i)\frac{1}{2}} \cdot \tilde{h}^{\rightarrow(i)}(t), \quad i \in \{1, 2, \dots, N_u\}, \quad (3.3.9)$$

where  $\bar{P}_{\text{HP}}^{\text{in}(i)}$  is the mean power per symbol at HPA input of the  $i^{\text{th}}$ -user. However, in multi-carrier mode, the mean power at HPA input must be derived based on the mean power per symbol given all users. Thus, the multi-user mean power per symbol at HPA input is derived as follows:

$$\begin{aligned}
 \bar{P}_{\text{HP}}^{\text{in}} &= \frac{1}{N_s} \cdot \int_{\mathbb{R}} \bar{P}_{\text{HP}}^{\text{in}}(t) dt \\
 &= \frac{1}{N_s} \cdot \int_{\mathbb{R}} \mathbb{E}[|\mathcal{X}(t)|^2] dt \\
 &= \frac{1}{N_s} \cdot \int_{\mathbb{R}} \mathbb{E} \left[ \left| \sum_{i=1}^{N_u} \sum_{q=0}^{N_s-1} \mathcal{S}_q^{(i)} \cdot h^{\rightarrow(i)}(t - qT_s^{(i)}) \cdot e^{j2\pi f_{\Delta}^{(i)}t} \right|^2 \right] dt \\
 &\stackrel{\text{Same derivation as (2.2.12)}}{=} \frac{1}{N_s} \cdot \sum_{i=1}^{N_u} \sum_{q=0}^{N_s-1} \int_{\mathbb{R}} |h^{\rightarrow(i)}(t - qT_s^{(i)})|^2 dt \\
 &\stackrel{\text{Time-shift invariance}}{=} \sum_{i=1}^{N_u} \int_{\mathbb{R}} |h^{\rightarrow(i)}(t)|^2 dt
 \end{aligned}$$



$$\stackrel{\text{Definition (3.3.9)}}{=} \sum_{i=1}^{N_u} \bar{\bar{P}}_{\text{HP}}^{\text{in}(i)}, \quad \forall N_s, \quad (3.3.10)$$

which is used for the polynomial representation approximation of the HPA. Thus, the amplifier distortions CIR related to the  $i^{\text{th}}$ -user requires several adaptations of the single carrier Formula 4 ( $N_{\text{AD}} = 1$ ). Indeed, the complex coefficients  $\gamma_1$  and  $\gamma_3$  are computed based on the updated multi-carrier definition of  $\bar{\bar{P}}_{\text{HP}}^{\text{in}}$  provided in (3.3.10). From this point, two key concepts need to be introduced: *power sharing* and *intermodulation products*.

### Power sharing

Firstly, it can be convenient to define power sharing ratios as  $\lambda_{\text{HP}}^{(i)} = \bar{\bar{P}}_{\text{HP}}^{\text{in}(i)} / \bar{\bar{P}}_{\text{HP}}^{\text{in}}$ ,  $\forall i \in \{1, 2, \dots, N_u\}$ , to characterize the power distribution among the carriers at the HPA input. This results in the following power constraint:

$$\sum_{i=1}^{N_u} \lambda_{\text{HP}}^{(i)} = 1, \quad (3.3.11)$$

which is derived from the definition (3.3.10). For later more compact notations, the power ratio between the  $q^{\text{th}}$  and  $i^{\text{th}}$  users is defined as  $\lambda_{\text{HP}}^{(q,i)} = \lambda_{\text{HP}}^{(q)} / \lambda_{\text{HP}}^{(i)}$ . On this basis, the *novel*  $i^{\text{th}}$ -user useful information power  $C_{\text{AD}}^{(i)}$  expression can be introduced. It can be formulated as:

$$\begin{aligned} C_{\text{AD}}^{(i)} = & \bar{\bar{P}}_{\text{HP}}^{\text{in}} \cdot |\gamma_1|^2 \cdot \left[ \lambda_{\text{HP}}^{(i)} \cdot C_{1,1}^{(i)} \right. \\ & + \bar{\bar{P}}_{\text{HP}}^{\text{in}^2} \cdot 2 \cdot \Re \left( \gamma_1^* \gamma_3 \cdot \left[ \lambda_{\text{HP}}^{(i)^2} \cdot C_{2,1}^{(i)} + \boxed{\lambda_{\text{HP}}^{(i)} \cdot \sum_{\substack{q=1 \\ q \neq i}}^{N_u} \lambda_{\text{HP}}^{(q)} \cdot C_{2,2}^{(i,q)}} \right] \right) \\ & + \bar{\bar{P}}_{\text{HP}}^{\text{in}^3} \cdot |\gamma_3|^2 \cdot \left[ \lambda_{\text{HP}}^{(i)^3} \cdot C_{3,1}^{(i)} + \boxed{\lambda_{\text{HP}}^{(i)^2} \cdot \sum_{\substack{q=1 \\ q \neq i}}^{N_u} \lambda_{\text{HP}}^{(q)} \cdot C_{3,2}^{(i,q)} + \lambda_{\text{HP}}^{(i)} \cdot \sum_{\substack{q=1 \\ q \neq i}}^{N_u} \lambda_{\text{HP}}^{(q)^2} \cdot C_{3,3}^{(i,q)}} \right. \\ & \left. \left. + \boxed{\lambda_{\text{HP}}^{(i)} \cdot \sum_{\substack{q=1 \\ q \neq i}}^{N_u} \sum_{\substack{l=1 \\ l \neq i \\ l > q}}^{N_u} \lambda_{\text{HP}}^{(q)} \cdot \lambda_{\text{HP}}^{(l)} \cdot C_{3,4}^{(i,q,l)}} \right] \right], \quad (3.3.12) \end{aligned}$$

$\forall N_u \geq 1$ , where  $C_{2,2}^{(i,q)}$ ,  $C_{3,2}^{(i,q)}$ ,  $C_{3,3}^{(i,q)}$ ,  $C_{3,4}^{(i,q,l)}$  are multi-user useful information coefficients. They can be expressed as:

$$C_{2,2}^{(i,q)} = 2 \cdot h^{*(i,i)*}(0;0) \cdot \sum_{k \in \mathbb{Z}} h^{*(i,q,q,i)}(0, k, k; 0), \quad (3.3.13a)$$

$$C_{3,2}^{(i,q)} = 4 \cdot \Re \left( \left( r_1^{(i)} \cdot h^{*(i,i,i,i)*}(0,0,0;0) + 2 \cdot \sum_{k \in \mathbb{Z}^*} h^{*(i,i,i,i)*}(0,k,k;0) \right) \cdot \sum_{k \in \mathbb{Z}} h^{*(i,q,q,i)}(0,k,k;0) \right), \quad (3.3.13b)$$

$$C_{3,3}^{(i,q)} = 4 \cdot \sum_{k \in \mathbb{Z}} |h^{*(i,q,q,i)}(0,k,k;0)|^2, \quad (3.3.13c)$$

$$C_{3,4}^{(i,q,l)} = 8 \cdot \sum_{k_1 \in \mathbb{Z}} \sum_{k_2 \in \mathbb{Z}} h^{*(i,q,q,i)*}(0,k_1,k_1;0) \cdot h^{*(i,l,l,i)}(0,k_2,k_2;0), \quad (3.3.13d)$$

which are based on the 1<sup>st</sup>-order and 3<sup>rd</sup>-order multi-user system impulse responses defined at optimal decision instant offset  $\tau^*$ . These impulse responses can be expressed as:

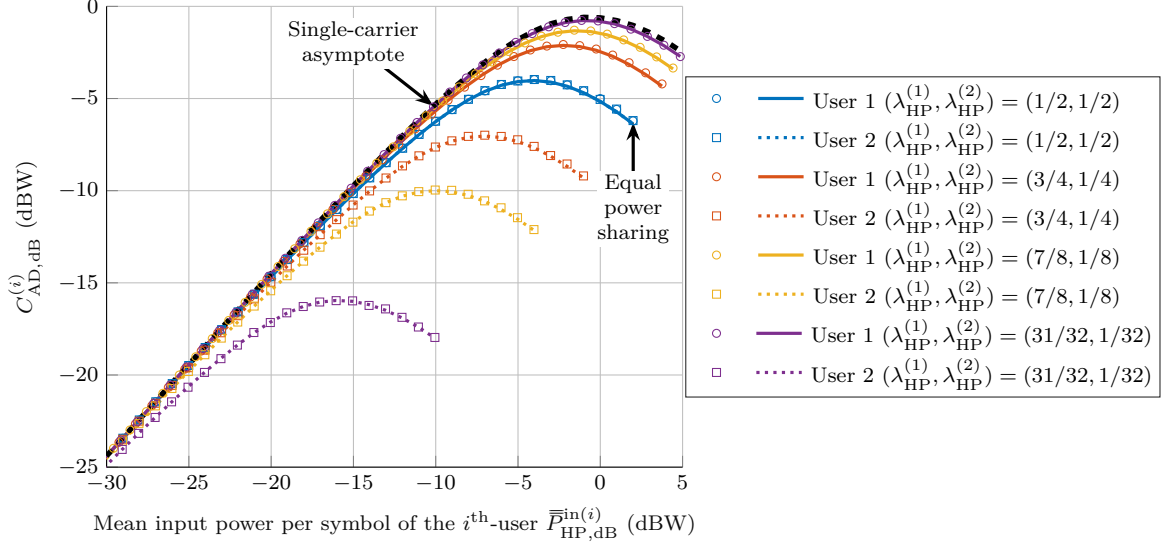
$$h^{*(i_1,i_2)}(k_1; f_\Delta) = \int_{\mathbb{R}} \tilde{h}^{\rightarrow(i_1)} \left( \left( p(\zeta^{(i_2,i_1)} - 1) + \tau^* \zeta^{(i_2,i_1)} + k_1 \right) T_s^{(i_1)} - u \right) h^{\leftarrow(i_2)}(u) \cdot e^{j2\pi f_\Delta ((\tau^* + pT_s^{(i_2)}) - u)} du, \quad (3.3.14a)$$

$$h^{*(i_1,i_2,i_3,i_4)}(k_1,k_2,k_3; f_\Delta) = \int_{\mathbb{R}} \tilde{h}^{\rightarrow(i_1)} \left( \left( p(\zeta^{(i_4,i_1)} - 1) + \tau^* \zeta^{(i_4,i_1)} + k_1 \right) T_s^{(i_1)} - u \right) \tilde{h}^{\rightarrow(i_2)} \left( \left( p(\zeta^{(i_4,i_2)} - 1) + \tau^* \zeta^{(i_4,i_2)} + k_2 \right) T_s^{(i_2)} - u \right) \tilde{h}^{\rightarrow(i_3)*} \left( \left( p(\zeta^{(i_4,i_3)} - 1) + \tau^* \zeta^{(i_4,i_3)} + k_3 \right) T_s^{(i_3)} - u \right) h^{\leftarrow(i_4)}(u) \cdot e^{j2\pi f_\Delta ((\tau^* + pT_s^{(i_4)}) - u)} du, \quad (3.3.14b)$$

where the symbol period ratio between the  $q^{\text{th}}$  and  $i^{\text{th}}$  users is defined as  $\zeta^{(q,i)} = T_s^{(q)}/T_s^{(i)}$ . They constitute a generalized form of the previously defined single-carrier 1<sup>st</sup>-order and 3<sup>rd</sup>-order impulse responses (3.3.5a) and (3.3.5b). The latter ones can be retrieved in the case  $i_1 = i_2 = i_3 = i_4$  and  $f_\Delta = 0$ . The interested reader can find more information on the proof in Appendix C.1. It is worth noting that the terms for  $k = 0$  are included in the sums involving the  $q^{\text{th}}$ -adjacent carrier and that the coefficients are independent of the placement of the carriers. The terms enclosed in dotted boxes in (3.3.12) come from the HPA amplification in multi-carrier mode. Although, the useful information power of a given user is more limited due to the power sharing (characterized by the introduction of  $\lambda_{\text{HP}}^{(i)}$ ), these extra terms further boost the useful information power due to the multi-carrier operation. However, the increase is not equal for all carriers. Indeed, carriers with higher mean input power get more increase than carriers with lower mean input power. This is the so-called *capture effect* (or *power robbing*<sup>14</sup>), which is explained in more detail in [19]. Lastly,  $C_{\text{AD}}^{(i)}$  is independent of the modulation of any  $q^{\text{th}}$ -user,  $\forall q \neq i$ .

For the sake of illustration, the useful information power per user is depicted in 3-13 in a simplified two-user system. In this scenario, the roll-offs of user 1 and user 2

<sup>14</sup>The widespread term *power robbing* can be misleading, since the useful information power of all carriers is increased due to the multi-carrier operation. It is, however, the unequal distribution of power between carriers is the origin of this phenomenon.

Figure 3-13: Two-carrier power sharing ( $N_{AD} = 1$ )

are assumed to be  $\alpha^{(1)} = \alpha^{(2)} = 0.1$ . The pre-HPA and post-HPA of user 1 and user 2 are considered free of filter distortions such that  $\tilde{h}^{\rightarrow(1)}(t) = \tilde{h}^{\rightarrow(2)}(t) = \tilde{h}^{\leftarrow(1)}(t) = \tilde{h}^{\leftarrow(2)}(t) = h_{SC}(t, 0.1, T_s)$ . This implies that the symbol periods of user 1 and user 2 are considered equal, i.e.  $T_s^{(1)} = T_s^{(2)} = T_s$ . This also leads to  $\zeta^{(1,2)} = \zeta^{(2,1)} = 1$  and thus, an important simplification of the 1<sup>st</sup>-order and 3<sup>rd</sup>-order multi-user system impulse responses. In fact, any value of  $T_s$  can be chosen, since the expression of (3.3.12) becomes independent of the symbol period in such a scenario. Furthermore, the expression is also independent of the placement of the carriers within the HPA bandwidth. Finally, different power sharing are explored and characterized by the set of values  $(\lambda_{HP}^{(1)}, \lambda_{HP}^{(2)})$ .

At equal power, it can be noticed that the power loss at saturation caused by the power sharing is approximately 3.4 dB, which is a typical order of loss [19]. At imbalanced power, the carrier with higher mean input power converges towards the single-carrier characteristic. In other words,  $C_{AD}^{(1,2)} \rightarrow C_{AD}$ , as  $\lambda_{HP}^{(1,2)} \rightarrow +\infty$ . Thus, the terms involving  $\lambda_{HP}^{(2)}$  become negligible as  $\lambda_{HP}^{(1)}$  increases relative to  $\lambda_{HP}^{(2)}$ .

### Intermodulation products

As a next step, the interference power of the  $i^{\text{th}}$ -user is investigated. It highly relies on the placements of the carriers and the so-called *intermodulation products*. Performing the HPA operation  $g_{HP}(\cdot)$  on the multi-carrier signal leads inexorably to components at frequencies that result from a linear combination of the carrier frequencies at the HPA input. It is worth noting that the intermodulation products known to be most troublesome are located at post-HPA frequencies<sup>15</sup>:  $2f_{\Delta}^{(1)} - f_{\Delta}^{(2)}$  (Type 1) and  $f_{\Delta}^{(1)} + f_{\Delta}^{(2)} - f_{\Delta}^{(3)}$  (Type 2) [19]. In the two-carrier example provided in Appendix C.1, the 5<sup>th</sup> and 7<sup>th</sup> terms of the received signal in (C.1.7) can be classified

<sup>15</sup>Frequencies are defined before downconversion of the user terminal receiver.

as intermodulation products of Type 1. Besides that, the intermodulation products of Type 2 appear only from  $N_u \geq 3$ .

On this basis, the *novel*  $i^{\text{th}}$ -user interference power  $I_{\text{AD}}^{(i)}$  expression can be introduced. It can be formulated as:

$$\begin{aligned}
 I_{\text{AD}}^{(i)} = & \bar{P}_{\text{HP}}^{\text{in}} \cdot |\gamma_1|^2 \cdot \left[ \lambda_{\text{HP}}^{(i)} \cdot I_{1,1}^{(i)} \right. \\
 & + \bar{P}_{\text{HP}}^{\text{in}^2} \cdot 2 \cdot \Re \left( \gamma_1^* \gamma_3 \cdot \left[ \lambda_{\text{HP}}^{(i)^2} \cdot I_{2,1}^{(i)} + \boxed{\lambda_{\text{HP}}^{(i)} \cdot \sum_{\substack{q=1 \\ q \neq i}}^{N_u} \lambda_{\text{HP}}^{(q)} \cdot I_{2,2}^{(i,q)} + \sum_{\substack{q=1 \\ q \neq i}}^{N_u} \sum_{\substack{l=1 \\ l \neq i}}^{N_u} \lambda_{\text{HP}}^{(q)} \cdot \lambda_{\text{HP}}^{(l)} \cdot I_{2,3}^{(q,l)}} \right] \right) \\
 & + \bar{P}_{\text{HP}}^{\text{in}^3} \cdot |\gamma_3|^2 \cdot \left[ \lambda_{\text{HP}}^{(i)^3} \cdot I_{3,1}^{(i)} + \boxed{\lambda_{\text{HP}}^{(i)^2} \cdot \sum_{\substack{q=1 \\ q \neq i}}^{N_u} \lambda_{\text{HP}}^{(q)} \cdot I_{3,2}^{(i,q)} + \lambda_{\text{HP}}^{(i)} \cdot \sum_{\substack{q=1 \\ q \neq i}}^{N_u} \lambda_{\text{HP}}^{(q)^2} \cdot I_{3,3}^{(i,q)}} \right. \\
 & \left. + \boxed{\lambda_{\text{HP}}^{(i)} \cdot \sum_{\substack{q=1 \\ q \neq i}}^{N_u} \sum_{\substack{l=1 \\ l \neq i}}^{N_u} \lambda_{\text{HP}}^{(q)} \cdot \lambda_{\text{HP}}^{(l)} \cdot I_{3,4}^{(i,q,l)} + \sum_{\substack{q=1 \\ q \neq i}}^{N_u} \sum_{\substack{l=1 \\ l \neq i}}^{N_u} \sum_{\substack{m=1 \\ m \neq i}}^{N_u} \lambda_{\text{HP}}^{(q)} \cdot \lambda_{\text{HP}}^{(l)} \cdot \lambda_{\text{HP}}^{(m)} \cdot I_{3,5}^{(q,l,m)}} \right] \Bigg], \tag{3.3.15}
 \end{aligned}$$

where  $I_{2,2}^{(i,q)}$ ,  $I_{2,3}^{(q,l)}$ ,  $I_{3,2}^{(i,q)}$ ,  $I_{3,3}^{(i,q)}$ ,  $I_{3,4}^{(i,q,l)}$ ,  $I_{3,5}^{(q,l,m)}$  are multi-user interference coefficients. It can be noticed that the intermodulation products are sometimes treated as an additive impairment for simplification. It means that only the terms, which are uncorrelated with the  $i^{\text{th}}$  user, are considered. In the case of  $N_{\text{AD}} = 1$  and expression (3.3.15), it corresponds to the coefficients  $I_{2,3}^{(q,l)}$  and  $I_{3,5}^{(q,l,m)}$ . This analysis leads to the multi-carrier amplifier distortions CIR defined below.

**Formula 5: Multi-carrier amplifier distortions for  $i^{\text{th}}$ -user ( $N_{\text{AD}} = 1$ )**

$$\left( \frac{C}{I} \right)_{\text{AD}}^{(i)\star} (\alpha^{(i)}, T_s^{(i)}, f_{\Delta}^{(i)}, \lambda_{\text{HP}}^{(i)}, \bar{P}_{\text{HP}}^{\text{in}}) = \left( \frac{C_{\text{AD}}^{(i)}}{I_{\text{AD}}^{(i)}} \right)^{\star}$$

where  $C_{\text{AD}}^{(i)}$  and  $I_{\text{AD}}^{(i)}$  are defined in (3.3.12) and (3.3.15), respectively. The CIR is defined based on the optimal decision of  $\tau^*$ .

In the end, Formula 5 is the most complex CIR expression of this thesis, since it accounts for numerous phenomena such as filtering, nonlinearities, and power distributions. To demonstrate its applicability, a step-by-step calculation procedure is provided in the next chapter in a realistic scenario. The interested reader can also refer to Appendix C.4 which exposes the detailed derivation of the linear adjacent carrier interference CIR. Indeed, this CIR is a subcase of interest of Formula 5 and results in an expression with significantly lower complexity. This derivation especially sheds light on the mathematical manipulations and key parameters such as the symbol period ratio  $\zeta^{(q,i)}$ , power ratio  $\lambda_{\text{HP}}^{(q,i)}$  and inter-carrier distance.

### Main findings on amplifier distortions

To finalize this section, we can draw the following conclusions:

- Low-complexity Formula 4 and Formula 5 can be used to compute the amplifier distortions CIR in single-carrier mode and multi-carrier mode.
- Their accuracy is higher in the presence of lower levels of nonlinearities, which is typically in the case of a predistorted amplifier characteristic.

## 3.4 Oscillator noise

### 3.4.1 General considerations

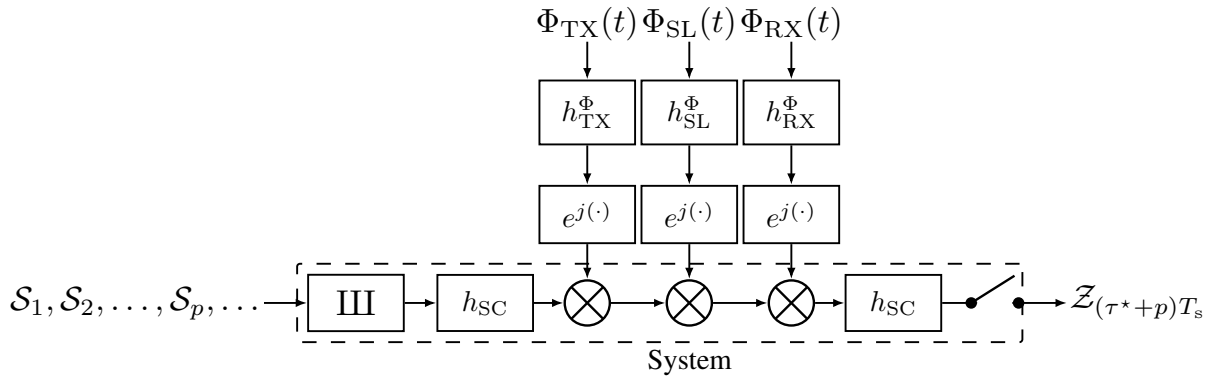


Figure 3-14: Simplified oscillator noise system model

The simplified system model for the characterization of the oscillator noises is illustrated in Fig. 3-14. As improvement with respect to the state-of-the-art, it includes the pulse shaping and phase noise mask characteristic. However, the effect of filter distortions and amplifier distortions is still neglected.

In practice, it is more convenient to define one aggregated phase noise that takes into account the statistical property of the transmitter, satellite, and receiver phase noises. Here, the same procedure as in Section 2.2.4 is used to define the aggregated phase noise. Thus,  $\Phi(t)$  is considered as a random process that is convoluted by the impulse response of the aggregated phase noise mask filter denoted by  $h^{\Phi}(t)$ . This results in the aggregated phase noise defined as  $\Theta(t) = \text{mod}((\Phi * h^{\Phi})(t), 2\pi)$ . Furthermore, the definition of the aggregated phase noise  $\Theta(t)$  must fulfill the same statistical properties as  $\Theta_{TX}(t) + \Theta_{SL}(t) + \Theta_{RX}(t)$ ,  $\forall t$ . This means that the following requirements must be met:

$$\mathbb{E}[\Theta(t)] = \mathbb{E}[\Theta_{TX}(t)] + \mathbb{E}[\Theta_{SL}(t)] + \mathbb{E}[\Theta_{RX}(t)], \forall t, \quad (3.4.1a)$$

$$\mathbb{V}[\Theta(t)] = \mathbb{V}[\Theta_{TX}(t)] + \mathbb{V}[\Theta_{SL}(t)] + \mathbb{V}[\Theta_{RX}(t)], \forall t, \quad (3.4.1b)$$

and  $\Theta_{\text{TX}}(t)$  must be Gaussian since the sum of uncorrelated Gaussian processes is a Gaussian process. Moreover, it is reminded that the variance of the aggregated phase noise can be rewritten as  $\mathbb{V}[\Theta(t)] = \varepsilon_{\Phi, \text{tot}}$ , where  $\varepsilon_{\Phi, \text{tot}}$  is the filter energy of the aggregated phase noise mask. One immediate solution is to define the aggregate phase noise mask as:

$$h^\Phi(t) = h_{\text{TX}}^\Phi(t) + h_{\text{SL}}^\Phi(t) + h_{\text{RX}}^\Phi(t) , \quad (3.4.2)$$

and also define  $\Phi(t)$  as a real zero-mean unit-power white Gaussian process. An example of aggregated phase noise mask frequency characteristic is provided in Fig. 2-14 based on this definition.

### 3.4.2 Analysis

Based on these considerations, the *novel* CIR formula corresponding to the simplified system model presented in Fig. 3-14 is defined below.

#### Formula 6: Oscillator noise

$$\left(\frac{C}{I}\right)_{\text{ON}}^*(\alpha, T_s, h^\Phi) = \frac{1}{\sum_{(k_1, k_2) \in \mathbb{Z}_{(u, v)}^2} \iint_{(u, v) \in \mathbb{R}^2} h_{\text{SC}}(k_1 T_s - u, \alpha, T_s) h_{\text{SC}}(k_2 T_s - v, \alpha, T_s) \cdot h_{\text{SC}}(u, \alpha, T_s) h_{\text{SC}}(v, \alpha, T_s) \cdot (e^{\varepsilon_{\Phi}(u, v)} - 1) \, du \, dv}$$

where the aggregate phase noise mask filter autocorrelation is:

$$\varepsilon_{\Phi}(u, v) = \int_{\mathbb{R}} h^\Phi(t + (u - v)) h^{\Phi*}(t) \, dt . \quad (3.4.3)$$

A particular case of the autocorrelation (3.4.3) is the aggregate phase noise mask filter energy where  $\varepsilon_{\Phi}(u, u) = \varepsilon_{\Phi, \text{tot}}$ ,  $\forall u \in \mathbb{R}$ . The interested reader can find more information on the CIR proof in Appendix C.1.10. In the formula, the autocorrelation characterizes the impairment of the aggregate phase noise due to time correlation. As part of the WSS definition, the autocorrelation lag is only dependent on the difference between two time instants  $u$  and  $v$ . For a more direct computation of the CIR, the autocorrelation can also be expressed using the frequency domain representation as:

$$\varepsilon_{\Phi}(u, v) = \int_{\mathbb{R}} |H^\Phi(f)|^2 e^{j2\pi f(u-v)} \, df , \quad (3.4.4)$$

which is dependent on the transfer function of the aggregate phase noise mask filter.

As an example, the transfer function of the aggregate phase noise mask filter can

be approximated as a piecewise function as follows:

$$|H^\Phi(f)|^2 = \frac{1}{2} \cdot \begin{cases} K_4, & 0 \text{ Hz} \leq |f| \leq 1 \cdot 10^2 \text{ Hz} \\ K_3/|f|^3, & 1 \cdot 10^2 \text{ Hz} \leq |f| \leq 1 \cdot 10^3 \text{ Hz} \\ K_2/|f|^2, & 1 \cdot 10^3 \text{ Hz} \leq |f| \leq 1 \cdot 10^5 \text{ Hz} \\ K_1/|f|, & 1 \cdot 10^5 \text{ Hz} \leq |f| \leq 1 \cdot 10^7 \text{ Hz} \\ K_0, & 1 \cdot 10^7 \text{ Hz} \leq |f| \leq 5 \cdot 10^7 \text{ Hz} \\ 0, & \text{else} \end{cases}, \quad (3.4.5)$$

where the approximated phase noise levels are based on the DVB-S2X single-sided characteristic of Fig. 2-14 are  $K_4 = 5 \cdot 10^{-3}$ ,  $K_3 = 5 \cdot 10^3 \text{ Hz}^3$ ,  $K_2 = 5 \cdot 10^0 \text{ Hz}^2$ ,  $K_1 = 5 \cdot 10^{-5} \text{ Hz}$  and  $K_0 = 5 \cdot 10^{-12}$ . The front factor  $1/2$  accounts for the fact that the double-sided phase noise mask is defined as half of the single-sided phase noise mask [52]. Moreover,  $f = 10^2 \text{ Hz}$  is assumed to be the low cut-off frequency of the locked oscillator [114]. The levels are neglected beyond the last data point  $f = 5 \cdot 10^7 \text{ Hz}$ . The frequency powers  $f^{-3}$ ,  $f^{-2}$ ,  $f^{-1}$ , and  $f^0$  are the so-called power-law spectra of the phase noise [115]. They correspond to flicker frequency noise, white frequency noise, the flicker phase noise, and white phase noise, respectively. The expression (3.4.5) leads to the aggregate phase noise autocorrelation depicted in Fig. 3-15. The calculation of (3.4.4) can be performed by decomposing the expression as a sum of integrals where each integral corresponds to a given power-law spectrum.

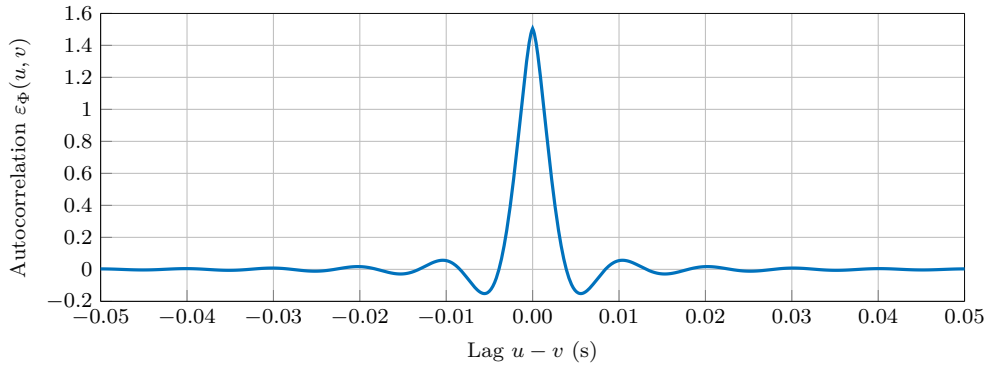


Figure 3-15: Typical aggregate phase noise autocorrelation

In this CIR analysis, there is a subtle difference in the study of the oscillator noise with respect to the work of [C3]. Indeed, the latter work assumed a normalized useful information power as done in the state-of-the-art papers based on the EVM method [84]. However, a more rigorous approach is to use the general CIR formulation in Definition 2. This leads to a useful information power dependent on the phase noise statistic in the same fashion as multiplicative impairments presented in Section 2.1.3. Not only is this definition preferable, since the useful power information accounts for the variations in the phase noise statistics, but it in fact leads to more simplifications in the CIR expression. Indeed, even though the calculations are quite extensive,

especially with the covariance calculation provided in Appendix C.5, common factors present in the useful information power and interference power cancel out. The simplifications also result in the independence with respect to the modulation.

To gain further insights on the CIR behavior, two subcases of Formula 6 are exposed. One notable subcase bringing further insights is the white phase noise. Indeed, this means that the transfer function and impulse response of the aggregate phase noise can be expressed as:

$$H^\Phi(f) = \sqrt{\varepsilon_{\Phi, \text{tot}}} , \quad (3.4.6a)$$

$$h^\Phi(t) = \sqrt{\varepsilon_{\Phi, \text{tot}}} \cdot \delta(t) , \quad (3.4.6b)$$

which leads to the following phase noise mask autocorrelation expression:

$$\varepsilon_\Phi(u, v) = \begin{cases} \varepsilon_{\Phi, \text{tot}}, & \text{if } u = v \\ 0, & \text{else} \end{cases} . \quad (3.4.7)$$

The oscillator noise CIR Formula 6 can then be simplified as:

$$\left(\frac{C}{I}\right)_{\text{ON}}^* (\alpha, T_s, h^\Phi) = \frac{1}{e^{\varepsilon_{\Phi, \text{tot}}} - 1} , \quad (3.4.8)$$

whose derived interference power matches the expression from [84, 115]. It is the only type of phase noise, which is independent of the symbol rate and solely dependent on the phase noise power. Moreover, this CIR function is strictly decreasing with  $\varepsilon_{\Phi, \text{tot}}$ . The following asymptotes can be observed:

$$\left(\frac{C}{I}\right)_{\text{ON}}^* (\alpha, T_s, h^\Phi) \rightarrow \frac{1}{\varepsilon_{\Phi, \text{tot}}} , \quad \text{as } \varepsilon_{\Phi, \text{tot}} \rightarrow 0 , \quad (3.4.9a)$$

$$\left(\frac{C}{I}\right)_{\text{ON}}^* (\alpha, T_s, h^\Phi) \rightarrow 0 , \quad \text{as } \varepsilon_{\Phi, \text{tot}} \rightarrow +\infty . \quad (3.4.9b)$$

The second subcase concerns the low phase noise power, which not only brings further insights, but facilitates the CIR calculation. Indeed, in the case of low power, Formula 6 leads to the asymptote defined below.

**Formula 7: Oscillator noise asymptote (low power)**

$$\left(\frac{C}{I}\right)_{\text{ON}}^* (\alpha, T_s, h^\Phi) \rightarrow \frac{1}{Q(h^\Phi)} , \quad \text{as } \varepsilon_{\Phi, \text{tot}} \rightarrow 0$$

where the denominator  $Q(h^\Phi)$  can be expressed in different ways:

$$Q(h^\Phi) \stackrel{\text{Definition}}{=} \sum_{(k_1, k_2) \in \mathbb{Z}_{(u, v)}^2} \iint_{(u, v) \in \mathbb{R}^2} h_{\text{SC}}(k_1 T_s - u, \alpha, T_s) h_{\text{SC}}(k_2 T_s - v, \alpha, T_s) \cdot h_{\text{SC}}(u, \alpha, T_s) h_{\text{SC}}(v, \alpha, T_s) \varepsilon_\Phi(u, v) du dv$$



$$\begin{aligned}
& \text{Autocorrelation representation (3.4.4)} \\
& \quad = \sum_{(k_1, k_2) \in \mathbb{Z}_{f, u, v}^2} \iiint_{(f, u, v) \in \mathbb{R}^3} h_{\text{SC}}(k_1 T_s - u, \alpha, T_s) h_{\text{SC}}(k_2 T_s - v, \alpha, T_s) \cdot \\
& \quad \quad h_{\text{SC}}(u, \alpha, T_s) h_{\text{SC}}(v, \alpha, T_s) |H^\Phi(f)|^2 e^{j2\pi f(u-v)} df du dv \\
& \quad = \text{SC frequency representation} \\
& \quad \quad \sum_{(k_1, k_2) \in \mathbb{Z}_{f, f_1, f_2}^2} \iiint_{(f, f_1, f_2) \in \mathbb{R}^3} |H^\Phi(f)|^2 H_{\text{SC}}(f - f_1, \alpha, T_s) H_{\text{SC}}(f + f_2, \alpha, T_s) \\
& \quad \quad H_{\text{SC}}(f_1, \alpha, T_s) H_{\text{SC}}(f_2, \alpha, T_s) e^{j2\pi(f_1 k_1 + f_2 k_2) T_s} df df_1 df_2 \\
& \quad = \text{\textit{T}_s\text{-normalization:}} \\
& \quad \quad \tilde{f} = f T_s; \tilde{f}_1 = f_1 T_s; \tilde{f}_2 = f_2 T_s \\
& \quad \quad \sum_{(k_1, k_2) \in \mathbb{Z}_{\tilde{f}, \tilde{f}_1, \tilde{f}_2}^2} \iiint_{(\tilde{f}, \tilde{f}_1, \tilde{f}_2) \in \mathbb{R}^3} |H^\Phi(\tilde{f}/T_s)|^2 H_{\text{SC}}(\tilde{f} - \tilde{f}_1, \alpha) H_{\text{SC}}(\tilde{f} + \tilde{f}_2, \alpha) \\
& \quad \quad H_{\text{SC}}(\tilde{f}_1, \alpha) H_{\text{SC}}(\tilde{f}_2, \alpha) e^{j2\pi(\tilde{f}_1 k_1 + \tilde{f}_2 k_2)} d\tilde{f} d\tilde{f}_1 d\tilde{f}_2, \quad (3.4.10)
\end{aligned}$$

where the last expression presents the lowest complexity, since the integrands are described by means of finite frequency characteristics. On top of that, the normalization with respect to the symbol period highlights that the CIR dependency on  $T_s$  can be fully described by  $|H^\Phi(\tilde{f}/T_s)|^2$ . Alternatively, the behavior of the symbol rate can be described by  $|H^\Phi(\tilde{f} \cdot R_s)|^2$ . It is also worth noting that the limit  $\varepsilon_{\Phi, \text{tot}} \rightarrow 0$  implies  $|\varepsilon_\Phi(u, v)| \rightarrow 0, \forall (u, v) \in \mathbb{R}^2$ , since Cauchy's inequality for integrals [116] leads to  $|\varepsilon_\Phi(u, v)| \leq \varepsilon_{\Phi, \text{tot}}, \forall (u, v) \in \mathbb{R}^2$ . In fact, in the case of low power, the phase noise behaves exactly like an AG noise (scaled to the signal power). This result can be understood by expanding the multiplying aggregate phase noise factor as follows:  $e^{j\Theta(t)} \rightarrow 1 + j \cdot \Theta(t)$  as  $\Theta(t) \rightarrow 0, \forall t$ . It is worth noting that this expansion was already used by Muschallik [86]. More precisely, the CIR expression matches the CIR of a zero-mean purely imaginary additive noise with variance  $\varepsilon_{\Phi, \text{tot}}$  (after normalization of the symbol power).

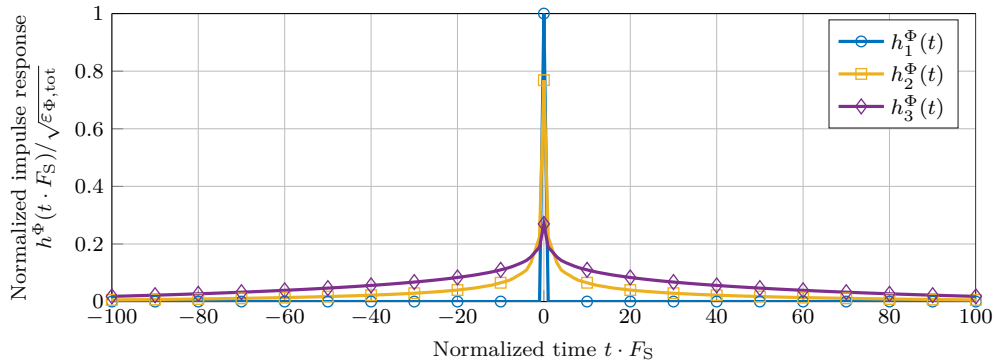


Figure 3-16: Power-laws' impulse responses

Lastly, the oscillator noise CIR is characterized<sup>16</sup> for different power-law spectra and phase noise power. Three phase noise mask filters are simulated with corresponding impulse responses  $h_0^\Phi(t)$ ,  $h_1^\Phi(t)$  and  $h_2^\Phi(t)$  illustrated in Fig. 3-16. They are

<sup>16</sup>The interested reader can refer to [C3] for the analog-to-digital conversion procedure.

designed with transfer function powers of the following form:

$$|H_0^\Phi(f)|^2 \approx K_0, \quad |f| \leq \frac{F_S}{2} \quad (3.4.11a)$$

$$|H_1^\Phi(f)|^2 \approx \frac{K_1}{|f|}, \quad |f| \leq \frac{F_S}{2} \quad (3.4.11b)$$

$$|H_2^\Phi(f)|^2 \approx \frac{K_2}{|f|^2}, \quad |f| \leq \frac{F_S}{2} \quad (3.4.11c)$$

where a reference frequency for the mask is taken arbitrarily as  $F_S/2$ , which is convenient for numerical simulations. To make the dependency on the symbol rate explicit, the expressions (3.4.11a), (3.4.11b), and (3.4.11c) can be reformulated using the  $R_s$ -normalization as:

$$|H_0^\Phi(\tilde{f} \cdot R_s)|^2 \approx K_0, \quad |\tilde{f}| \leq \frac{N_{S/s}}{2} \quad (3.4.12a)$$

$$|H_1^\Phi(\tilde{f} \cdot R_s)|^2 \approx \frac{K'_1}{|\tilde{f}|} \cdot N_{S/s}, \quad |\tilde{f}| \leq \frac{N_{S/s}}{2} \quad (3.4.12b)$$

$$|H_2^\Phi(\tilde{f} \cdot R_s)|^2 \approx \frac{K'_2}{|\tilde{f}|^2} \cdot N_{S/s}^2, \quad |\tilde{f}| \leq \frac{N_{S/s}}{2} \quad (3.4.12c)$$

where  $K'_1 = K_1 \cdot F_S$  and  $K'_2 = K_2 \cdot F_S^2$ . The number of samples per symbol, denoted by  $N_{S/s}$ , is the parameter characterizing the behavior of  $R_s$  with respect to the phase noise mask. Moreover, the filter energies of the aggregate phase noise masks are denoted by  $\varepsilon_{\Phi 0, \text{tot}}$ ,  $\varepsilon_{\Phi 1, \text{tot}}$  and  $\varepsilon_{\Phi 2, \text{tot}}$ , respectively.

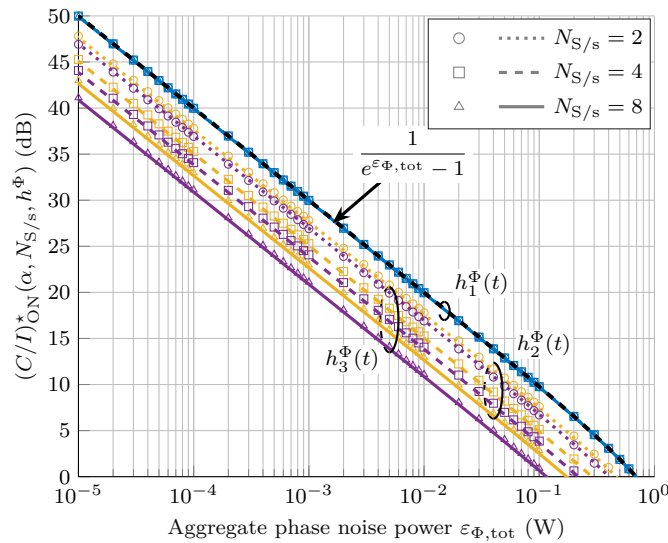


Figure 3-17: Oscillator noise CIR

The CIR is depicted in Fig. 3-17 as a function of the energy of each phase noise

mask filter<sup>17</sup> and number of samples per symbol. Firstly, the white phase noise simulated by  $h_1^\Phi(t)$  perfectly matches the theoretical formula (3.4.8),  $\forall N_{S/s}$ . On the other hand, the increase of degree in power-law spectra decreases the CIR for a given  $N_{S/s}$ . Besides that, the CIR of  $h_3^\Phi(t)$  and  $h_2^\Phi(t)$  is decreasing with increasing  $N_{S/s}$  for a given phase noise power. This can be understood from asymptote denominator expression (3.4.10) and normalized transfer function powers (3.4.12b) and (3.4.12c), which shows that the CIR of  $h_3^\Phi(t)$  and  $h_2^\Phi(t)$  is decreasing by a factor  $N_{S/s}$  and  $N_{S/s}^2$ , respectively. In other words, increasing the symbol rate for a given (non-white) phase noise mask leads to an increase in CIR. The degree of the increase depends on the degree of the power-law spectrum. This implies that increasing the symbol rates of a system reduces the effect of all power-law spectra of the oscillator noise with the exception of the white phase noise components. Moreover, the asymptote Formula 7 has a remarkable accuracy of 97.9 % for CIRs above 10 dB and an accuracy of 87.8 % for CIRs above 5 dB,  $\forall N_{S/s}$ ,  $\forall h^\Phi(t)$ . Finally, numerical simulations based on QPSK and 16-APSK modulations confirm the independence of the modulation schemes<sup>18</sup> as expressed by the theoretical Formula 6. They also suggest that the CIR is independent of the roll-off.

#### Main findings on oscillator noise

To finalize this section, we can draw the following conclusions:

- Formula 6 can be used to characterize the oscillator noise in LTI systems.
- Low-complexity Formula 7 can be used with 97.9 % accuracy for CIRs above 10 dB. It is the key to understanding the connection between phase noise mask and symbol rate, and their respective impact on the CIR.

### 3.5 Summary and future works

In this chapter, *novel* and practical CIR formulas have been derived for four critical impairments: Waveform imperfections (Section 3.1), filter distortions (Section 3.2), amplifier distortions (Section 3.3), and oscillator noise (Section 3.4). A summary of the formulas is presented in Table 3.2 with some of the key inputs and requirements for their application. The presented set of formulas constitutes an important basis for satellite engineers to assess the performance of present and future satellite links. Most importantly, these low-complexity formulas are based on rigorous mathematical models with explicit assumptions as opposed to currently used empirical formulas and estimates based on time-consuming and cumbersome simulations. Detailed proofs have also been provided for each type of impairment for two main reasons. On the one hand, it enables an in-depth understanding of the dependencies and independencies as well as how the key impairment parameters are formed. On the other hand, it

<sup>17</sup>In that case, it is not required to define the power levels  $K_0$ ,  $K_1$  and  $K_2$ .

<sup>18</sup>As illustrated with the multiplicative impairment in Fig. 2-3b, the instantaneous CIR (symbol-level) is dependent on the modulation scheme, but not the generalized CIR (signal-level).

facilitates the reproducibility of the results and thus, facilitates future research and improvements of the presented formulas. Furthermore, the main mathematical tools used for the derivations of each impairment are provided to ease future work within the presented framework.

Although all presented results have been verified through numerical simulations, a logical next step of this work is to verify them through experiment. Moreover, numerous extensions of the characterization are possible. A few examples are presented below:

- In the context of waveform imperfections, a study of future candidate satellite waveforms such as the 5G new radio waveform based on OFDM [117] seem of interest to understand the new trade-offs introduced by the standard.
- In the context of the amplifier distortions, a study of the optimal decision instant in single-carrier and multi-carrier modes seems necessary to understand possible deviations as demonstrated in the presence of filter distortions.
- In the context of the oscillator noise, a study of the CIR with respect to candidate phase noise masks for higher frequency bands seems relevant to understand the impact of oscillators in future systems.

Table 3.2: Summary of CIR formulas

Formula	System	Main impairment model inputs	Main requirement
<b>Waveform imperfections:</b>			
1	Fig. 2-10	Waveform parameters	SC pulse shaping
<b>Filter distortions:</b>			
2	Fig. 2-10	Channel filter poles and zeros	-
3	Fig. 2-10	Channel filter gain and group delay	Distortions linearity
<b>Amplifier distortions:</b>			
4	Fig. 2-12	HPA polynomial coefficients	Single-carrier mode
5	Fig. 3-11	HPA polynomial coefficients	Multi-carrier mode
<b>Oscillator noise:</b>			
6	Fig. 3-14	Phase noise mask	-
7	Fig. 3-14	Phase noise mask	Low phase noise power

# 4 | Applications

## Contents

4.1	Link budget refinement . . . . .	71
4.2	Link budget optimization . . . . .	78
4.3	Summary and future works . . . . .	86

In this chapter, examples of key applications of the derived CIR formulas are exposed. As a first step, different approaches are presented to further refine the link budget in a contemporary HTS scenario. Then, the focus is set on link budget optimization. In this context, the feasibility and gain of real-time DCA optimization are demonstrated for future UHTS scenarios.

## 4.1 Link budget refinement

### 4.1.1 Scenario

As support for the analysis, the link budget report generated by the Newtec tool [65] and specified in the DVB-S2X standard [52] is considered. The lists of link budget input and output data in clear sky conditions are available in Appendix D. The scenario corresponds to a high-speed link implemented over a realistic Ka-band link<sup>1</sup> and with realistic ground infrastructure. This contemporary HTS scenario is illustrated in Fig. 4-1. In particular, a forward link in two-carrier mode is considered. The carrier under study is configured with a symbol rate  $R_s^{(1)} = 36.571$  Mbauds, roll-off  $\alpha^{(1)} = 0.05$  as well as the modulation and coding (MODCOD) 32-APSK 9/10. Based on the link budget calculations, the system is able to provide a net bit rate of 159.338 Mbits/s to the user located in Beirut in clear sky conditions.

The present mathematical framework reveals essentially two main issues in such typical link budget calculations:

- 1) All impairments are implicitly assumed to be AG. Consequently, they are all combined using the decomposition rule (Corollary 1).
- 2) Not all impairments relevant to satellite communications systems are taken into account.

---

<sup>1</sup>Al Yah 2, previously named YahSat 1B, is a Saudi Arabian HTS, which is configured with 61 narrow spotbeams. The satellite provides – among others – television and high-speed Internet services in the Middle East, Africa, Central and South West Asia. Its coverage especially includes rural and remote areas [118, 119].

Thus, these two issues are tackled in the following using the material of this thesis.

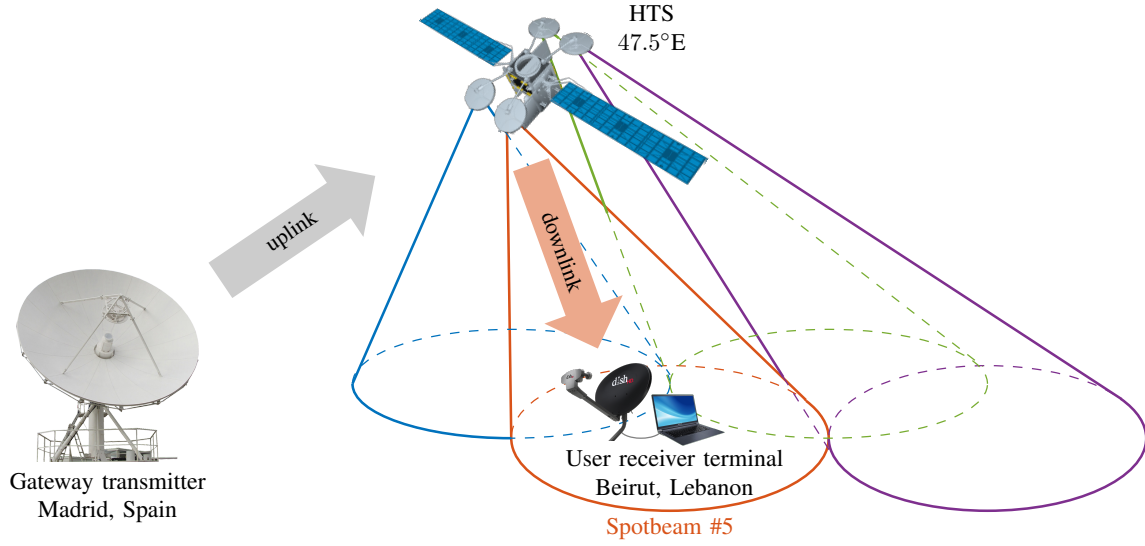


Figure 4-1: Contemporary HTS Ka-band scenario

### 4.1.2 Link budget enhancement

#### Amplifier distortions

To this date, the amplifier distortions are still modeled as an AG impairment<sup>2</sup>, which does not take the impact of filters into account. Based on this work, Formula 5 can be used to render the full complexity of this impairment and thus, further enhance the accuracy of the link budget calculations. As a matter of fact, amplifier distortions are neither additive nor Gaussian. Furthermore, the proper modeling of amplifier distortions requires the memory of the HPA and filters to be included. Since the parameters of the carrier under study are known, four groups of parameters must be determined to apply Formula 5: The polynomial coefficients, the modulation coefficients, the multicarrier parameters, and the filter parameters. The step-by-step procedure goes as follows.

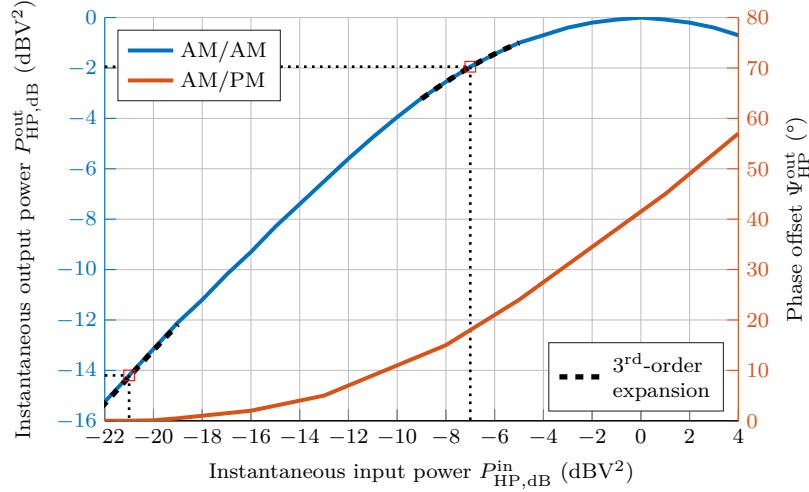
As a first step, the characteristics of the conventional Ka-band TWTA specified by the DVB-S2X standard are used as support for the derivation of the polynomial coefficients. The corresponding characteristics are illustrated in Fig. 4-2a. To be more specific, the CIR relies on the quantities  $|\gamma_1|$ ,  $|\gamma_3|$ , and  $\arg(\gamma_1^* \gamma_3)$ , which are directly dependent on the polynomial coefficients  $\gamma_1$  and  $\gamma_3$ . They are the fingerprint of the HPA nonlinearities in the CIR. These quantities can be directly extracted from the AM/AM characteristic, by expanding the AM/AM function<sup>3</sup> at the input power of interest as illustrated in Fig. 4-2a. Mathematically, it means identifying the

<sup>2</sup>This AG CIR is sometimes referred to as carrier-to-spectral regrowth power ratio.

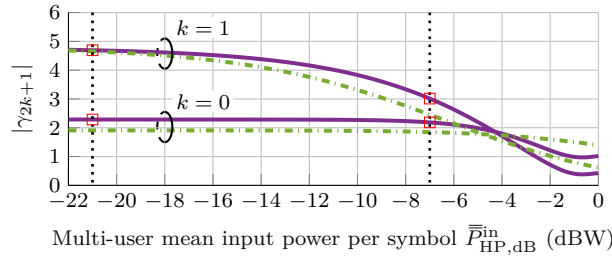
<sup>3</sup>If only data points are available, this mathematical function can for instance be generated via polynomial interpolation. In this scenario, a 9<sup>th</sup>-degree polynomial is used.

coefficients of the following expansion:

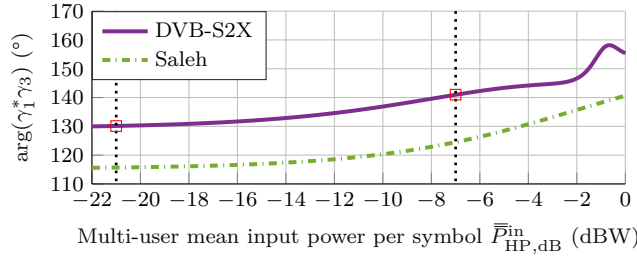
$$\begin{aligned}
 |\mathcal{Y}(t)|^2 &\stackrel{\text{Polynomial representation (3.3.2)}}{\approx} \left| \gamma_1 \cdot \mathcal{X}(t) + \gamma_3 \cdot \mathcal{X}(t) \cdot |\mathcal{X}(t)|^2 \right|^2 \\
 &\approx |\gamma_1|^2 \cdot |\mathcal{X}(t)|^2 + |\gamma_3|^2 \cdot |\mathcal{X}(t)|^6 \\
 &\quad + 2 \cdot |\gamma_1| \cdot |\gamma_3| \cdot \cos(\arg(\gamma_1^* \gamma_3)) \cdot |\mathcal{X}(t)|^4, \text{ as } |\mathcal{X}(t)|^2 \approx \bar{P}_{\text{HP}}^{\text{in}}. \quad (4.1.1)
 \end{aligned}$$



(a) Normalized DVB-S2X HPA characteristics [52]



(b) Modulus of the polynomial coefficients



(c) Relative angle between the polynomial coefficients

Figure 4-2: Extraction of the polynomial coefficients characteristics

Since the spotbeam output back-off (OBO) is specified as 14.3 dB, this implies that the desired quantities can be computed using the corresponding multi-user mean

power per symbol at HPA input<sup>4</sup>  $\bar{P}_{\text{HP,dB}}^{\text{in}} = -21$  dBW i.e.  $\bar{P}_{\text{HP}}^{\text{in}} = 10^{\frac{-21}{10}} \approx 7.943 \cdot 10^{-3}$  W. This leads<sup>5</sup> to  $|\gamma_1| \approx 2.287$ ,  $|\gamma_3| \approx 4.692$  and  $\arg(\gamma_1^* \gamma_3) \approx 130.1^\circ$ . It is worth noting that the dependency on  $\arg(\gamma_1^* \gamma_3) = \arg(\gamma_3) - \arg(\gamma_1)$  means that only the relative angle of  $\gamma_3$  with respect to  $\gamma_1$  is necessary and not the absolute angles. The complete characteristics of the polynomial coefficients moduli and relative angle are given in Fig. 4-2b and Fig. 4-2c, respectively. As an element of comparison, the characteristics of the Saleh coefficients previously exposed in Section 2.2.3 are provided as well.

As a second step, the modulation coefficients can be derived as follows. Since the considered coding rate is 9/10, the corresponding optimized inner and outer ring ratios of the 32-APSK modulation are  $v_1 = 2.53$  and  $v_2 = 4.30$  [52]. Based on the ring ratios as well as the power moments presented in Appendix B.4, the following 32-APSK modulation coefficients can be computed:  $r_1^{(1)} = 1$ ,  $r_2^{(1)} \approx 1.3457$  and  $r_3^{(1)} \approx 1.9987$ .

As a third step, the multicarrier parameters must be defined: the power sharing between the two carriers and the bandwidth parameters of the second carrier. Since the link budget tool does not account for these parameters, an equal power sharing is considered with  $(\lambda_{\text{HP}}^{(1)}, \lambda_{\text{HP}}^{(2)}) = (0.5, 0.5)$ . Furthermore, the same symbol rate and roll-off are considered for the second carrier, i.e.  $R_s^{(2)} = 36.571$  Mbauds and  $\alpha^{(2)} = 0.05$ . Since the guardband between the carriers is not specified, a theoretical value of 0 Hz is considered.

As a final step, the filter parameters must be determined. However, link budget tools are still not able to take into account filter characteristics. For the sake of interpretation of the result, it is considered that the system is free of filter distortions. This implies that the pre-HPA and post-HPA system impulse responses  $\tilde{h}^{\rightarrow(1)}(t) = h^{\leftarrow(1)}(t) = \tilde{h}^{\rightarrow(2)}(t) = h_{\text{SC}}(t, 0.05, 2.7344 \cdot 10^{-8})$ , where  $T_s^{(1)} = T_s^{(2)} \approx 2.7344 \cdot 10^{-8}$  s.

In the end, the modulation coefficients, multicarrier parameters, and filter parameters enable to compute the two-carrier useful information power coefficients  $C_{1,1}^{(1)}$ ,  $C_{2,1}^{(1)}$ ,  $C_{3,1}^{(1)}$ ,  $C_{2,2}^{(1,2)}$ ,  $C_{3,2}^{(1,2)}$  and  $C_{3,3}^{(1,2)}$  as well as the two-carrier interference power coefficients  $I_{1,1}^{(1)}$ ,  $I_{2,1}^{(1)}$ ,  $I_{3,1}^{(1)}$ ,  $I_{2,2}^{(1,2)}$ ,  $I_{3,2}^{(1,2)}$  and  $I_{3,3}^{(1,2)}$ . Using all the derived parameters, the overall useful information power  $C_{\text{AD}}^{(1)}$  and impairment power  $I_{\text{AD}}^{(1)}$  can be derived from (3.3.12) and (3.3.15), respectively. Consequently, Formula 5 results in the following multi-carrier amplifier distortions CIR for the user located in Beirut:

$$\left(\frac{C}{I}\right)_{\text{AD,dB}}^{(1)*}(0.05, 2.7344 \cdot 10^{-8}, 0, 0.5, 7.943 \cdot 10^{-3}) \approx 38.06 \text{ dB}, \quad (4.1.2)$$

which is above the typical 30 dB lowerbound desired for the specifications [52]. On top of that, Formula 5 achieves 99.2 % accuracy<sup>6</sup> when comparing (4.1.2) with respect

<sup>4</sup>It is reminded that power values are expressed relatively to a normalized unit input power at saturation.

<sup>5</sup>Since  $\arg(\gamma_1^* \gamma_3) \approx \pm 142.9^\circ$  by inverting  $\cos(\arg(\gamma_1^* \gamma_3)) \approx -0.798$ , the sign of the angle can be retrieved by matching with the AM/PM curve.

<sup>6</sup>At this stage, the accuracy comparison can only be done rigorously with respect to numerical simulations (i.e., the true CIR value), since the Newtec link budget tool is based on slightly different



to the numerical simulations, which includes the complete HPA characteristic.

Since the useful information and interference power coefficients are already computed, it is worth noting that the formula can easily be updated with a different MODCOD, power back-off, or power ratio. For instance, if the operating point of the HPA is chosen closer to saturation with  $\bar{P}_{\text{HP,dB}}^{\text{in}} = -7$  dBW. This leads to  $\bar{P}_{\text{HP}}^{\text{in}} = 10^{\frac{-7}{10}} \approx 1.995 \cdot 10^{-1}$  W,  $|\gamma_1| \approx 2.186$ ,  $|\gamma_3| \approx 3.013$  and  $\arg(\gamma_1^* \gamma_3) \approx 141.0^\circ$ . As a result, the CIR can be updated with little effort into:

$$\left(\frac{C}{I}\right)_{\text{AD,dB}}^{(1)\star} (0.05, 2.7344 \cdot 10^{-8}, 0, 0.5, 1.995 \cdot 10^{-1}) \approx 10.61 \text{ dB} . \quad (4.1.3)$$

Nonetheless, an almost complete update of the expression would ineluctably be required if at least one of the multicarrier parameters (symbol rate, roll-off, or number of carriers) or filter parameters (distortions characteristic) was to be modified. For example, considering the post-HPA filter distortions of the OMUX requires a redefinition of the user 1 post-HPA filter impulse response as  $h^{\leftarrow(1)}(t) = \int_{\mathbb{R}} H_{\text{SC}}(\tilde{f}, \alpha^{(1)}) \cdot H_{\text{OM}}((\tilde{f} + \tilde{f}_{\Delta}^{(1)})/T_s^{(1)}) \cdot e^{j2\pi\tilde{f}t} d\tilde{f}$ , which leads to a redefinition of all useful information and impairment power coefficients.

Since the CIR of the multi-user amplifier distortions has been derived in the NTI system illustrated in Fig. 3-11, it is this system model and the generalized CIR (Definition 2) that impose the rules of CIRs combination. For instance, the power defined at decision instant of post-HPA uncorrelated AG impairments  $I', I'', \dots$  can still be combined in an additive manner as follows:

$$\left(\frac{C}{I}\right)^{(1)\star} = \left(\frac{C_{\text{AD}}^{(1)}}{I_{\text{AD}}^{(1)} + I' + I'' + \dots}\right)^{\star} . \quad (4.1.4)$$

However, the expression relies on the optimization of the decision instant offset  $\tau^*$ , which is one of the main challenges in considering more general and more accurate models.

Finally, it is worth noting that this particular link budget takes into account the amplifier distortions CIR not only from the HTS, but also from the gateway transmitter. As, in this scenario, the gateway transmitter operates in single-carrier mode, the CIR of single-carrier amplifier distortions (Formula 4) should be preferred as a result<sup>7</sup>.

---

assumptions (it uses for instance a built-in default HPA characteristic) as well as empirical modeling. However, it suggests a CIR discrepancy in the order of dBs.

<sup>7</sup>The combination of CIRs of amplifier distortions has not been studied in the present mathematical framework and constitutes one of the possible extensions of this work.

### 4.1.3 Link budget complements

#### Filter distortions

Since link budget tools such as the one from Newtec do not take filter distortions into account, the DVB-S2X standard provides further information regarding filter distortions. For instance, the average gain slope related to the DTH receiver cable and LNB is measured and specified as 2 dB over 500 MHz. From this information, the CIR corresponding to the receiver filter distortions can be derived. As a basis for the calculation, the carrier parameters  $\alpha = 0.05$  and  $R_s = 36.571$  Mbauds are used once more. The step-by-step calculation goes as follows.

As a first step, the gain slope is computed:  $g_1 = 4 \cdot 10^{-3}$  dB/MHz. As a second step, the 1<sup>st</sup>- order gain distortions coefficient is computed:  $x_1 = g_1 \cdot R_s = 1.463 \cdot 10^{-1}$  dB/MHz · Mbauds. Finally, the CIR can directly be determined using either Fig. 3-3 or Formula 3. In the latter case, the CIR calculation can be performed *by hand* as follows:

$$\begin{aligned} \left(\frac{C}{I}\right)_{\text{FD,dB}}^* (0.05, 1.36 \cdot 10^{-1}, 0) &= -10 \cdot \log_{10} \left( (\xi \cdot 1.463 \cdot 10^{-1})^2 \cdot P_1(0.05) \right) \\ &\approx -10 \cdot \log_{10} \left( (0.11513 \cdot 1.463 \cdot 10^{-1})^2 \cdot 0.07720 \right) \\ &\approx 46.60 \text{ dB} , \end{aligned} \tag{4.1.5}$$

where  $P_1(0.05) \approx 0.07720$  is provided in Table 3.1 and by definition  $\xi = \ln(10)/20 \approx 0.11513$ . Since the CIR is above 20 dB, the characterization from Section 3.2.2 also guarantees that the accuracy of this asymptotic formula lies beyond 99.5 % with respect to the general filter distortions CIR (Formula 2). Although this CIR does not account for all filter distortions in the system<sup>8</sup>, it is a key and convenient approach to evaluating the impact a single component (or group of components) can have on the system.

When performing more precise link budget calculations and in the case of strong filter distortions (typically with CIR lower than 10 dB), Formula 2 should be preferred over Formula 3 to obtain a higher level of accuracy. However, the expression is more general. Its application comes at the cost of more complexity.

#### Oscillator noise

Similar to the filter distortions, Formula 6 can be used to evaluate the overall impact of the oscillator noise on the system. Nevertheless, it should be kept in mind that due to the multiplicative nature of this impairment, the direct inclusion of this CIR in the link budget is not trivial and requires further investigations.

Fortunately, it has been highlighted that the oscillator noise behaves closely to an additive impairment (typically for CIR above 10 dB with 97.9 % accuracy). Thus, the asymptote expression of Formula 7 can be included in the link budget using the

<sup>8</sup>To evaluate the overall impact of all components, the sum of the gain slopes and group delay slopes must be used to compute  $x_1$  and  $y_1$ , respectively.

decomposition rule under certain conditions<sup>9</sup>. In the end, it appears as a promising approach to include multiplicative impairments in link budget calculations.

### Waveform imperfections

The link budget tools such as the one from Newtec do not take waveform imperfections into account. However, this impairment is ubiquitous in any practical system involving SC shaping. Indeed, to characterize mathematically each impairment in Chapter 3, the waveform imperfections parameters are in fact tuned such as to be dominated by the impairment under study on the range of observation. To give an example, a graph of gain slope distortions is simulated (as performed in Section 3.2.2) and illustrated in Fig. 4-3 as a function of the SC one-sided span  $S$ . The roll-off is again considered as  $\alpha = 0.05$  and the number of samples per symbol arbitrarily as  $N_{S/s} = 4$ . As a point of comparison, the decomposition rule is applied to the waveform

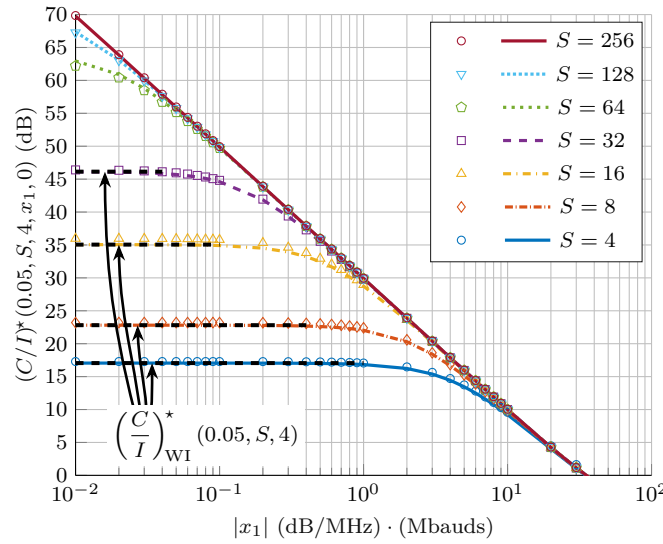


Figure 4-3: Waveform imperfections impact on the total CIR

imperfections CIR (Formula 1) and filter distortions CIR (Formula 2) to approximate the total<sup>10</sup> CIR as follows:

$$\left(\frac{C}{I}\right)^{\star-1}(\alpha, S, N_{S/s}, x_1, y_1) \approx \left(\frac{C}{I}\right)^{\star-1}_{\text{WI}}(\alpha, S, N_{S/s}) + \left(\frac{C}{I}\right)^{\star-1}_{\text{FD}}(\alpha, x_1, y_1). \quad (4.1.6)$$

Indeed, it can be observed that the total CIR behaves closely to the decomposition rule<sup>11</sup>. For CIRs above 20 dB, the decomposition rule reaches a minimum of 98.11 % accuracy with respect to the simulated data points. To derive the optimized waveform imperfections parameters, the following procedure is proposed.

<sup>9</sup>Given that the oscillator noise CIR has been derived in an LTI system, it means that this approximation holds only when the HPA is operated in the linear region.

<sup>10</sup>In this example, it refers to the realistic time-limited and sampled filter distortions CIR.

<sup>11</sup>However, the corresponding mathematical decomposition is non-trivial and relies on evaluating the convergence terms of the Riemann sum contained in the total CIR.

Firstly, a target link budget CIR link budget is chosen. Here, the value  $(C/I)_{\text{dB}} = 20.46$  dB of Table D.2 is considered as a reference. Secondly, minimum accuracy on the target CIR is chosen such as 99 %. Based on the principle of impairment domination exposed in Section 2.1.4, a CIR of at least 33.63 dB is required to guarantee a minimum of 99 % of accuracy. This leads to a minimum one-sided span of  $S = 16$ , which corresponds to  $(C/I)_{\text{WI,dB}}^*(0.05, 16, 4) \approx 35.05$  dB. It results in a total CIR with waveform imperfections of  $(C/I)_{\text{dB}} = 20.31$  dB reaching 99.3 % accuracy of the target value and remaining above the specified minimum accuracy.

In the end, it is crucial to understand and *control* the impact that ubiquitous impairments such as the waveform imperfections have on the total CIR to obtain even more accurate link budget calculations. On top of that, optimizing the waveform imperfections parameters can enable to further optimize computational resources of the UHTS OBP and thus, save on-board power consumption.

### Main findings on link budget refinement

To finalize this section, we can draw the following conclusions:

- The accuracy of the amplifier distortions CIR in contemporary link budgets can be enhanced using Formulas 4 and 5. The formulas also define the rules on how to combine other additive impairments.
- The filter distortions CIR (Formulas 2 and 3) and oscillator noise CIR (Formulas 6 and 7) can be used as link budget complements.
- The waveform imperfections parameters can be optimized such as to balance system complexity and the CIR impact (Formula 1).

## 4.2 Link budget optimization

### 4.2.1 Problem formulation

In the frame of this thesis, the behavior of different parameters has been explored. In practice, the parameters related to two key resources need to be meticulously optimized. On the one hand, it is paramount to make the best use of the available spectrum and thus, optimize jointly the symbol rate  $R_s^{(i)}$ , roll-off  $\alpha^{(i)}$  and carrier placement  $f_{\Delta}^{(i)}$  of all users  $i \in \{1, 2, \dots, N_u\}$ . On the other hand, the power settings such as the user power ratio  $\lambda_{\text{HP}}^{(i)}$  and the mean power per symbol at the HPA input  $\bar{P}_{\text{HP}}^{\text{in}}$  need to be carefully chosen to achieve the best system performances.

To illustrate an application of the formulas derived in this work, an optimization of frequency resources is proposed<sup>12</sup>. More specifically, the feasibility of real-time DCA optimization in the context of UHTS systems is highlighted. Indeed, DCA brings key benefits. It allows a fully flexible connectivity between uplink and downlink beams,

<sup>12</sup>For the sake of simplicity and without loss of generality, it is assumed that in this scenario the HPA is operated in the linear region and that the power is equally shared between the carriers.

removes the need for a centralized gateway, and can achieve higher capacity gains as demonstrated in terrestrial communications [120]. On top of that, it prevents from increasing the processing power on-board the satellite, which is a major drawback of alternative strategies such as beam-hopping (physical layer) or flexible routing protocols (higher layer). In fact, real-time DCA optimization is of high interest for mobility applications. It is especially well-suited for airborne services such as in-flight entertainment (IFE), where new aircraft appear and others disappear regularly. This phenomenon is even amplified in UHTS communications systems where the width of spotbeams gets narrower.

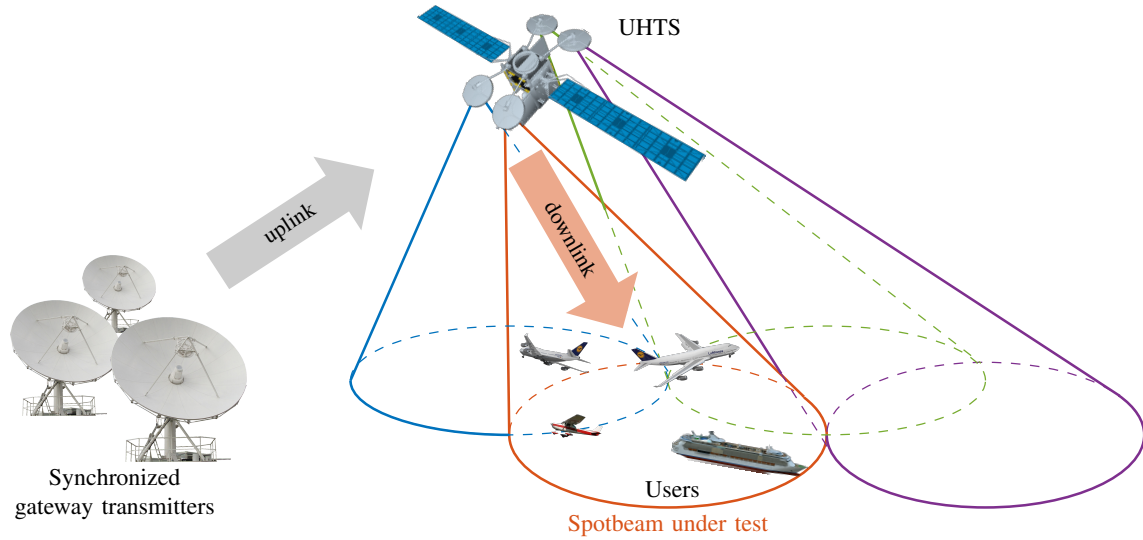


Figure 4-4: Future UHTS DCA scenario

The considered scenario is depicted in Fig. 4-4. As detailed in the introduction, filter distortions are expected to play a critical role in the UHTS link budget, since wideband multicarrier operations tend to be preferred for flexibility, spectral efficiency, and mass reasons. As such, the realistic wideband OMUX shown in Fig. 2-11 is considered to model CIR variations over the frequency. The corresponding CIR graph obtained by applying Formula 2 is illustrated in Fig. 4-5. The imperfections of a realistic characteristic can especially be noticed as opposed to the ideal case presented in Fig. 3-8. In the end, the link budget corresponding to this scenario can be simplified as follows:

$$\left(\frac{C}{I}\right)^{\star-1}(\alpha^{(i)}, R_s^{(i)}, f_{\Delta}^{(i,v)}) = \left(\frac{C}{I}\right)_{\text{FD}}^{\star-1}(\alpha^{(i)}, R_s^{(i)}, f_{\Delta}^{(i,v)}) + \left(\frac{C}{I}\right)_{\text{AG}}^{\star-1}, \quad (4.2.1)$$

where the total CIR is decomposed<sup>13</sup> into the filter distortions CIR and an arbitrary CIR. The subscript AG refers to all the other impairments that are considered AG.

Based on this link budget expression, the DCA optimization problem can be

<sup>13</sup>In this case, the decomposition rule can be applied, since the remaining CIR is considered AG. However, the decision instant offset must be optimized on both CIRs jointly.

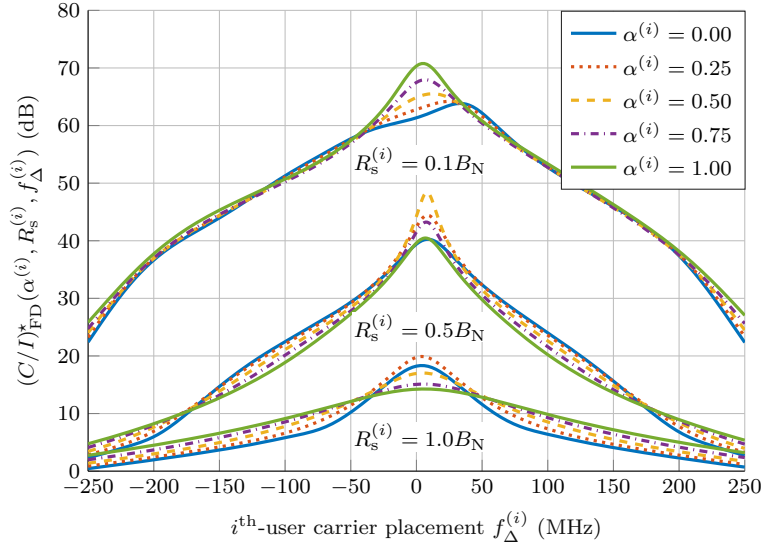


Figure 4-5: Filter distortions CIR characteristic

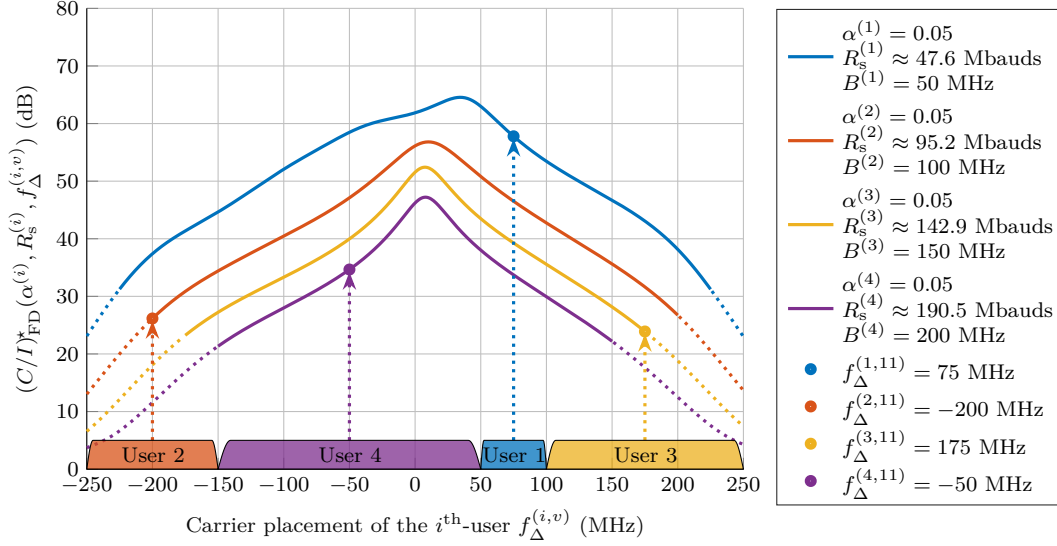
formulated. Different optimization approaches can be considered: sum-rate maximization, CIR maximization based on user priority, or CIR maximization based on user fairness. For the sake of illustration, the latter approach is considered. Thus, the DCA optimization problem can be reduced to a max-min optimization problem:

$$\mathcal{P} : \max_{1 \leq v \leq V} \left\{ \min_{1 \leq i \leq N_u} \left\{ \left( \frac{C}{I} \right)^* \left( \alpha^{(i)}, R_s^{(i)}, f_{\Delta}^{(i,v)} \right) \right\} \right\} \quad (4.2.2)$$

where  $v$  and  $V$  designate the index of a given sequence<sup>14</sup> of users' carriers and the number of possible sequences, respectively. Therefore, the DCA optimization consists in finding the allocation  $v^*$  that maximizes the minimum CIR across all carriers. Put in another way, it focuses on minimizing the worst-case of filter distortions. To eliminate unnecessary complexity, it is assumed that the carriers are non-overlapping and that the sum of the users' bandwidth matches the OMUX nominal bandwidth, i.e.  $\sum_{i=1}^{N_u} B^{(i)} = B_N$ . Thus, the search space is reduced in the worst case to  $V \cdot N_u$  CIR computations. Furthermore, the advantages of the max-min problem formulation have been especially highlighted in the context of cellular radio systems [121, 122]. It is worth noting that most resource allocation problems such as this one are NP-hard [123].

To better picture how the carrier allocation is performed, an example is provided in the case  $N_u = 4$ . All possible sequences of users' carriers are listed in Table 4.1. A configuration is chosen such that each user has the same roll-off  $\alpha^{(i)} = 0.05$  and a different symbol rate  $R_s^{(i)}$ . The corresponding allocation for sequence  $v = 11$  is depicted in Fig. 4-6. When focusing solely on filter distortions, the CIRs of users 1, 2, 3 and 4 are 57.79 dB, 26.16 dB, 23.90 dB and 34.66 dB, respectively. This especially emphasizes the wide range of possible CIR values. In this configuration, the minimum

<sup>14</sup>By convention, the sequences are indicated in increasing order of frequency.

Figure 4-6: Example of carriers allocation ( $N_u = 4$ ;  $v = 11$ )

filter distortions CIR is reached by user 3. After optimization, the best allocation<sup>15</sup> corresponds to  $v = 4$  with a minimum CIR of 26.74 dB.

## 4.2.2 Methodology of performance evaluation

### Filter distortions representations

In the context of filter distortions, two representations have been exposed: The pole-zero representation and the exponential polynomial representation. At the heart of the DCA lies the trade-off between complexity and accuracy of the CIR computation, which precisely depends on the selected representation. On the one hand, the pole-zero representation (related to Formula 2) has the best accuracy, but also the more complexity. On the other hand, the 1<sup>st</sup>-order of filter distortions of the exponential polynomial representation (related to Formula 3) have less accuracy, but have

<sup>15</sup>For simplicity, this first example of optimization assumes that  $(C/I)_{AG}^* \rightarrow +\infty$ .

Table 4.1: List of possible users' sequences ( $N_u = 4$ )

$v$	sequences	$v$	sequences	$v$	sequences	$v$	sequences
1	1-2-3-4	7	2-1-3-4	13	3-1-2-4	19	4-1-2-3
2	1-2-4-3	8	2-1-4-3	14	3-1-4-2	20	4-1-3-2
3	1-3-2-4	9	2-3-1-4	15	3-2-1-4	21	4-2-1-3
4	1-3-4-2	10	2-3-4-1	16	3-2-4-1	22	4-2-3-1
5	1-4-2-3	11	2-4-1-3	17	3-4-1-2	23	4-3-1-2
6	1-4-3-2	12	2-4-3-1	18	3-4-2-1	24	4-3-2-1



the lowest complexity possible. Thus, their performance is compared for the DCA optimization. Both DCA methods are referred to as *pole-zero* and *slope-based*.

### Performance criteria

To evaluate the performance of the proposed DCA methods, four criteria are used. The first performance criterion is the complexity (or allocation speed), which can be decomposed into two elementary complexities:

$$\mathcal{O}(\text{DCA}) \approx \mathcal{O}(\text{Search}) \times \mathcal{O}(\text{CIR}) , \quad (4.2.3)$$

where  $\mathcal{O}(\text{Search})$  and  $\mathcal{O}(\text{CIR})$  represent the complexities of the search algorithm and the CIR computation, respectively. This criterion is of paramount importance, since it determines to which extent real-time DCA optimization can be applied. A naive brute-force search among all possible carrier allocations is in the order of  $\mathcal{O}(N_u \cdot N_u!)$ , which is computationally expensive. By contrast, a smarter approach consists in computing only non-repetitive CIR values, since the placement of a given carrier is sometimes identical across different possible carrier combinations. This latter approach is used in the simulations and leads to a search complexity of  $\mathcal{O}(N_u \cdot 2^{N_u-1})$ . In the example of  $N_u = 4$ , the non-repetitive placements of users' carriers are indicated in Table 4.1 in blue and constitute an acceleration of the DCA by a factor of 3.

The second performance criterion is the allocation optimality. It simply consists in measuring the success rate where the best possible carrier allocation is achieved. Since this criterion is a direct consequence of the CIR accuracy, the accuracy is also given as complementary information.

The third performance criterion is the allocation gain. Thus, the minimum CIR achieved by a DCA optimization method is measured with respect to the minimum CIR achieved through random allocation. Consequently, the allocation gain can be defined as:

$$\mathcal{G}_{\text{dB}} = 10 \cdot \log_{10} \left( \frac{\min_{1 \leq i \leq N_u} \left\{ \left( \frac{C}{I} \right)^* (\alpha^{(i)}, R_s^{(i)}, f_{\Delta}^{(i, v_m^*)}) \right\}}{\min_{1 \leq i \leq N_u} \left\{ \left( \frac{C}{I} \right)^* (\alpha^{(i)}, R_s^{(i)}, f_{\Delta}^{(i, v_r)}) \right\}} \right) , \quad (4.2.4)$$

where  $v_m^*$  and  $v_r$  are the optimized carrier allocation resulting from a given DCA method and the random carrier allocation, respectively.

Last but not least, the fourth performance criterion is a complementary indicator of the DCA capacity increase. The Shannon capacity for AG impairments is used to conveniently estimate the increase of capacity provided by a given DCA method with respect to the capacity of the random allocation. Thus, the mean capacity increase



across users can be expressed in the following compact form:

$$\mathcal{C}_\Delta = \frac{1}{N_u} \cdot \sum_{i=1}^{N_u} R_s^{(i)} \cdot \log_2 \left( \frac{1 + \left(\frac{C}{I}\right)^\star (\alpha^{(i)}, R_s^{(i)}, f_\Delta^{(i, v_m^*)})}{1 + \left(\frac{C}{I}\right)^\star (\alpha^{(i)}, R_s^{(i)}, f_\Delta^{(i, v_r)})} \right). \quad (4.2.5)$$

It is worth noting that it is the only criterion that is dependent on the considered system nominal bandwidth  $B_N$ .

## Configurations

To evaluate and compare the performance of the proposed DCA methods, 100 randomized configurations<sup>16</sup> are generated for a given number of users  $N_u \in \{1, 2, \dots, 8\}$ . For each carrier, the symbol rate  $R_s$  is generated following a uniform distribution. In other words, each symbol rate is chosen from the interval of remaining available bandwidth until the sum of the bandwidths is equal to  $B_N$ . This allows a good representation of different carriers' characteristics present in practical systems. In order to isolate the allocation gain related to the symbol rate, the roll-off of all users is fixed to the standard value of  $\alpha = 0.05$ .

### 4.2.3 Numerical results

As a first step, general results are discussed for the case  $(C/I)_{AG}^\star \rightarrow +\infty$ . The performance analysis of the CIR formulas is exposed in Table 4.2 in the context

<sup>16</sup>This number is a practical trade-off between the performance statistics and the sum of the configurations execution times.

Table 4.2: Performance analysis of the CIR formulas

Filter distortions representation		Pole-zero	Slope-based	
CIR formula		2	3	
CIR accuracy	$N_u = 8$	max	> 99.99 %	99.85 %
		mean	> 99.99 %	99.67 %
		min	99.99 %	99.25 %
	$N_u = 4$	max	> 99.99 %	99.18 %
		mean	99.99 %	98.26 %
		min	99.99 %	90.32 %
Allocation optimality		100.00 %	94.07 %	
Allocation speed <sup>a</sup>		3	11	

<sup>a</sup>Maximum number of carriers where DCA is performed under 10 seconds (execution time measured on a contemporary 3.5-GHz-processor).

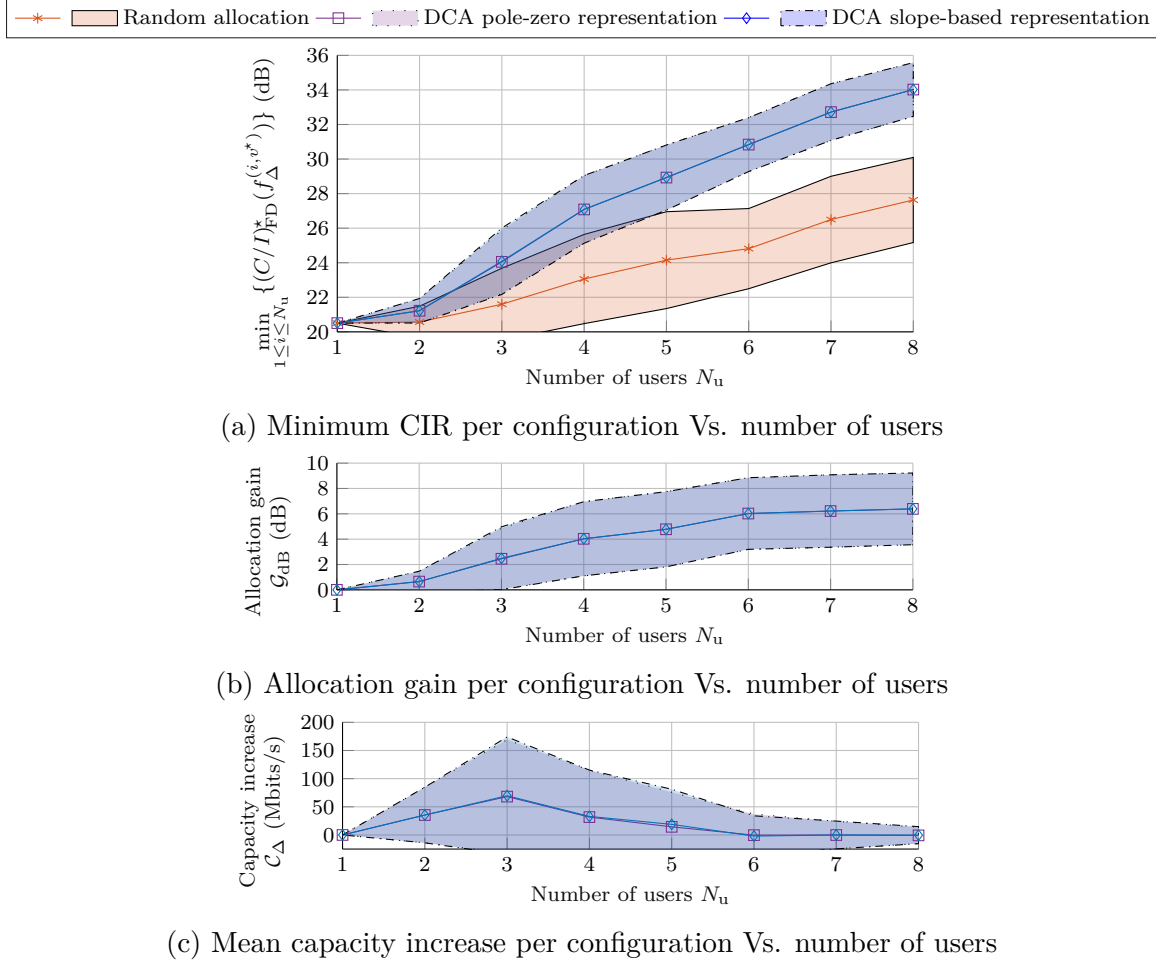


Figure 4-7: Performance analysis of the DCA methods

of real-time DCA optimization. The slope-based representation provides the lowest complexity by a substantial margin. The pole-zero representation relies on a numerical integration and decision instant optimization<sup>17</sup> to compute the CIR, which makes it computationally expensive. Besides complexity, it can be noticed that the mean accuracy is strictly increasing with the number of users. This is especially visible in the case of the slope-based representation, which is based on an approximation of the gain and group delay. Indeed, the higher the number of users  $N_u$  is (given a fixed nominal bandwidth), the more often users have narrower bandwidths (with respect to the nominal bandwidth). Thus, it leads to an approximation that is more accurate statistically. In other words, the smaller the carrier bandwidth is, the more the approximation  $(x_1, y_1) \rightarrow (0, 0)$  becomes true. As a consequence, the slope-based representation is especially well-suited to a high number of users. It is worth noting that the accuracy of the slope-based representation is highly dependent on the filter distortions characteristics. In this context, only one gain ripple and one group delay

<sup>17</sup>The optimization of the decision instant assumes that a timing recovery loop is included in the user receiver terminal.

ripple are present in the channel. By contrast, an elliptical filter containing multiple ripples would lead to a rapid decrease of the slope-based formula accuracy.

The performance analysis of the DCA methods as a function of the number of users  $N_u$  is illustrated in Fig. 4-7. On these graphs, the lines and areas correspond to means and standard deviations, respectively. The allocation gain  $\mathcal{G}_{\text{dB}}$  depicted in Fig. 4-7b is significant for all considered methods. The mean allocation gain is globally increasing with the number of users on the considered interval. For instance, the pole-zero representation reaches  $\mathcal{G}_{\text{dB}} = 4.0$  dB for 4 users and  $\mathcal{G}_{\text{dB}} = 6.0$  dB for 8 users. The measured gain optimality of the proposed methods reaches at least 94.07 % of the time the highest possible DCA gain.

Moreover, the estimated mean capacity increase per user suggests that the DCA max-min optimization leads statistically to more attractive solutions between 2 and 4 users. In the case of 3 users, it is expected to obtain on average a capacity increase of 69.7 Mbits/s per user given all considered configurations. This representative value should be interpreted as an idealistic performance, since it is derived from the case  $(C/I)_{\text{AG}}^* \rightarrow +\infty$  and the increase in capacity is fundamentally system-dependent. Besides that, when the number of users increases, the mean capacity increase becomes smaller as the carriers become statistically narrower. As a last note, more details on possible speed improvements using lookup tables are available in [J1].

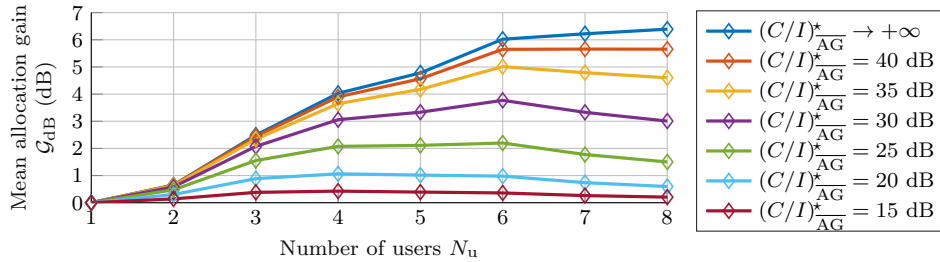


Figure 4-8: Impact of the remaining impairments

Finally, a brief analysis is provided for finite values of  $(C/I)_{\text{AG}}^*$ . The mean allocation gain of the DCA pole-zero representation is illustrated in Fig. 4-8 as a function of  $(C/I)_{\text{AG}}^*$ . Since the allocation gain is relying on CIR variations over the frequency, it can be observed that introducing an AG impairment can reduce the gain perspectives. Indeed, the more dominating the remaining AG impairments are, the fewer variations over the frequency there is. Configurations with more users are more affected, since narrower carriers produce higher CIRs of filter distortions, which are now dominated by the CIR of remaining AG impairments. Overall, it highlights the complex relationship between the filter distortions CIR and the remaining CIR, which are both scenario dependent. In practice, more allocation gain can be obtained when considering the amplifier distortions on top of the filter distortions using Formula 5. However, this requires substantially more investigations, since it increases the number of parameters to take into account and the impairments at stake are more complex. A glimpse of this complexity is highlighted in [C2]. In the end, real-time DCA optimization definitely remains an appealing low-complexity solution to increase the capacity of future UHTS systems.

### Main findings on link budget optimization

To finalize this section, we can draw the following conclusions:

- The formulas proposed in this thesis are particularly well-suited to real-time optimization of the satellite resources.
- The feasibility of real-time DCA has been proved in an UHTS scenario with an average capacity increase per user reaching up to 69.7 Mbits/s.

## 4.3 Summary and future works

In this chapter, crucial applications of the derived CIR formulas were addressed. On the one hand, the step-by-step calculations of the CIR formulas are exposed based on the link budget data of a typical HTS scenario. In this context, it is shown how the amplifier distortions CIR definition of existing link budgets can be improved to obtain more general and more accurate calculations. It is also highlighted that the CIRs of filter distortions, oscillator noise, and waveform imperfections are indispensable complements to assess the impact of filters, oscillators and the waveform on the system. On the other hand, the feasibility of real-time DCA optimization for future UHTS scenarios has been proved. The allocation gain has been thoroughly studied depending on the number of users and AG impairment power. Lastly, the analysis emphasizes that an average capacity increase per user of up to 69.7 Mbits/s can be envisioned.

It would be of interest to extend the work by quantifying the increase in link budget accuracy brought by the derived CIR formulas across multiple realistic scenarios, configurations, and link budget tools. This quantification would in particular require an experimental validation to go beyond the numerical validations. Another recommended step is to extend the study of the DCA optimization to the amplifier distortions CIR, which is more general than the filter distortions CIR and takes into account more parameters. This upgrade would enable an additional increase in allocation gain. However, it would require an intensive work on the complexity reduction to ensure that the DCA optimization is real-time. Indeed, the complexity of the optimization problem and the amplifier distortions CIR grows drastically with the number of users. This constitutes the main future challenge in the context of link budget optimization.

# 5 | Conclusions and Future Research Directions

---

## Contents

5.1	Concluding remarks . . . . .	87
5.2	Directions for future research . . . . .	88

---

### 5.1 Concluding remarks

This thesis has provided sound mathematical foundations and principles to build more accurate link budget analyses and better resources optimization in satellite communications systems. Within the presented mathematical framework, *novel* and practical CIR formulas have been derived for four critical impairments: waveform imperfections, filter distortions, amplifier distortions, and oscillator noise. A summary of the formulas has been presented in Table 3.2. The following examples of applications have been investigated. Firstly, it has been shown that the waveform imperfections parameters can be optimized such as to balance system complexity and the impact of the waveform imperfections CIR (Formula 1) on the system. Secondly, the accuracy of the amplifier distortions CIR in contemporary link budgets has been enhanced using Formula 4 (single-carrier mode) and Formula 5 (multi-carrier mode). Thirdly, the filter distortions CIR (Formulas 2 and 3) and oscillator noise CIR (Formulas 6 and 7) have shown a great potential as link budget complements. On top of that, the theoretical results have been validated with high levels of accuracy through numerical simulations under realistic scenarios. Mathematical tools (exposed in Appendices A and B) and detailed manipulations (exposed in the core of the thesis and Appendix C) have been emphasized to gain further insights. In particular, they facilitate the reproduction of the results as well as the extension of the framework.

In the context of link budget optimization, the feasibility of real-time DCA optimization has been proven for future UHTS scenarios. An in-depth study of the allocation gain and the capacity increase has been performed. In particular, the analysis highlights that an average capacity increase per user of up to 69.7 Mbits/s can typically be envisioned. In conclusion, this thesis constitutes a crucial step toward more rigorous, more refined, and better optimized link budget analyses for future satellite communications systems.

## 5.2 Directions for future research

Based on the results of this thesis, three main directions of research are standing out. Firstly, it is suggested to evaluate experimentally the added accuracy brought by the formulas to extend the results of numerical validations. This would further facilitate the implementation of the derived formulas in existing link budget tools and bring further insights into the physical phenomena involved in the link. Secondly, different extensions of the mathematical framework are possible. On one side, the characterization of other impairments such as future 5G satellite waveform imperfections appears of high interest. On another side, it seems pertinent to further deepen the analysis of certain impairments. In particular, it appears essential to better understand the influence of the optimal decision instant in the context of amplifier distortions. Thirdly, the logical next step of the DCA optimization analysis is to extend the evaluation of performances to the amplifier distortions CIR.

# A | Useful Definitions

---

## A.1 Raised-cosine filter

The RC and SC filters [92] are defined below with energies  $T_s$  and 1, respectively.

### Time domain

$$h_{\text{RC}}(t, \alpha, T_s) = \tag{A.1.1a}$$

$$\begin{cases} 1, & t = 0 \\ \frac{\sin\left(\frac{\pi}{2\alpha}\right)}{\left(\frac{1}{2\alpha}\right)}, & t = \pm \frac{T_s}{2\alpha} \ (\alpha \neq 0) \\ \frac{\sin\left(\frac{\pi t}{T_s}\right) \cos\left(\frac{\pi \alpha t}{T_s}\right)}{\left(\frac{\pi t}{T_s}\right) \left(1 - \left(\frac{2\alpha t}{T_s}\right)^2\right)}, & \text{else} \end{cases}$$

$$h_{\text{SC}}(t, \alpha, T_s) = \tag{A.1.1b}$$

$$\frac{1}{\sqrt{T_s}} \cdot \begin{cases} 1 + \alpha \left(\frac{4}{\pi} - 1\right), & t = 0 \\ \frac{\alpha}{\sqrt{2}} \cdot \left( \left(1 + \frac{2}{\pi}\right) \sin\left(\frac{\pi}{4\alpha}\right) + \left(1 - \frac{2}{\pi}\right) \cos\left(\frac{\pi}{4\alpha}\right) \right), & t = \pm \frac{T_s}{4\alpha} \ (\alpha \neq 0) \\ \frac{\sin\left(\frac{\pi t}{T_s}(1 - \alpha)\right) + \left(4\alpha \frac{t}{T_s}\right) \cos\left(\frac{\pi t}{T_s}(1 + \alpha)\right)}{\left(\frac{\pi t}{T_s}\right) \left(1 - \left(\frac{4\alpha t}{T_s}\right)^2\right)}, & \text{else} \end{cases}$$

### Frequency domain

$$H_{\text{RC}}(f, \alpha, T_s) = \tag{A.1.2a}$$

$$T_s \cdot \begin{cases} 1, & 0 \leq |f| \leq \frac{(1-\alpha)}{2T_s} \\ \frac{1}{2} \left(1 + \cos\left[\frac{\pi T_s}{\alpha} \left(|f| - \frac{(1-\alpha)}{2T_s}\right)\right]\right), & \frac{(1-\alpha)}{2T_s} \leq |f| \leq \frac{(1+\alpha)}{2T_s} \ (\alpha \neq 0) \\ 0, & \text{else} \end{cases}$$

$$H_{\text{SC}}(f, \alpha, T_s) = \sqrt{H_{\text{RC}}(f, \alpha, T_s)} \tag{A.1.2b}$$

For calculations involving a normalization by the symbol period  $T_s$ , the following compact notations are introduced:  $h_{\text{RC}}(t, \alpha) = h_{\text{RC}}(t, \alpha, 1)$ ,  $h_{\text{SC}}(t, \alpha) = h_{\text{SC}}(t, \alpha, 1)$ ,  $H_{\text{RC}}(f, \alpha) = H_{\text{RC}}(f, \alpha, 1)$  and  $H_{\text{SC}}(f, \alpha) = H_{\text{SC}}(f, \alpha, 1)$ .

## A.2 Useful functions and generalized functions

The rectangular function, scaled sine cardinal and Dirac comb are defined as follows:

$$\Pi_T(t) = \begin{cases} 1, & |t| \leq T \\ 0, & \text{else} \end{cases}, \quad (\text{A.2.1})$$

$$\Omega_T(f) = \begin{cases} 2T, & f = 0 \\ \frac{\sin(2T\pi f)}{\pi f}, & \text{else} \end{cases}, \quad (\text{A.2.2})$$

$$\text{III}_F(f) = \sum_{n \in \mathbb{Z}} \delta(f - nF), \quad (\text{A.2.3})$$

where  $T, F \in \mathbb{R}_+^*$  and  $\mathcal{F}[\Pi_T(t)](f) = \Omega_T(f)$ . It is noteworthy to mention that these functions are of particular interest in the context of waveform imperfections.



# B | Useful Identities

---

The following identities have been proved and used in the context of this thesis. They are sorted by categories: series, integrals, limits, stochastic processes, Fourier transforms, and miscellaneous.

## B.1 Series

### Type 1

Assumption:  $\tau \in \mathbb{R}/\mathbb{Z}^*$ .

$$S_{1,2}(\tau) = \sum_{k \in \mathbb{Z}^*} \frac{1}{(\tau + k)^2} = \begin{cases} \frac{\pi^2}{3}, & \tau = 0 \\ \frac{\pi^2}{\sin(\pi\tau)^2} - \frac{1}{\tau^2}, & \text{else} \end{cases} \quad (\text{B.1.1a})$$

$$S_{1,3}(\tau) = \sum_{k \in \mathbb{Z}^*} \frac{1}{(\tau + k)^3} = \begin{cases} 0, & \tau = 0 \\ \frac{\pi^3}{\sin(\pi\tau)^3} \cos(\pi\tau) - \frac{1}{\tau^3}, & \text{else} \end{cases} \quad (\text{B.1.1b})$$

$$S_{1,4}(\tau) = \sum_{k \in \mathbb{Z}^*} \frac{1}{(\tau + k)^4} = \begin{cases} \frac{\pi^4}{45}, & \tau = 0 \\ \frac{\pi^4}{\sin(\pi\tau)^4} \left(1 - \frac{2}{3} \sin(\pi\tau)^2\right) - \frac{1}{\tau^4}, & \text{else} \end{cases} \quad (\text{B.1.1c})$$

$$\text{Induction: } S_{1,n+1}(\tau) = -\frac{1}{n} \frac{\partial S_{1,n}(\tau)}{\partial \tau}, \quad n \geq 2.$$

### Type 2

Assumption:  $x \in [-1; 1]$ .

$$S_{2,2}(x) = \sum_{k=1}^{+\infty} \frac{(-1)^k}{(\pi k)^2} \cos(\pi k x) = \frac{x^2}{4} - \frac{1}{12} \quad (\text{B.1.2a})$$

$$S_{2,3}(x) = \sum_{k=1}^{+\infty} \frac{(-1)^k}{(\pi k)^3} \sin(\pi k x) = \frac{x^3}{12} - \frac{x}{12} \quad (\text{B.1.2b})$$

$$S_{2,4}(x) = \sum_{k=1}^{+\infty} \frac{(-1)^k}{(\pi k)^4} \cos(\pi k x) = -\frac{x^4}{48} + \frac{x^2}{24} - \frac{7}{720} \quad (\text{B.1.2c})$$

$$\text{Induction: } S_{2,n+1}(x) = (-1)^{n+1} \int S_{2,n}(x) dx, \quad n \geq 2.$$

### Type 3

Assumption:  $\alpha \in [0; 1]$ .

$$P_1(\alpha) = \sum_{k \in \mathbb{Z}^*} \begin{cases} \frac{1}{64k^2}, & |k| = \frac{1}{2\alpha} \ (\alpha \neq 0) \\ \frac{\cos(\alpha\pi k)^2}{4(\pi k)^2((2\alpha k)^2 - 1)^2}, & |k| \neq \frac{1}{2\alpha} \end{cases}$$

$$= \alpha^2 \left( \frac{1}{4} - \frac{2}{\pi^2} \right) - \frac{\alpha}{8} + \frac{1}{12} \quad (\text{B.1.3a})$$

$$P_2(\alpha) = \sum_{k \in \mathbb{Z}^*} \begin{cases} \frac{9}{256\pi^2 k^4}, & |k| = \frac{1}{2\alpha} \ (\alpha \neq 0) \\ \left( \frac{\alpha \sin(\alpha\pi k)}{2(\pi k)((2\alpha k)^2 - 1)} + \frac{(3(2\alpha k)^2 - 1) \cos(\alpha\pi k)}{2(\pi k)^2((2\alpha k)^2 - 1)^2} \right)^2, & |k| \neq \frac{1}{2\alpha} \end{cases}$$

$$(\text{B.1.3b})$$

Series calculation: use contour integral based on the methodology presented in [124].

## B.2 Integrals

### Type 1

Assumption:  $\tau \in \mathbb{R}$ .

$$I_{1,0}(\tau) = \int_{-1/2}^{1/2} 1 \cdot \cos(2\pi f\tau) \, df = \frac{\sin(\pi\tau)}{(\pi\tau)} \quad (\text{B.2.1a})$$

$$I_{1,1}(\tau) = \int_{-1/2}^{1/2} f \cdot \sin(2\pi f\tau) \, df = \frac{1}{2} \frac{\sin(\pi\tau)}{(\pi\tau)^2} - \frac{1}{2} \frac{\cos(\pi\tau)}{(\pi\tau)} \quad (\text{B.2.1b})$$

$$I_{1,2}(\tau) = \int_{-1/2}^{1/2} f^2 \cdot \cos(2\pi f\tau) \, df = \frac{1}{4} \frac{\sin(\pi\tau)}{(\pi\tau)^3} ((\pi\tau)^2 - 2) + \frac{1}{2} \frac{\cos(\pi\tau)}{(\pi\tau)^2} \quad (\text{B.2.1c})$$

$$\text{Induction: } I_{1,n+1}(\tau) = \begin{cases} +\frac{(n+1)}{2(\pi\tau)} I_{1,n}(\tau) - \frac{1}{2^{n+1}} \frac{\cos(\pi\tau)}{(\pi\tau)}, & \text{if } n+1 \text{ is odd} \\ -\frac{(n+1)}{2(\pi\tau)} I_{1,n}(\tau) + \frac{1}{2^{n+1}} \frac{\sin(\pi\tau)}{(\pi\tau)}, & \text{if } n+1 \text{ is even} \end{cases}, \quad n \geq 0.$$

### Type 2

$$I_{2,0} = \int_0^1 \frac{\ln(x)^2}{(1-x)^2} \, dx = \frac{\pi^2}{3} \quad (\text{B.2.2a})$$

$$I_{2,1} = \int_0^1 \frac{\ln(x)^2}{(1+x)^2} \, dx = \frac{\pi^2}{6} \quad (\text{B.2.2b})$$

Integral calculation: express the denominator as a geometric series.

## B.3 Limits

Assumption:  $f$  is a continuous function on the predefined interval  $]a, b]$ .

### Type 1

The right Riemann sum on the interval  $]0; 1]$  divided into  $S$  subintervals of length  $1/S$  converges as follows:

$$\frac{1}{S} \cdot \sum_{m=1}^S f\left(\frac{m}{S}\right) \rightarrow \int_0^1 f(x)dx, \text{ as } S \rightarrow +\infty \quad (\text{B.3.1})$$

### Type 2

The right Riemann sum on the interval  $] -S; S]$  divided into  $2 \cdot S$  subintervals, where each subinterval is subdivided into  $N_{S/s}$  subsubintervals of length  $1/N_{S/s}$ , converges as follows:

$$\frac{1}{N_{S/s}} \cdot \sum_{m=-S \cdot N_{S/s}+1}^{S \cdot N_{S/s}} f\left(\frac{m}{N_{S/s}}\right) \rightarrow \int_{-S}^S f(x)dx, \text{ as } N_{S/s} \rightarrow +\infty \quad (\text{B.3.2})$$

## B.4 Stochastic processes

### 16-APSK modulation coefficients

Assumption: a symbol random variable  $\mathcal{S}$  follows the 16-APSK zero-mean unit-power uniform distribution based on Section 2.2.2 and [71], i.e.,  $\mathcal{S} \sim \mathcal{U}\{s_1^{(16)}, s_2^{(16)}, \dots, s_{16}^{(16)}\}$ .

$$r_1 = \mathbb{E}[|\mathcal{S}|^2] = 1 \quad (\text{B.4.1a})$$

$$r_2 = \mathbb{E}[|\mathcal{S}|^4] = 4 \cdot \frac{1 + 3v_1^4}{(1 + 3v_1^2)^2} \quad (\text{B.4.1b})$$

$$r_3 = \mathbb{E}[|\mathcal{S}|^6] = 16 \cdot \frac{1 + 3v_1^6}{(1 + 3v_1^2)^3} \quad (\text{B.4.1c})$$

$$\text{Induction: } r_n = \mathbb{E}[|\mathcal{S}|^{2n}] = 4^{n-1} \cdot \frac{1 + 3v_1^{2n}}{(1 + 3v_1^2)^n}, n \geq 1.$$

### 32-APSK modulation coefficients

Assumption: a symbol random variable  $\mathcal{S}$  follows the 32-APSK zero-mean unit-power uniform distribution based on Section 2.2.2 and [71], i.e.,  $\mathcal{S} \sim \mathcal{U}\{s_1^{(32)}, s_2^{(32)}, \dots, s_{32}^{(32)}\}$ .

$$r_1 = \mathbb{E}[|\mathcal{S}|^2] = 1 \quad (\text{B.4.2a})$$

$$r_2 = \mathbb{E}[|\mathcal{S}|^4] = 8 \cdot \frac{1 + 3v_1^4 + 4v_2^4}{(1 + 3v_1^2 + 4v_2^2)^2} \quad (\text{B.4.2b})$$

$$r_3 = \mathbb{E}[|\mathcal{S}|^6] = 64 \cdot \frac{1 + 3v_1^6 + 4v_2^6}{(1 + 3v_1^2 + 4v_2^2)^3} \quad (\text{B.4.2c})$$

$$\text{Induction: } r_n = \mathbb{E}[|\mathcal{S}|^{2n}] = 8^{n-1} \cdot \frac{1 + 3v_1^{2n} + 4v_2^{2n}}{(1 + 3v_1^2 + 4v_2^2)^n}, \quad n \geq 1.$$

## Useful zero-expectation identities

Assumption: a symbol random variable  $\mathcal{S}$  follows either the PSK or APSK zero-mean unit-power uniform distribution based on Section 2.2.2 and [71].

$$\mathbb{E}[\mathcal{S}] = 0 \quad (\text{B.4.3a})$$

$$\mathbb{E}[\mathcal{S}^*] = 0 \quad (\text{B.4.3b})$$

$$\mathbb{E}[\mathcal{S}^2] = 0 \quad (\text{B.4.3c})$$

$$\mathbb{E}[\mathcal{S}^{*2}] = 0 \quad (\text{B.4.3d})$$

$$\mathbb{E}[\mathcal{S} \cdot |\mathcal{S}|^2] = 0 \quad (\text{B.4.3e})$$

$$\mathbb{E}[\mathcal{S}^{*2} \cdot |\mathcal{S}|^2] = 0 \quad (\text{B.4.3f})$$

## B.5 Fourier transforms

Assumptions:  $T, F \in \mathbb{R}_+^*$ ,  $\beta \in \mathbb{C}$  and  $x : \mathbb{R} \rightarrow \mathbb{C}$  is an integrable function and  $X(f) = \mathcal{F}[x(t)](f)$ .

Table B.1: List of useful Fourier transform identities.

Identity	Time domain	$\xleftrightarrow[\mathcal{F}^{-1}[\cdot]]{\mathcal{F}[\cdot]}$	Frequency domain	
Scaling	$x(t) \cdot \beta$		$X(f) \cdot \beta$	(B.5.1)
Time-shifting	$x(t - T)$		$X(f) \cdot e^{-j2\pi T f}$	(B.5.2)
Frequency-shifting	$x(t) \cdot e^{j2\pi F t}$		$X(f - F)$	(B.5.3)
Sampling	$x(t) \cdot \frac{1}{\sqrt{F}} \cdot \text{III}_{\frac{1}{F}}(t)$		$\sqrt{F} \cdot (X * \text{III}_F)(f)$	(B.5.4)
Time finiteness	$x(t) \cdot \Pi_T(t)$		$(X * \Omega_T)(f)$	(B.5.5)

## B.6 Miscellaneous

The time domain sampling identity can be reformulated as:

$$x(t) \cdot \text{III}_{\frac{1}{F}}(t) = \sum_{n \in \mathbb{Z}} x\left(\frac{n}{F}\right) \delta\left(t - \frac{n}{F}\right) \quad (\text{B.6.1})$$

The frequency domain sampling identity can be reformulated as:

$$(X * \text{III}_F)(f) = \sum_{n \in \mathbb{Z}} X(f - nF) \quad (\text{B.6.2})$$

# C | Proofs

---

## C.1 General carrier-to-interference ratios

### Linear time-invariant system with additive impairment

In the context of waveform imperfections and filter distortions in an LTI system, the received signal at optimal decision instant  $(\tau^* + p)T_s$  can be expressed as:

$$\mathcal{Z}_{(\tau^*+p)T_s} = \sum_{k=p-(N_s-1)}^p \mathcal{S}_{p-k} \cdot h((\tau^* + k)T_s) . \quad (\text{C.1.1})$$

The signal can be decomposed to identify the impairment as follows:

$$\mathcal{Z}_{(\tau^*+p)T_s} = \underbrace{\mathcal{S}_p \cdot h(\tau^*T_s)}_{\text{Transformed useful information}} + \underbrace{\sum_{\substack{k=p-(N_s-1) \\ k \neq 0}}^p \mathcal{S}_{p-k} \cdot h((\tau^* + k)T_s)}_{\text{Zero-mean additive impairment}} , \quad (\text{C.1.2})$$

This leads to the generic CIR expression:

$$\begin{aligned} \left(\frac{C}{I}\right)^* (\alpha, T_s, h) &\stackrel{\substack{\text{Corollary 2} \\ \text{applied to (C.1.2),} \\ \text{border effects neglected}}}{=} \frac{\mathbb{E} [|\mathcal{S}_p \cdot h(\tau^*T_s)|^2]}{\mathbb{E} \left[ \left| \sum_{k \in \mathbb{Z}^*} \mathcal{S}_{p-k} \cdot h((\tau^* + k)T_s) \right|^2 \right]} \\ &\stackrel{\substack{\text{Uncorrelated symbols,} \\ \text{scalar property} \\ \text{of the expectation}}}{=} \frac{\mathbb{E} [|\mathcal{S}_p|^2] \cdot |h(\tau^*T_s)|^2}{\sum_{k \in \mathbb{Z}^*} \mathbb{E} [|\mathcal{S}_{p-k}|^2] \cdot |h((\tau^* + k)T_s)|^2} \\ &\stackrel{\substack{\text{Same average} \\ \text{symbol power}}}{=} \frac{|h(\tau^*T_s)|^2}{\sum_{k \in \mathbb{Z}^*} |h((\tau^* + k)T_s)|^2} , \quad (\text{C.1.3}) \end{aligned}$$

where  $h(t)$  is the system impulse response and  $\tau^*$  is the optimal decision instant offset that maximizes the CIR. It is reminded that the notation  $(C/I)^*$  means that the CIR is defined at optimal decision instant.

## Nonlinear time-invariant system with nonlinear impairment

### Single-carrier mode

In the context of an NTI system with HPA characteristic approximated by the 3<sup>rd</sup>-order-polynomial (as described in Section 2.2.11), the received single-carrier signal at optimal decision instant can be expressed as:

$$\begin{aligned} \mathcal{Z}_{(\tau^*+p)T_s} &= \bar{P}_{\text{HP}}^{\text{in}\frac{1}{2}} \cdot \gamma_1 \cdot \sum_{k_1 \in \mathbb{Z}} \mathcal{S}_{p-k_1} \cdot h^*(k_1) \\ &+ \bar{P}_{\text{HP}}^{\text{in}\frac{3}{2}} \cdot \gamma_3 \cdot \sum_{k_1 \in \mathbb{Z}} \sum_{k_2 \in \mathbb{Z}} \sum_{k_3 \in \mathbb{Z}} \mathcal{S}_{p-k_1} \mathcal{S}_{p-k_2} \mathcal{S}_{p-k_3}^* \cdot h^*(k_1, k_2, k_3) . \end{aligned} \quad (\text{C.1.4})$$

In the case of nonlinear impairments, no convenient signal decomposition is possible, since useful information and impairments are intertwined. The expression for the useful information and the impairment powers can be obtained using the respective formulas from Definition 2 on the whole signal expression. For instance, the useful information expression is defined as  $C_{\text{AD}} = \mathbb{E} \left[ |\mathbb{E}[\mathcal{Z}_{(\tau^*+p)T_s} | \mathcal{S}_p]|^2 \right]$ . This implies that the first calculation steps are the following:

$$\begin{aligned} &\mathbb{E} \left[ \mathcal{Z}_{(\tau^*+p)T_s} | \mathcal{S}_p = s_p \right] \\ &\stackrel{\text{Expectation linearity}}{=} \bar{P}_{\text{HP}}^{\text{in}\frac{1}{2}} \cdot \gamma_1 \cdot \sum_{k_1 \in \mathbb{Z}^*} \mathbb{E}[\mathcal{S}_{p-k_1} | \mathcal{S}_p = s_p] \cdot h^*(k_1) \\ &\quad + \bar{P}_{\text{HP}}^{\text{in}\frac{3}{2}} \cdot \gamma_3 \cdot \left( \sum_{k_1 \in \mathbb{Z}^*} \sum_{k_2 \in \mathbb{Z}^*} \sum_{k_3 \in \mathbb{Z}^*} \mathbb{E}[\mathcal{S}_{p-k_1} \mathcal{S}_{p-k_2} \mathcal{S}_{p-k_3}^* | \mathcal{S}_p = s_p] \cdot h^*(k_1, k_2, k_3) \right) \\ &\stackrel{\text{Non-zero expectations}}{=} \bar{P}_{\text{HP}}^{\text{in}\frac{1}{2}} \cdot \gamma_1 \cdot s_p \cdot h^*(0) + \bar{P}_{\text{HP}}^{\text{in}\frac{3}{2}} \cdot \gamma_3 \cdot \left( s_p s_p s_p^* \cdot h^*(0, 0, 0) + 2 \cdot s_p \cdot \sum_{k \in \mathbb{Z}^*} h^*(0, k, k) \right) \end{aligned} \quad (\text{C.1.5})$$

since the remaining non-zero expectations are:

$$\mathbb{E}[s_p | \mathcal{S}_p = s_p] = s_p , \quad (\text{C.1.6a})$$

$$\mathbb{E}[s_p s_p s_p^* | \mathcal{S}_p = s_p] = s_p s_p s_p^* , \quad (\text{C.1.6b})$$

$$\mathbb{E}[s_p \mathcal{S}_{p-k} \mathcal{S}_{p-k}^* | \mathcal{S}_p = s_p] = s_p , \quad k \in \mathbb{Z}^* , \quad (\text{C.1.6c})$$

$$\mathbb{E}[\mathcal{S}_{p-k} s_p \mathcal{S}_{p-k}^* | \mathcal{S}_p = s_p] = s_p , \quad k \in \mathbb{Z}^* . \quad (\text{C.1.6d})$$

Based on this result, the calculation of  $\mathbb{E} \left[ |\mathbb{E}[\mathcal{Z}_{(\tau^*+p)T_s} | \mathcal{S}_p]|^2 \right]$  leading to the expression  $C_{\text{AD}} = \bar{P}_{\text{HP}}^{\text{in}} \cdot |\gamma_1|^2 \cdot C_1 + \bar{P}_{\text{HP}}^{\text{in}^2} \cdot 2 \cdot \text{Re}(\gamma_1^* \gamma_3 \cdot C_2) + \bar{P}_{\text{HP}}^{\text{in}^3} \cdot |\gamma_3|^2 \cdot C_3$  in Section 3.3.2 becomes trivial. Regarding the calculation of the impairment power  $I_{\text{AD}} = \mathbb{E} \left[ \mathbb{V}[\mathcal{Z}_{(\tau^*+p)T_s} | \mathcal{S}_p] \right]$ , one approach is to split the variance into  $\mathbb{V}[\mathcal{Z}_{(\tau^*+p)T_s} | \mathcal{S}_p = s_p] = \mathbb{E} \left[ |\mathcal{Z}_{(\tau^*+p)T_s}|^2 | \mathcal{S}_p = s_p \right] - \left| \mathbb{E}[\mathcal{Z}_{(\tau^*+p)T_s} | \mathcal{S}_p = s_p] \right|^2$  and use the previous expression (C.1.5).

## Two-carrier mode

To emphasize the basics of CIR calculations in multi-carrier mode, a two-carrier example is exposed. At the user 1 received terminal, the signal defined at optimal decision instant can be expressed as:

$$\begin{aligned}
& \mathcal{Z}_{(\tau^*+p)T_s^{(1)}}^{(1)} \\
&= \boxed{\bar{P}_{\text{HP}}^{\text{in}\frac{1}{2}} \cdot \lambda_{\text{HP}}^{(1)\frac{1}{2}} \cdot \gamma_1 \cdot \sum_{k_1 \in \mathbb{Z}} \mathcal{S}_{p-k_1}^{(1)} \cdot h^{*(1,1)}(k_1; 0)} \\
&+ \bar{P}_{\text{HP}}^{\text{in}\frac{1}{2}} \cdot \lambda_{\text{HP}}^{(2)\frac{1}{2}} \cdot \gamma_1 \cdot \sum_{k_1 \in \mathbb{Z}} \mathcal{S}_{p-k_1}^{(2)} \cdot h^{*(2,1)}(k_1; f_{\Delta}^{(2)} - f_{\Delta}^{(1)}) \\
&+ \boxed{\bar{P}_{\text{HP}}^{\text{in}\frac{3}{2}} \cdot \lambda_{\text{HP}}^{(1)\frac{3}{2}} \cdot \gamma_3 \cdot \sum_{k_1 \in \mathbb{Z}} \sum_{k_2 \in \mathbb{Z}} \sum_{k_3 \in \mathbb{Z}} \mathcal{S}_{p-k_1}^{(1)} \mathcal{S}_{p-k_2}^{(1)} \mathcal{S}_{p-k_3}^{(1)*} \cdot h^{*(1,1,1,1)}(k_1, k_2, k_3; 0)} \\
&+ \bar{P}_{\text{HP}}^{\text{in}\frac{3}{2}} \cdot \lambda_{\text{HP}}^{(1)\frac{3}{2}} \cdot \gamma_3 \cdot \sum_{k_1 \in \mathbb{Z}} \sum_{k_2 \in \mathbb{Z}} \sum_{k_3 \in \mathbb{Z}} \mathcal{S}_{p-k_1}^{(1)} \mathcal{S}_{p-k_2}^{(2)} \mathcal{S}_{p-k_3}^{(1)*} \cdot h^{*(1,2,1,1)}(k_1, k_2, k_3; f_{\Delta}^{(2)} - f_{\Delta}^{(1)}) \cdot 2 \\
&+ \bar{P}_{\text{HP}}^{\text{in}\frac{3}{2}} \cdot \lambda_{\text{HP}}^{(1)\frac{3}{2}} \cdot \gamma_3 \cdot \sum_{k_1 \in \mathbb{Z}} \sum_{k_2 \in \mathbb{Z}} \sum_{k_3 \in \mathbb{Z}} \mathcal{S}_{p-k_1}^{(1)} \mathcal{S}_{p-k_2}^{(1)} \mathcal{S}_{p-k_3}^{(2)*} \cdot h^{*(1,1,2,1)}(k_1, k_2, k_3; f_{\Delta}^{(1)} - f_{\Delta}^{(2)}) \\
&+ \boxed{\bar{P}_{\text{HP}}^{\text{in}\frac{3}{2}} \cdot \lambda_{\text{HP}}^{(1)\frac{3}{2}} \cdot \gamma_3 \cdot \sum_{k_1 \in \mathbb{Z}} \sum_{k_2 \in \mathbb{Z}} \sum_{k_3 \in \mathbb{Z}} \mathcal{S}_{p-k_1}^{(1)} \mathcal{S}_{p-k_2}^{(2)} \mathcal{S}_{p-k_3}^{(2)*} \cdot h^{*(1,2,2,1)}(k_1, k_2, k_3; 0) \cdot 2} \\
&+ \bar{P}_{\text{HP}}^{\text{in}\frac{3}{2}} \cdot \lambda_{\text{HP}}^{(1)\frac{3}{2}} \cdot \gamma_3 \cdot \sum_{k_1 \in \mathbb{Z}} \sum_{k_2 \in \mathbb{Z}} \sum_{k_3 \in \mathbb{Z}} \mathcal{S}_{p-k_1}^{(2)} \mathcal{S}_{p-k_2}^{(2)} \mathcal{S}_{p-k_3}^{(1)*} \cdot h^{*(2,2,1,1)}(k_1, k_2, k_3; 2 \cdot (f_{\Delta}^{(2)} - f_{\Delta}^{(1)})) \\
&+ \bar{P}_{\text{HP}}^{\text{in}\frac{3}{2}} \cdot \lambda_{\text{HP}}^{(1)\frac{3}{2}} \cdot \gamma_3 \cdot \sum_{k_1 \in \mathbb{Z}} \sum_{k_2 \in \mathbb{Z}} \sum_{k_3 \in \mathbb{Z}} \mathcal{S}_{p-k_1}^{(2)} \mathcal{S}_{p-k_2}^{(2)} \mathcal{S}_{p-k_3}^{(2)*} \cdot h^{*(2,2,2,1)}(k_1, k_2, k_3; f_{\Delta}^{(2)} - f_{\Delta}^{(1)}),
\end{aligned} \tag{C.1.7}$$

where only the terms enclosed in dotted boxes are involved in the useful information power of user 1. Indeed, all the other terms are canceled out with the expectation operation due to uncorrelation between symbols and the use of typical identities presented in Appendix B.4.3. In the two-carrier mode, only the third enclosed term is related to user 2. In the general multi-carrier mode, the same type of symbol combination is repeated for all the other users. Lastly, all listed terms are involved in the interference power computation with different degrees of influence.

## Linear time-invariant system with multiplicative impairment

In the context of WSS oscillator phase noise in an LTI system, the received signal at optimal decision instant can be expressed as:

$$\mathcal{Z}_{(\tau^*+p)T_s} = \sum_{k \in \mathbb{Z}} \mathcal{S}_{p-k} \cdot \int_{\mathbb{R}} h_{\text{SC}}(kT_s - u) h_{\text{SC}}(u) \cdot e^{j\Theta(u)} du, \quad (\text{C.1.8})$$

The signal can be decomposed to identify the impairment as follows:

$$\mathcal{Z}_{(\tau^*+p)T_s} = \underbrace{\mathcal{S}_p \cdot \int_{\mathbb{R}} h_{\text{SC}}(u)^2 \cdot e^{j\Theta(u)} du}_{\text{Transformed useful information with multiplicative impairment}} + \underbrace{\sum_{k \in \mathbb{Z}^*} \mathcal{S}_{p-k} \cdot \int_{\mathbb{R}} h_{\text{SC}}(kT_s - u) h_{\text{SC}}(u) \cdot e^{j\Theta(u)} du}_{\text{Additive impairment}}, \quad (\text{C.1.9})$$

This leads to the oscillator noise CIR expression:

$$\begin{aligned} & \left( \frac{C}{I} \right)_{\text{ON}}^* (\alpha, T_s, h^\Phi) \\ & \stackrel{\substack{\text{Generalized CIR} \\ \text{Definition 2} \\ \text{applied to (C.1.9)}}}{=} \frac{\mathbb{E} \left[ |\mathcal{S}_p|^2 \cdot \left| \mathbb{E} \left[ \int_{-\infty}^{+\infty} h_{\text{SC}}(u)^2 \cdot e^{j\Theta(u)} du \right] \right|^2 \right]}{\mathbb{E} \left[ \begin{aligned} & |\mathcal{S}_p|^2 \cdot \mathbb{V} \left[ \int_{-\infty}^{+\infty} h_{\text{SC}}(u)^2 \cdot e^{j\Theta(u)} du \right] + \dots + \\ & \mathbb{V} \left[ \sum_{k \in \mathbb{Z}^*} \mathcal{S}_{p-k} \cdot \int_{-\infty}^{+\infty} h_{\text{SC}}(kT_s - u) h_{\text{SC}}(u) \cdot e^{j\Theta(u)} du \right] \end{aligned} \right]} \\ & \stackrel{\substack{\text{Symbol power} \\ \text{simplification,} \\ \text{variance definition} \\ \text{and recombination}}}{=} \frac{\left| \mathbb{E} \left[ \int_{-\infty}^{+\infty} h_{\text{SC}}(u)^2 \cdot e^{j\Theta(u)} du \right] \right|^2}{\sum_{(k_1, k_2) \in \mathbb{Z}_{(u,v)}^2} \iint_{(u,v) \in \mathbb{R}^2} h_{\text{SC}}(k_1 T_s - u) h_{\text{SC}}(k_2 T_s - v) h_{\text{SC}}(u) h_{\text{SC}}(v) \cdot \mathbb{C}[e^{j\Theta(u)}; e^{j\Theta(v)}] du dv} \\ & \stackrel{\substack{\text{Numerator and} \\ \text{covariance calculation} \\ \text{using Proof C.5}}}{=} \frac{e^{-\varepsilon_{\Phi, \text{tot}}}}{\sum_{(k_1, k_2) \in \mathbb{Z}_{(u,v)}^2} \iint_{(u,v) \in \mathbb{R}^2} h_{\text{SC}}(k_1 T_s - u) h_{\text{SC}}(k_2 T_s - v) h_{\text{SC}}(u) h_{\text{SC}}(v) \cdot \left( e^{-\varepsilon_{\Phi, \text{tot}} \left( 1 - \frac{\varepsilon_{\Phi}(u,v)}{\varepsilon_{\Phi, \text{tot}}} \right)} - e^{-\varepsilon_{\Phi, \text{tot}}} \right) du dv} \\ & \stackrel{\substack{\text{Compact expression}}}{=} \frac{1}{\sum_{(k_1, k_2) \in \mathbb{Z}_{(u,v)}^2} \iint_{(u,v) \in \mathbb{R}^2} h_{\text{SC}}(k_1 T_s - u) h_{\text{SC}}(k_2 T_s - v) h_{\text{SC}}(u) h_{\text{SC}}(v) \cdot (e^{\varepsilon_{\Phi}(u,v)} - 1) du dv}, \quad (\text{C.1.10}) \end{aligned}$$

where  $\varepsilon_{\Phi}(u, v)$  and  $\varepsilon_{\Phi, \text{tot}}$  are the aggregate phase noise mask filter autocorrelation and the aggregate phase noise mask filter energy, respectively.



## C.2 Waveform imperfections

Asymptote ( $\alpha = 0, N_{S/s} \rightarrow +\infty$ )

$$\begin{aligned}
\left(\frac{C}{I}\right)_{\text{WI}}(0, S) &\stackrel{\text{CIR definition (3.1.2)}}{=} \frac{\left|\int_{-S}^S h_{\text{SC}}(u, 0)^2 du\right|^2}{2 \cdot \sum_{k=1}^{2S-1} \left|\int_{k-S}^S h_{\text{SC}}(u, 0) h_{\text{SC}}(k-u, 0) du\right|^2} \\
&\stackrel{\text{SC definition (A.1.1b)}}{=} \frac{\left|\int_{-S}^S \frac{\sin(\pi u)^2}{(\pi u)^2} du\right|^2}{2 \cdot \sum_{k=1}^{2S-1} \left|\int_{k-S}^S \frac{\sin(\pi u)}{(\pi u)} \frac{\sin(\pi(k-u))}{(\pi(k-u))} du\right|^2} \\
&\stackrel{\text{Integration, expansion}}{\rightarrow} \frac{1}{\frac{2}{\pi^4} \cdot \left( \sum_{k=1}^{S-1} \frac{(\ln(S) - \ln(S-k))^2}{k^2} + \sum_{k=S+1}^{2S-1} \frac{(\ln(S) - \ln(k-S))^2}{k^2} \right)} \\
&\stackrel{\text{Sum combination}}{\rightarrow} \frac{1}{\frac{2}{\pi^4} \cdot \frac{1}{S} \cdot \frac{1}{S} \cdot \sum_{k=1}^{S-1} \ln\left(\frac{k}{S}\right)^2 \left( \frac{1}{\left(1 - \left(\frac{k}{S}\right)\right)^2} + \frac{1}{\left(1 + \left(\frac{k}{S}\right)\right)^2} \right)} \\
&\stackrel{\text{Riemann sum (B.3.1)}}{\rightarrow} \frac{1}{\frac{2}{\pi^4} \cdot \frac{1}{S} \cdot \int_0^1 \ln(x)^2 \left( \frac{1}{(1-x)^2} + \frac{1}{(1+x)^2} \right) dx} \\
&\stackrel{\text{Integration (B.2.2)}}{\rightarrow} \frac{1}{\frac{2}{\pi^4} \cdot \frac{1}{S} \cdot \frac{\pi^2}{2}} \\
&\rightarrow \pi^2 S, \quad \text{as } S \rightarrow +\infty.
\end{aligned} \tag{C.2.1}$$

### C.3 Filter distortions

Asymptote ( $N_{\text{FD}} = 1$ )

$$\begin{aligned}
\left(\frac{C}{I}\right)_{\text{FD}}^{\star}(\alpha, x_1, y_1) &\stackrel{\text{CIR definition Formula 2}}{=} \frac{\left|\int_{\mathbb{R}} H_{\text{RC}}(f, \alpha) \cdot H_{\text{CH}}(f, x_1, y_1) \cdot e^{j2\pi f \tau^{\star}} df\right|^2}{\sum_{k \in \mathbb{Z}^*} \left|\int_{\mathbb{R}} H_{\text{RC}}(f, \alpha) \cdot H_{\text{CH}}(f, x_1, y_1) \cdot e^{j2\pi f(\tau^{\star} + k)} df\right|^2} \\
&\stackrel{\substack{\tau^{\star} \rightarrow 0, \\ H_{\text{CH}}(f, x_1, y_1) \\ \text{definition (3.2.7)}}}{\rightarrow} \frac{\left|\int_{\mathbb{R}} H_{\text{RC}}(f, \alpha) \cdot e^{\xi x_1 f - j\pi y_1 f^2} df\right|^2}{\sum_{k \in \mathbb{Z}^*} \left|\int_{\mathbb{R}} H_{\text{RC}}(f, \alpha) \cdot e^{\xi x_1 f - j\pi y_1 f^2} \cdot e^{j2\pi f k} df\right|^2} \\
&\stackrel{\substack{H_{\text{CH}}(f, x_1, y_1) \\ \text{expansion}}}{\rightarrow} \frac{\left|\int_{\mathbb{R}} H_{\text{RC}}(f, \alpha) \cdot (1 + \xi x_1 f - j\pi y_1 f^2) df\right|^2}{\sum_{k \in \mathbb{Z}^*} \left|\int_{\mathbb{R}} H_{\text{RC}}(f, \alpha) \cdot (1 + \xi x_1 f - j\pi y_1 f^2) \cdot e^{j2\pi f k} df\right|^2} \\
&\stackrel{\substack{H_{\text{RC}}(f, \alpha) \text{ Nyquist} \\ \text{property (2.2.3)}}}{\rightarrow} \frac{1}{\sum_{k \in \mathbb{Z}^*} \left|\int_{\mathbb{R}} H_{\text{RC}}(f, \alpha) \cdot (\xi x_1 f - j\pi y_1 f^2) \cdot e^{j2\pi f k} df\right|^2} \\
&\stackrel{\substack{\text{Symmetry} \\ \text{in frequency}}}{\rightarrow} \frac{1}{\sum_{k \in \mathbb{Z}^*} \left( \begin{aligned} &(\xi x_1) \cdot \int_{\mathbb{R}} H_{\text{RC}}(f, \alpha) \cdot f \cdot \sin(2\pi f k) df \\ & - (\pi y_1) \cdot \int_{\mathbb{R}} H_{\text{RC}}(f, \alpha) \cdot f^2 \cdot \cos(2\pi f k) df \end{aligned} \right)^2} \\
&\stackrel{\substack{\text{Development,} \\ \text{sum cancellation} \\ \text{of cross-term } (x_1 y_1)}}{\rightarrow} \frac{1}{(\xi x_1)^2 \cdot \sum_{k \in \mathbb{Z}^*} \left( \int_{\mathbb{R}} H_{\text{RC}}(f, \alpha) \cdot f \cdot \sin(2\pi f k) df \right)^2 + (\pi y_1)^2 \cdot \sum_{k \in \mathbb{Z}^*} \left( \int_{\mathbb{R}} H_{\text{RC}}(f, \alpha) \cdot f^2 \cdot \cos(2\pi f k) df \right)^2} \\
&\stackrel{\substack{\text{Integration,} \\ \text{summation} \\ \text{using (B.1.3)}}}{\rightarrow} \frac{1}{(\xi x_1)^2 \cdot P_1(\alpha) + (\pi y_1)^2 \cdot P_2(\alpha)}, \quad \text{as } (x_1, y_1) \rightarrow (0, 0).
\end{aligned} \tag{C.3.1}$$

An efficient approach to find out that the optimal decision instant offset is asymptotically zero (i.e.,  $\tau^{\star} \rightarrow 0$  as  $(x_1, y_1) \rightarrow (0, 0)$ ) is to study the derivative of the CIR with respect to the epoch and to consider the epoch as a polynomial function of the filter distortions parameters:  $\tau = ax_1 + by_1$ ,  $(a, b) \in \mathbb{R}^2$  as  $(x_1, y_1) \rightarrow (0, 0)$ . This leads to  $a = b = 0$ .

## C.4 Amplifier distortions

Adjacent channel interference ( $\alpha^{(i)} = \alpha^{(q)} = 0, N_{\text{AD}} = 0$ )

$$\begin{aligned}
& \left( \frac{C}{I} \right)_{\text{AD}}^{(i)\star} \left( 0, 0, T_s^{(i)}, T_s^{(q)}, \bar{P}_{\text{HP}}^{\text{in}(i)}, \bar{P}_{\text{HP}}^{\text{in}(q)}, f_{\Delta}^{(i)}, f_{\Delta}^{(q)} \right) \\
& \stackrel{\text{Formula 5, } N_{\text{AD}}=0,}{f_{\Delta}^{(q,i)} = |f_{\Delta}^{(q)} - f_{\Delta}^{(i)}|} \frac{\bar{P}_{\text{HP}}^{\text{in}(i)} \cdot |h_{\text{RC}}(t, 0, T_s^{(i)})|^2}{\bar{P}_{\text{HP}}^{\text{in}(q)} \cdot \sum_{k \in \mathbb{Z}} \left| \int_{\mathbb{R}} H_{\text{SC}}(f - f_{\Delta}^{(q,i)}, 0, T_s^{(q)}) \cdot H_{\text{SC}}(f, 0, T_s^{(i)}) \cdot e^{j2\pi f k T_s^{(i)}} df \right|^2} \\
& \stackrel{\tilde{f} = f T_s^{(i)}}{=} \frac{1}{\lambda_{\text{HP}}^{(q,i)} \cdot \sum_{k \in \mathbb{Z}} \left| \int_{\mathbb{R}} H_{\text{SC}}(\tilde{f} - \tilde{f}_{\Delta}^{(q,i)}, 0, \zeta^{(q,i)}) \cdot H_{\text{SC}}(\tilde{f}, 0) \cdot e^{j2\pi \tilde{f} k} d\tilde{f} \right|^2} \\
& \stackrel{\text{Rectangular function property}}{=} \frac{1}{\lambda_{\text{HP}}^{(q,i)} \cdot \sum_{k \in \mathbb{Z}} \left| \int_{\tilde{f}_{\Delta}^{(q,i)} - \frac{\zeta^{(q,i)}}{2}}^{\tilde{f}_{\Delta}^{(q,i)} + \frac{\zeta^{(q,i)}}{2}} \Pi_{\frac{1}{2}}(\tilde{f}) \cdot e^{j2\pi \tilde{f} k} d\tilde{f} \right|^2} \\
& \stackrel{\text{Discontinuity in } k=0}{=} \frac{1}{\lambda_{\text{HP}}^{(q,i)} \cdot \left| \int_{\tilde{f}_{\Delta}^{(q,i)} - \frac{\zeta^{(q,i)}}{2}}^{\tilde{f}_{\Delta}^{(q,i)} + \frac{\zeta^{(q,i)}}{2}} \Pi_{\frac{1}{2}}(\tilde{f}) d\tilde{f} \right|^2 + \lambda_{\text{HP}}^{(q,i)} \cdot \sum_{k \in \mathbb{Z}^*} \left| \int_{\tilde{f}_{\Delta}^{(q,i)} - \frac{\zeta^{(q,i)}}{2}}^{\tilde{f}_{\Delta}^{(q,i)} + \frac{\zeta^{(q,i)}}{2}} \Pi_{\frac{1}{2}}(\tilde{f}) \cdot e^{j2\pi \tilde{f} k} d\tilde{f} \right|^2} \\
& \stackrel{\tilde{f}_{\Delta}^{(q,i)} \text{ symmetry, } |\tilde{f}_{\Delta}^{(q,i)}| < \frac{1+\zeta^{(q,i)}}{2}}{=} \frac{1}{\lambda_{\text{HP}}^{(q,i)} \cdot \left| \int_{|\tilde{f}_{\Delta}^{(q,i)}| - \frac{\zeta^{(q,i)}}{2}}^{\frac{1}{2}} 1 d\tilde{f} \right|^2 + \lambda_{\text{HP}}^{(q,i)} \cdot \sum_{k \in \mathbb{Z}^*} \left| \int_{|\tilde{f}_{\Delta}^{(q,i)}| - \frac{\zeta^{(q,i)}}{2}}^{\frac{1}{2}} e^{j2\pi \tilde{f} k} d\tilde{f} \right|^2} \\
& \stackrel{\text{Integration, } \tilde{f}_{\text{lim}}^{(q,i)} \text{ notation}}{=} \frac{1}{\lambda_{\text{HP}}^{(q,i)} \cdot \left( \tilde{f}_{\text{lim}}^{(q,i)} - |\tilde{f}_{\Delta}^{(q,i)}| \right)^2 + \lambda_{\text{HP}}^{(q,i)} \cdot \left[ \frac{1}{\pi^2} \sum_{k=1}^{\infty} \frac{1}{k^2} - \sum_{k=1}^{\infty} \frac{(-1)^k}{(\pi k)^2} \cos \left( 2\pi k \left( |\tilde{f}_{\Delta}^{(q,i)}| - \frac{\zeta^{(q,i)}}{2} \right) \right) \right]} \\
& \stackrel{\text{Summation using (B.1.1a) and (B.1.2a)}}{=} \frac{1}{\lambda_{\text{HP}}^{(q,i)} \cdot \left( \tilde{f}_{\text{lim}}^{(q,i)} - |\tilde{f}_{\Delta}^{(q,i)}| \right)^2 + \lambda_{\text{HP}}^{(q,i)} \cdot \left[ \left( \tilde{f}_{\text{lim}}^{(q,i)} - |\tilde{f}_{\Delta}^{(q,i)}| \right) - \left( \tilde{f}_{\text{lim}}^{(q,i)} - |\tilde{f}_{\Delta}^{(q,i)}| \right)^2 \right]} \\
& = \frac{1}{\lambda_{\text{HP}}^{(q,i)} \cdot \left( \tilde{f}_{\text{lim}}^{(q,i)} - |\tilde{f}_{\Delta}^{(q,i)}| \right)}, \quad \text{as } |\tilde{f}_{\Delta}^{(q,i)}| < \tilde{f}_{\text{lim}}^{(q,i)}, \tag{C.4.1}
\end{aligned}$$

where  $\tilde{f}_{\Delta}^{(q,i)} = f_{\Delta}^{(q,i)} T_s^{(i)}$ ,  $\lambda_{\text{HP}}^{(q,i)} = \lambda_{\text{HP}}^{(q)} / \lambda_{\text{HP}}^{(i)}$ ,  $\zeta^{(q,i)} = T_s^{(q)} / T_s^{(i)}$ , and  $\tilde{f}_{\text{lim}}^{(q,i)} = (1 + \zeta^{(q,i)})/2$  represent the distance between the carriers of the users in frequency (normalized by  $T_s^{(i)}$ ), the power ratio between the  $q^{\text{th}}$ -user and the  $i^{\text{th}}$ -user, the symbol period ratio between the  $q^{\text{th}}$ -user and the  $i^{\text{th}}$ -user, and the frequency limit at which the carriers starts overlapping (normalized by  $T_s^{(i)}$ ), respectively. The CIR of linear adjacent channel interference is zero when the carriers are not overlapping (i.e.,  $|\tilde{f}_{\Delta}^{(q,i)}| \geq \tilde{f}_{\text{lim}}^{(q,i)}$ ).

## C.5 Oscillator noise

### Covariance derivation

A crucial step in the determination of the oscillator noise CIR relies on the derivation of the following covariance:

$$\mathbb{C}[e^{j\Theta(u)}; e^{j\Theta(v)}] = \mathbb{E}[e^{j(\Theta(u)-\Theta(v))}] - \mathbb{E}[e^{j\Theta(u)}]\mathbb{E}[e^{-j\Theta(v)}] , \quad (\text{C.5.1})$$

where three expectations of zero-mean wrapped Gaussian random process can be recognized and lead to:

$$\mathbb{E}[e^{j(\Theta(u)-\Theta(v))}] = e^{-\frac{\mathbb{V}[\Theta(u)-\Theta(v)]}{2}} , \quad (\text{C.5.2a})$$

$$\mathbb{E}[e^{j\Theta(u)}] = e^{-\frac{\mathbb{V}[\Theta(u)]}{2}} , \quad (\text{C.5.2b})$$

$$\mathbb{E}[e^{-j\Theta(v)}] = e^{-\frac{\mathbb{V}[-\Theta(v)]}{2}} = e^{-\frac{\mathbb{V}[\Theta(v)]}{2}} . \quad (\text{C.5.2c})$$

Furthermore, the arguments of the two last expectations (C.5.2b) and (C.5.2c) can be determined from the fact that:

$$\mathbb{V}[\Theta(u)] = \varepsilon_{\Phi, \text{tot}} \cdot \mathbb{V}[\Phi(u)] = \varepsilon_{\Phi, \text{tot}} , \quad (\text{C.5.3})$$

where  $\varepsilon_{\Phi, \text{tot}}$  is the energy of the aggregate phase noise mask filter. On the other hand, the argument of the first expectation (C.5.2a) develops as follows:

$$\mathbb{V}[\Theta(u) - \Theta(v)] = \mathbb{V}[\Theta(u)] + \mathbb{V}[\Theta(v)] - 2 \cdot \text{Cov}[\Theta(u); \Theta(v)] . \quad (\text{C.5.4})$$

Using the definitions of the covariance and  $\Phi(t)$ , the last term can be developed as:

$$\begin{aligned} \mathbb{C}[\Theta(u); \Theta(v)] &= \mathbb{E}[\Theta(u)\Theta^*(v)] \\ &= \int_{\mathbb{R}} h^{\Phi}(u-t)h^{\Phi*}(v-t)\mathbb{E}[\Phi^2(t)]dt \\ &= \int_{\mathbb{R}} h^{\Phi}(u-t)h^{\Phi*}(v-t)dt \\ &= \int_{\mathbb{R}} h^{\Phi}(t' + (u-v))h^{\Phi*}(t')dt' , \end{aligned} \quad (\text{C.5.5})$$

which is in fact the autocorrelation of the aggregate phase noise mask filter later denoted by  $\varepsilon_{\Phi}(u, v)$ . Finally,

$$\mathbb{E}[e^{j(\Theta(u)-\Theta(v))}] = e^{-\varepsilon_{\Phi, \text{tot}} \left(1 - \frac{\varepsilon_{\Phi}(u, v)}{\varepsilon_{\Phi, \text{tot}}}\right)} , \quad (\text{C.5.6})$$

which results in the following expression of the covariance:

$$\mathbb{C}[e^{j\Theta(u)}; e^{j\Theta(v)}] = e^{-\varepsilon_{\Phi, \text{tot}} \left(1 - \frac{\varepsilon_{\Phi}(u, v)}{\varepsilon_{\Phi, \text{tot}}}\right)} - e^{-\varepsilon_{\Phi, \text{tot}}} . \quad (\text{C.5.7})$$

# D | Data

Table D.1: Summary of link budget input data

	Carrier	
Selected MODCOD	32-APSK 9/10	
Symbol rate (Mbauds)	36.571	
Roll-off	0.05	
	Satellite	
<b>General:</b>		
Name	Al Yah 2	
Longitude (°E)	47.5	
Link	Forward	
OMUX nominal bandwidth $B_N$ (MHz)	115.2	
Antenna gain-to-noise temperature ratio $G/T$ (dB/K)	17.05	
<b>Spotbeam:</b>		
Number	5	
EIRP (dBW)	60.74	
OBO (dB)	14.29	
<b>Carrier-to-impairment power ratio:</b>		
Amplifier distortions CIR at PEB <sup>a</sup> (dB)	42.46	
	Uplink	Downlink
<b>Location:</b>		
Longitude (°E)	−3.5	35.5
Latitude (°N)	40.5	33.88
Altitude (km)	0.863	0.69
<b>Frequency:</b>		
Center frequency (GHz)	28.18	19.88
Polarization (V, H or C)	C	C
<b>Antenna:</b>		
Diameter (m)	7.3	2.4
Efficiency (%)	54	70
Noise temperature (K)	—	51
Depointing loss (dB)	0.3	0.3
<b>Transmission:</b>		
HPA power at saturation (dBW)	21.2	—
OBO (dB)	2.5	—

<b>Reception:</b>		
LNB noise figure (dB)	—	1.8
Coupling losses (dB)	—	0.05
<b>Carrier-to-impairment power ratios:</b>		
Amplifier distortions CIR (dB)	25.77	—
Adjacent channel interference CIR at PEB <sup>a</sup> (dB)	21	23.22
Adjacent satellite interference CIR at PEB <sup>a</sup> (dB)	35	33.28
Cross-polar interference CIR at PEB <sup>a</sup> (dB)	35	22.54

<sup>a</sup>Power equivalent bandwidth (PEB).

Table D.2: Summary of link budget output data (clear sky)

	Carrier	
Bandwidth (MHz)	38.4	
Gross bit rate (Mbits/s)	164.570	
Net bit rate (Mbits/s)	159.338	
	Uplink	Downlink
<b>Transmission:</b>		
Antenna gain (dB)	64	52.43
HPA power at saturation (dBW)	21.2	—
EIRP (dBW)	82.5	—
<b>Losses:</b>		
Antenna depointing loss (dB)	0.3	0.3
Free-space path loss (dB)	213.38	209.82
Total atmospheric attenuation (dB)	0.65	0.36
Total path losses (dB)	214.04	210.18
<b>Reception:</b>		
Total system noise temperature	—	202.7
Antenna gain-to-noise temperature ratio $G/T$ (dB/K)	17.05	29.31
<b>Carrier-to-impairment power ratios:</b>		
Thermal noise CIR (dB)	38.18	<b>23.65</b>
Amplifier distortions CIR (dB)	<b>25.77</b>	52.63
Adjacent channel interference CIR (dB)	31.17	33.39
Adjacent satellite interference CIR (dB)	45.17	43.45
Cross-polar interference CIR (dB)	45.17	32.71
Total CIR (dB)	<b>24.41</b>	<b>22.71</b>
	Total link budget	
Total CIR (dB)	<b>20.46</b>	
System margin (dB)	0.50	
Net CIR (dB)	19.96	
Threshold CIR (dB)	16.50	
Excess margin (dB)	<b>3.46</b>	

# Bibliography

---

- [1] D. K. van Keuren. (2022) National Aeronautics and Space Administration (NASA) history. Moon in their eyes: Moon communication relay at the naval research laboratory, 1951-1962. [Online]. Available: <https://history.nasa.gov/SP-4217/ch2.htm>, last accessed on 27th Apr. 2022. (cit. on p. 2.)
- [2] L. C. Tillotson, “Active satellite repeaters: Interim report I,” in *TELSTAR I*, ser. NASA SP-32. United States. National Aeronautics and Space Administration (NASA) Technical Reports Server (NTRS), 1963, vol. 1, pp. 752–763. (cit. on p. 2.)
- [3] K. Tsiolkovsky, “Speculations about Earth and Sky and on Vesta,” *USSR Academy of Sciences, Moscow*, 1959 (first published in 1895 in Russian). (cit. on p. 2.)
- [4] H. Potočník, “Eine Warte im leeren Weltraum,” in *Das Problem der Befahrung des Weltraums: der Raketen-Motor*. Richard Carl Schmidt & Co., Berlin, 1929, pp. 96–100. (cit. on p. 2.)
- [5] A. C. Clarke, “Extra-terrestrial relays: Can rocket stations give world-wide radio coverage?” *Wireless World*, 1945, pp. 305–308. (cit. on p. 2.)
- [6] Syncom Projects Office, “Launch and orbital maneuvers,” in *Syncom Engineering Report*, ser. NASA TR R-233. United States. National Aeronautics and Space Administration (NASA) Technical Reports Server (NTRS), 1966, vol. 1, ch. 3, pp. 31–0. (cit. on p. 2.)
- [7] Intelsat. (2022) Our Story. [Online]. Available: <https://www.intelsat.com/about-us/our-story/>, last accessed on 27th Apr. 2022. (cit. on pp. 2 and 3.)
- [8] Telesat. (2022) Our History: 50 years of creating connections. [Online]. Available: <https://www.telesat.com/history/>, last accessed on 27th Apr. 2022. (cit. on pp. 2 and 3.)
- [9] Eutelsat. (2022) Our History: 40 years of innovation at the heart of a global satellite industry and vibrant digital economy. [Online]. Available: <https://www.eutelsat.com/en/group/our-history.html>, last accessed on 27th Apr. 2022. (cit. on p. 3.)
- [10] M. Wade. (2022) Gorizont. [Online]. Available: <https://web.archive.org/web/20080617211454/http://www.astronautix.com/craft/gorizont.htm>, last accessed on 27th Apr. 2022. (cit. on p. 3.)

- [11] SES. (2022) Our History Highlights. [Online]. Available: <https://www.ses.com/about-us/our-history-highlights>, last accessed on 27th Apr. 2022. (cit. on p. 3.)
- [12] SES. (2022) SES fact sheet on Astra 1A at 5.2° East (February 2003). [Online]. Available: <https://web.archive.org/web/20160304045343/https://es.ses-astra.com/18579787/1A-footprint-fact-sheet.pdf>, last accessed on 27th Apr. 2022. (cit. on p. 3.)
- [13] K. Spies and E. Haakinson, “Calculation of geostationary satellite footprints for certain idealized antennas,” in *NTIA-Report-80-51*, P. M. Klutznick, Ed. U.S. Department of Commerce, 1980. (cit. on pp. 3 and 5.)
- [14] D. J. Stephenson, “The linked budget calculation,” in *Newnes Guide to Satellite TV: Installation, Reception and Repair*, 2nd ed. Newnes, 1991, ch. 5, pp. 107–132. (cit. on p. 3.)
- [15] ITU. (2022) Radio Regulations. [Online]. Available: <https://www.itu.int/pub/R-REG-RR>, last accessed on 27th Apr. 2022. (cit. on p. 3.)
- [16] —, “Règlement de service annexé à la convention radiotélégraphique internationale,” *Documents de la Conférence radiotélégraphique internationale de Berlin*, 1906, [Online]. Available: <https://search.itu.int/history/HistoryDigitalCollectionDocLibrary/1.2.48.fr.200.pdf>, last accessed on 27th Apr. 2022. (cit. on p. 3.)
- [17] —. (2022) WARC ORB-85: World Administrative Radio Conference on the use of the geostationary-satellite orbit and the planning of the space services utilizing it (1st session) (Geneva, 1985). [Online]. Available: <http://handle.itu.int/11.1004/020.1000/4.111>, last accessed on 27th Apr. 2022. (cit. on p. 4.)
- [18] —, “Final Acts adopted by the first session of the World Administrative Radio Conference on the use of the geostationary-satellite orbit and the planning of space services utilizing it,” *IEEE Transactions on Communications*, 1986, [Online]. Available: <https://search.itu.int/history/HistoryDigitalCollectionDocLibrary/4.111.43.en.100.pdf>, last accessed on 27th Apr. 2022. (cit. on p. 4.)
- [19] G. Maral and M. Bousquet, “The communication payload,” in *Satellite Communications Systems: Systems, Techniques and Technologies*, 5th ed., ser. Wiley Series in Communication and Distributed Systems. Wiley, 2009, ch. 9, pp. 435–525. (cit. on pp. 4, 8, 35, 60, and 61.)
- [20] —, “Earth stations,” in *Satellite Communications Systems: Systems, Techniques and Technologies*, 5th ed., ser. Wiley Series in Communication and Distributed Systems. Wiley, 2009, ch. 8, pp. 363–434. (cit. on pp. 4 and 8.)



- [21] *Digital Video Broadcasting (DVB); Framing structure, channel coding and modulation for 11/12 GHz satellite services*, ETSI EN 300 421 V1.1.2, European Telecommunications Standards Institute (ETSI), August 1997, [Online]. Available: [https://www.etsi.org/deliver/etsi\\_en/300400\\_300499/300421/01.01.02\\_60/en\\_300421v010102p.pdf](https://www.etsi.org/deliver/etsi_en/300400_300499/300421/01.01.02_60/en_300421v010102p.pdf), last accessed on 27th Apr. 2022. (cit. on p. 4.)
- [22] J. Whelan, “Analog-FM vs. digital-PSK transmission,” *IEEE Transactions on Communication Technology*, vol. 14, no. 3, pp. 275–282, 1966. (cit. on p. 4.)
- [23] B. Battrick, “Satellite telecommunications – market perspectives and industrial situation,” *ESA JCB 2005 (18) Rev. 1*, 2005. [Online]. Available: <https://www.esa.int/esapub/br/br254/br254.pdf> (cit. on p. 4.)
- [24] Boeing Satellite System Inc. (2022) ANIK F2: Ka-band for North America. [Online]. Available: [https://web.archive.org/web/20050729092003/http://www.boeing.com/defense-space/space/bss/factsheets/702/anik\\_f2/anik\\_f2.html](https://web.archive.org/web/20050729092003/http://www.boeing.com/defense-space/space/bss/factsheets/702/anik_f2/anik_f2.html), last accessed on 27th Apr. 2022. (cit. on p. 4.)
- [25] D. Minoli, “High throughput satellites (HTS) and KA/KU spot beam technologies.” John Wiley & Sons, Inc., 2015, ch. 3, pp. 95–159. [Online]. Available: <https://onlinelibrary.wiley.com/doi/abs/10.1002/9781118984086.ch3> (cit. on pp. 4, 5, and 6.)
- [26] ITU, “ITU internet reports: The portable internet,” 2004, pp. A–1 – A–25, [Online]. Available: <http://handle.itu.int/11.1002/pub/800c7e3c-en>, last accessed on 27th Apr. 2022. (cit. on p. 4.)
- [27] *Digital Video Broadcasting (DVB) User guidelines for the second generation system for Broadcasting, Interactive Services, News Gathering and other broadband satellite applications (DVB-S2)*, ETSI TR 102 376 V1.1.1, European Telecommunications Standards Institute (ETSI), February 2005, [Online]. Available: [https://www.etsi.org/deliver/etsi\\_tr/102300\\_102399/102376/01.01.01\\_60/tr\\_102376v010101p.pdf](https://www.etsi.org/deliver/etsi_tr/102300_102399/102376/01.01.01_60/tr_102376v010101p.pdf), last accessed on 27th Apr. 2022. (cit. on p. 5.)
- [28] R. Jewett. (2022) Viasat completes purchase of Euro Broadband Infrastructure. [Online]. Available: <https://www.satellitetoday.com/broadband/2021/04/30/viasat-completes-purchase-of-euro-broadband-infrastructure/>, last accessed on 27th Apr. 2022. (cit. on p. 5.)
- [29] Viasat Inc. (2022) KA-SAT satellite: The KA-SAT satellite network provides internet coverage over much of Europe. [Online]. Available: <https://www.viasat.com/space-innovation/satellite-fleet/ka-sat/>, last accessed on 27th Apr. 2022. (cit. on p. 5.)
- [30] SatBeams. (2022) Footprints: 9°E — Eutelsat KA-SAT 9A (KASAT, KA-Sat). [Online]. Available: <https://www.satbeams.com/footprints?position=9>, last accessed on 27th Apr. 2022. (cit. on p. 5.)

- [31] H. Fenech, Amos, Tomatis, and Soumholphkaky, “KA-SAT and future HTS systems,” in *2013 IEEE 14th International Vacuum Electronics Conference (IVEC)*, 2013, pp. 1–2. (cit. on p. 5.)
- [32] X. Maufroid, F. Coromina, B.-M. Folio, H. Göckler, H. Kopmann, and M. N. Abdulazim, “High throughput bent-pipe processor for future broadband satellite access networks,” in *8th Int. Workshop on Sign. Proc. Space Commun.*, 2003, pp. 259–275. (cit. on pp. 5 and 7.)
- [33] P. Angeletti, G. Gallinaro, L. Hili, and X. Maufroid, “Evolution of analog to digital conversion technology for wideband space applications,” in *23rd AIAA International Communications Satellite Systems Conference 2005 (ICSSC)*. (cit. on p. 5.)
- [34] P. Angeletti, R. D. Gaudenzi, and M. Lisi, “From "bent pipes" to "software defined payloads": Evolution and trends of satellite communications systems,” in *26th International Communications Satellite Systems Conference 2008 (ICSSC)*. [Online]. Available: <https://arc.aiaa.org/doi/abs/10.2514/6.2008-5439> (cit. on p. 5.)
- [35] A. Le Pera, F. Forni, M. Grossi, M. Lucente, V. Palma, T. Rossi, and M. Ruggeri, “Digital transparent processor for satellite telecommunication services,” in *2007 IEEE Aerospace Conference*, 2007, pp. 1–9. (cit. on p. 5.)
- [36] C. Haardt, O. D. R. Herrero, and N. Alagha, “Semi-transparent packet switching by satellite: Migrating existing technologies for new opportunities,” in *26th International Communications Satellite Systems Conference (ICSSC)*, 2012. [Online]. Available: <https://arc.aiaa.org/doi/abs/10.2514/6.2008-5411> (cit. on p. 5.)
- [37] N. Venet, V. Enjolras, C. Nicolas, and P. Voisin, “Spaceflex onboard digital transparent processor: a new generation of DTP with optical digital interconnects,” in *International Conference on Space Optics — ICSSO 2018*, Z. Sodnik, N. Karafolas, and B. Cugny, Eds., vol. 11180, International Society for Optics and Photonics. SPIE, 2019, pp. 1597 – 1606. [Online]. Available: <https://doi.org/10.1117/12.2536074> (cit. on p. 6.)
- [38] SES. (2022) SES-17 Successfully Launched on Ariane 5. [Online]. Available: <https://www.ses.com/press-release/ses-17-successfully-launched-ariane-5>, last accessed on 27th Apr. 2022. (cit. on p. 6.)
- [39] M. Holmes. (2022) Eutelsat delays return to growth projection, Konnect VHTS pushed back to H2 2023. [Online]. Available: <https://www.satellitetoday.com/business/2022/02/17/eutelsat-delays-return-to-growth-projection-with-delays-to-konnect-vhts-and-10b-satellites/>, last accessed on 27th Apr. 2022. (cit. on p. 6.)

- [40] J. Rainbow. (2022) Lack of critical skilled workers delays first ViaSat-3 launch to late summer. [Online]. Available: <https://spacenews.com/lack-of-critical-skilled-workers-delays-first-viasat-3-launch-to-late-summer/>, last accessed on 27th Apr. 2022. (cit. on p. 6.)
- [41] Eutelsat. (2022) Future Satellites: Konnekt VHTS, Delivering high-speed broadband across Europe. [Online]. Available: <https://www.eutelsat.com/satellites/future-satellites.html>, last accessed on 27th Apr. 2022. (cit. on p. 6.)
- [42] Viasat Inc. (2022) ViaSat-3 satellite constellation: ViaSat-3 will offer global satellite broadband coverage and unprecedented capacity. [Online]. Available: <https://www.viasat.com/space-innovation/satellite-fleet/viasat-3/>, last accessed on 27th Apr. 2022. (cit. on p. 6.)
- [43] A. I. Perez-Neira, M. A. Vazquez, M. B. Shankar, S. Maleki, and S. Chatzinotas, “Signal processing for high-throughput satellites: Challenges in new interference-limited scenarios,” *IEEE Signal Processing Magazine*, vol. 36, no. 4, pp. 112–131, 2019. (cit. on p. 6.)
- [44] X. Lin and N. Lee, *5G and Beyond: Fundamentals and Standard*. Springer. (cit. on p. 6.)
- [45] 3GPP. (2022) Release 17. [Online]. Available: <https://www.3gpp.org/release-17>, last accessed on 27th Apr. 2022. (cit. on p. 6.)
- [46] ITU. (2022) Press Release: 2.9 billion people still offline. [Online]. Available: <https://www.itu.int/en/mediacentre/Pages/PR-2021-11-29-FactsFigures.aspx>, last accessed on 27th Apr. 2022. (cit. on p. 6.)
- [47] E. Yaacoub and M. Alouini, “A key 6G challenge and opportunity—connecting the base of the pyramid: A survey on rural connectivity,” *Proceedings of the IEEE*, vol. 108, no. 4, pp. 533–582, 2020. (cit. on p. 6.)
- [48] R. De Gaudenzi, P. Angeletti, D. Petrolati, and E. Re, “Future technologies for very high throughput satellite systems,” *Int J Satell Commun Network*, vol. 38, no. 2, pp. 141–161, 2020. [Online]. Available: <https://onlinelibrary.wiley.com/doi/abs/10.1002/sat.1327> (cit. on p. 6.)
- [49] F. Völk, R. T. Schwarz, M. Lorenz, and A. Knopp, “Emergency 5G communication on-the-move: Concept and field trial of a mobile satellite backhaul for public protection and disaster relief,” *International Journal of Satellite Communications and Networking*. [Online]. Available: <https://onlinelibrary.wiley.com/doi/abs/10.1002/sat.1377> (cit. on p. 6.)
- [50] O. Vidal, G. Verelst, J. Lacan, E. Alberty, J. Radzik, and M. Bousquet, “Next generation high throughput satellite system,” in *2012 IEEE First AESS European Conference on Satellite Telecommunications (ESTEL)*, 2012, pp. 1–7. (cit. on p. 7.)

- [51] H. Fenech, L. Roux, A. Hirsch, and V. Soumholphakdy, "Satellite antennas and digital payloads for future communication satellites: The quest for efficiencies and greater flexibility," *IEEE Antennas and Propagation Magazine*, vol. 61, no. 5, pp. 20–28, 2019. (cit. on p. 7.)
- [52] *Digital Video Broadcasting (DVB); Implementation guidelines for the second generation system for Broadcasting, Interactive Services, News Gathering and other broadband satellite applications; Part 2: S2 Extensions (DVB-S2X)*, ETSI TR 102 376-2 V1.2.1, European Telecommunications Standards Institute (ETSI), January 2021, [Online]. Available: [https://www.etsi.org/deliver/etsi\\_tr/102300\\_102399/10237602/01.02.01\\_60/tr\\_10237602v010201p.pdf](https://www.etsi.org/deliver/etsi_tr/102300_102399/10237602/01.02.01_60/tr_10237602v010201p.pdf), last accessed on 27th Apr. 2022. (cit. on pp. 8, 9, 24, 29, 31, 32, 36, 51, 65, 71, 73, and 74.)
- [53] T. M. Braun. John Wiley & Sons, Inc., 2012. (cit. on p. 8.)
- [54] A. E. Atia, "Wideband communication satellite payload architecture," in *2011 IEEE MTT-S International Microwave Symposium*, 2011, pp. 1–4. (cit. on p. 8.)
- [55] R. I. Cameron and M. Yu, "Design of manifold-coupled multiplexers," *IEEE Microwave Magazine*, vol. 8, no. 5, pp. 46–59, 2007. (cit. on pp. 8, 30, and 31.)
- [56] V. Singh, K. S. Parikh, S. Singh, and R. B. Bavaria, "DR OMUX for satellite communications: A complete step-by-step design procedure for the C-band dielectric resonator output multiplexer," *IEEE Microwave Magazine*, vol. 14, no. 6, pp. 104–118, 2013. (cit. on pp. 8 and 30.)
- [57] M. Kunes, "Microwave multiplexers for space applications," *Electronics Communication Engineering Journal*, vol. 10, no. 1, pp. 29–35, 1998. (cit. on p. 8.)
- [58] B. F. Beidas, "Adaptive digital signal predistortion for nonlinear communication systems using successive methods," *IEEE Transactions on Communications*, vol. 64, no. 5, pp. 2166–2175, 2016. (cit. on pp. 9, 33, and 57.)
- [59] O. B. Usman and A. Knopp, "Digital predistortion in high throughput satellites: Architectures and performance," *IEEE Access*, vol. 9, pp. 42 291–42 304, 2021. (cit. on p. 9.)
- [60] D. Leeson, "A simple model of feedback oscillator noise spectrum," *Proceedings of the IEEE*, vol. 54, no. 2, pp. 329–330, 1966. (cit. on p. 9.)
- [61] G. Maral and M. Bousquet, "Uplink, downlink and overall link performance; intersatellite links," in *Satellite Communications Systems: Systems, Techniques and Technologies*, 5th ed., ser. Wiley Series in Communication and Distributed Systems. Wiley, 2009, ch. 5, pp. 163–246. (cit. on p. 10.)
- [62] K.-U. Storek and A. Knopp, "Fair user grouping for multibeam satellites with MU-MIMO precoding," in *GLOBECOM 2017 - 2017 IEEE Global Communications Conference*, 2017, pp. 1–7. (cit. on p. 10.)

- [63] D. Serrano-Velarde, E. Lance, H. Fenech, and G. R-Guisantes, “A novel dimensioning method for high throughput satellite design,” in *2012 IEEE First AESS European Conference on Satellite Telecommunications (ESTEL)*, 2012, pp. 1–6. (cit. on p. 10.)
- [64] Rohde & Schwarz INRADIO GmbH, “R&S®GSASLP Satellite Link Planner,” [Online]. Available: [https://www.rohde-schwarz.com/us/about/overview/inradios/inradios\\_253348.html](https://www.rohde-schwarz.com/us/about/overview/inradios/inradios_253348.html), last accessed on 27th Apr. 2022. (cit. on p. 10.)
- [65] ST Engineering iDirect, “Satellite Network Calculator,” [Online]. Available: <https://www.idirect.net/products/satellite-network-calculator/>, last accessed on 27th Apr. 2022. (cit. on pp. 10 and 71.)
- [66] *Space engineering*, Communications, European Cooperation for Space Standardization (ECSS), March 2021. [Online]. Available: <https://ecss.nl/standard/> (cit. on p. 11.)
- [67] T. M. Braun, “Payload’s communications parameters,” in *Satellite Communications Payload and System*. John Wiley & Sons, Inc., 2012, ch. 7, pp. 181–205. (cit. on pp. 11, 30, and 31.)
- [68] N. Kasdin, “Discrete simulation of colored noise and stochastic processes and  $1/f^\alpha$  power law noise generation,” *Proceedings of the IEEE*, vol. 83, no. 5, pp. 802–827, 1995. (cit. on pp. 11 and 36.)
- [69] H. Schlemmer, J. Ebert, T. Taenzer, and W. Gappmair, “Some notes on phase noise generation and the impact on DVB-S2x waveforms,” in *2019 15th International Conference on Telecommunications (ConTEL)*, 2019, pp. 1–6. (cit. on p. 11.)
- [70] V. H. Rohit, Yogesh Prasad KR, V. Ravichandran, S. Sudhakar, S. Udupa, and N. Valarmathi, “Performance analysis of root raised cosine filtering in CCSDS ACM,” in *2016 International Conference on Wireless Communications, Signal Processing and Networking (WiSPNET)*, 2016, pp. 1750–1756. (cit. on p. 11.)
- [71] *Flexible Advanced Coding and Modulation Scheme For High Rate Telemetry Applications*, Blue Book, Issue 1, 131.2-B-1, Consultative Committee for Space Data Systems (CCSDS), March 2012, [Online]. Available: <https://public.ccsds.org/Pubs/131x2b1e1.pdf>, last accessed on 27th Apr. 2022. (cit. on pp. 11, 23, 24, 54, 93, and 94.)
- [72] L. Pilato, G. Meoni, and L. Fanucci, “Design and quantization limits of root raised cosine digital filter,” in *2017 3rd International Conference on Frontiers of Signal Processing (ICFSP)*, 2017, pp. 59–62. (cit. on p. 11.)
- [73] R. Bobilin and J. Lindenlaub, “Distortion analysis of binary FSK,” *IEEE Transactions on Communication Technology*, vol. 19, no. 4, pp. 478–486, 1971. (cit. on p. 12.)

- [74] R. L. Gobbi, “Intersymbol interference due to an ideal filter with linear amplitude attenuation,” in *IEEE Conference on Military Communications*, 1990, pp. 1276–1280 vol.3. (cit. on p. 12.)
- [75] W. S. Moreira and J. C. Brandao, “Effect of channel distortions in the performance of digital transmission systems with QAM modulation,” in *SBT/IEEE International Symposium on Telecommunications*, 1990, pp. 297–301. (cit. on p. 12.)
- [76] K. Metzger and R. Valentin, “Intersymbol interference due to linear and non-linear distortion,” *IEEE Transactions on Communications*, vol. 44, no. 7, pp. 809–816, 1996. (cit. on p. 12.)
- [77] R. Sadr, M. Shahshahani, and W. J. Hurd, “Degradation of signal-to-noise ratio due to amplitude distortion,” *IEEE Transactions on Information Theory*, vol. 35, no. 4, pp. 874–878, 1989. (cit. on p. 12.)
- [78] J. Jones, “Filter distortion and intersymbol interference effects on PSK signals,” *IEEE Transactions on Communication Technology*, vol. 19, no. 2, pp. 120–132, 1971. (cit. on pp. 12 and 42.)
- [79] S. Benedetto and E. Biglieri, “Nonlinear equalization of digital satellite channels,” *IEEE Journal on Selected Areas in Communications*, vol. 1, no. 1, pp. 57–62, 1983. (cit. on p. 12.)
- [80] B. F. Beidas, “Intermodulation distortion in multicarrier satellite systems: Analysis and turbo Volterra equalization,” *IEEE Transactions on Communications*, vol. 59, no. 6, pp. 1580–1590, 2011. (cit. on pp. 12 and 35.)
- [81] J. L. Pinto and I. Darwazeh, “Phase distortion and error vector magnitude for 8-PSK systems,” in *Proceedings of London Communications Symposium– LCS 2000*, pp. 14–15. (cit. on p. 13.)
- [82] T. Nakagawa and K. Araki, “Effect of phase noise on RF communication signals,” in *Vehicular Technology Conference Fall 2000. IEEE VTS Fall VTC2000. 52nd Vehicular Technology Conference (Cat. No.00CH37152)*, vol. 2, 2000, pp. 588–591 vol.2. (cit. on pp. 13 and 20.)
- [83] M. R. Khanzadi, D. Kuylenstierna, A. Panahi, T. Eriksson, and H. Zirath, “Calculation of the performance of communication systems from measured oscillator phase noise,” *IEEE Transactions on Circuits and Systems I: Regular Papers*, vol. 61, no. 5, pp. 1553–1565, 2014. (cit. on p. 13.)
- [84] T. Höhne and V. Ranki, “Phase noise in beamforming,” *IEEE Transactions on Wireless Communications*, vol. 9, no. 12, pp. 3682–3689, 2010. (cit. on pp. 13, 65, and 66.)



- [85] A. Georgiadis, “Gain, phase imbalance, and phase noise effects on error vector magnitude,” *IEEE Transactions on Vehicular Technology*, vol. 53, no. 2, pp. 443–449, 2004. (cit. on p. 13.)
- [86] C. Muschallik, “Influence of RF oscillators on an OFDM signal,” *IEEE Transactions on Consumer Electronics*, vol. 41, no. 3, pp. 592–603, 1995. (cit. on pp. 13 and 67.)
- [87] C. Shannon, “Communication in the presence of noise,” *Proceedings of the IRE*, vol. 37, no. 1, pp. 10–21, 1949. (cit. on p. 18.)
- [88] X. Maufroid, F. Coromina, B.-M. Folio, H. G. Göckler, H. Kopmann, and M. N. Abdulazim, “High throughput bent-pipe processor for future broadband satellite access networks,” in *Proc. 8th Int. Workshop on Signal Processing for Space Commun. (SPSC)*, 2003, pp. 259–275. (cit. on p. 19.)
- [89] D. Serrano-Velarde, E. Lance, H. Fenech, and G. R-Guisantes, “A novel dimensioning method for high throughput satellite design,” in *2012 IEEE First AESS European Conference on Satellite Telecommunications (ESTEL)*, 2012, pp. 1–6. (cit. on p. 19.)
- [90] R. Bi, M. Yang, and G. Wang, “Interference and link budget analysis in integrated satellite and terrestrial mobile system,” in *2018 International Symposium on Networks, Computers and Communications (ISNCC)*, 2018, pp. 1–6. (cit. on p. 19.)
- [91] L. Zheng and R. Gallager, “Random processes and noise,” in *6.450 Principles of Digital Communications I*. Massachusetts Institute of Technology: MIT OpenCourseWare, 2006, ch. 7, pp. 199–247. [Online]. Available: <https://ocw.mit.edu> (cit. on p. 23.)
- [92] J. Proakis and M. Salehi, “Digital communication through band-limited channels.” McGraw-Hill, 2008, ch. 9, pp. 604–639. (cit. on pp. 25, 29, and 89.)
- [93] —, “Digital communication through band-limited channels.” McGraw-Hill, 2008, ch. 2, pp. 74–76. (cit. on p. 27.)
- [94] A. V. Oppenheim and R. W. Schaffer, “Filter design techniques.” Pearson, 2014, ch. 7, pp. 557–564. [Online]. Available: <https://elibrary.pearson.de/book/99.150005/9781292038155> (cit. on p. 29.)
- [95] F. Li, J. Yang, and X. Yin, “High quality  $TE_{011}$  mode cavity filter for input multiplexer applications,” in *2018 48th European Microwave Conference (EuMC)*, 2018, pp. 101–104. (cit. on p. 30.)
- [96] M. Latif and A. U. Salfi, “Design of 5-channel C-band input multiplexer for communication satellites,” *Journal of Space Technology*, vol. V, no. 1, 2015. (cit. on p. 30.)

- [97] J. S. Galaz, A. P. del Pino, and P. M. Iglesias, “High order RF filters for communications satellite systems,” in *IWMF 2015 - 6th CNES/ESA International Workshop on Microwave Filters*, 2015. (cit. on p. 30.)
- [98] *Digital Video Broadcasting (DVB); Second generation framing structure, channel coding and modulation systems for Broadcasting, Interactive Services, News Gathering and other broadband satellite applications; Part 1: DVB-S2*, ETSI EN 302 307-1 V1.4.1, European Telecommunications Standards Institute (ETSI), July 2014, [Online]. Available: [https://www.etsi.org/deliver/etsi\\_en/302300\\_302399/30230701/01.04.01\\_60/en\\_30230701v010401p.pdf](https://www.etsi.org/deliver/etsi_en/302300_302399/30230701/01.04.01_60/en_30230701v010401p.pdf), last accessed on 27th Apr. 2022. (cit. on p. 31.)
- [99] R. J. Cameron, “General coupling matrix synthesis methods for Chebyshev filtering functions,” *IEEE Transactions on Microwave Theory and Techniques*, vol. 47, no. 4, pp. 433–442, 1999. (cit. on p. 31.)
- [100] C. Eun and E. Powers, “A new Volterra predistorter based on the indirect learning architecture,” *IEEE Transactions on Signal Processing*, vol. 45, no. 1, pp. 223–227, 1997. (cit. on p. 33.)
- [101] A. Saleh, “Frequency-independent and frequency-dependent nonlinear models of TWT amplifiers,” *IEEE Transactions on Communications*, vol. 29, no. 11, pp. 1715–1720, 1981. (cit. on p. 33.)
- [102] C. Rapp, “Effects of HPA-nonlinearity on a 4-DPSK/OFDM-signal for a digital sound broadcasting system,” *Proceedings Second European Conf. on Sat. Comm. (ESA SP-332)*, pp. 179–184, 1991. (cit. on p. 33.)
- [103] B. F. Beidas, R. I. Seshadri, and N. Becker, “Multicarrier successive predistortion for nonlinear satellite systems,” *IEEE Transactions on Communications*, vol. 63, no. 4, pp. 1373–1382, 2015. (cit. on p. 35.)
- [104] L. Piazzo and P. Mandarini, “Analysis of phase noise effects in OFDM modems,” *IEEE Transactions on Communications*, vol. 50, no. 10, pp. 1696–1705, 2002. (cit. on p. 36.)
- [105] D. D. Lin and T. J. Lim, “The variational inference approach to joint data detection and phase noise estimation in OFDM,” *IEEE Transactions on Signal Processing*, vol. 55, no. 5, pp. 1862–1874, 2007. (cit. on p. 36.)
- [106] T. Tänzer, “Efficient implementation and analysis of different phase noise generation methods for DVB-S2x waveforms,” Master’s thesis, Institute of Communication Networks and Satellite Communications, Graz University of Technology, Austria, 2018. (cit. on p. 36.)
- [107] C. A. Hofmann and A. Knopp, “Phase noise limits in low-rate communication via satellite,” *IEEE Internet of Things Journal*, pp. 1–1, 2021. (cit. on p. 36.)



- [108] B. M. Shankar, R. Piazza, and S. Cioni, “On-ground signal processing techniques enabling efficient amplification of multicarriers,” in *Cooperative and Cognitive Satellite Systems*. Academic Press, 2015, ch. 4, pp. 119–153. (cit. on p. 48.)
- [109] V. Volterra, *Sopra le funzioni che dipendono da altre funzioni*. Tipografia della R. Accademia dei Lincei, 1887. (cit. on p. 54.)
- [110] M. Abramowitz and I. Stegun, “Elementary analytical methods,” ser. Applied mathematics series. Dover Publications, 1972, ch. 3, pp. 17–18. (cit. on p. 56.)
- [111] A. Mallet, A. Anakabe, J. Sombrin, R. Rodriguez, and F. Coromina, “Multi-port amplifier operation for Ka-band space telecommunication applications,” in *2006 IEEE MTT-S International Microwave Symposium Digest*, 2006, pp. 1518–1521. (cit. on p. 56.)
- [112] F. Raab, P. Asbeck, S. Cripps, P. Kenington, Z. Popovic, N. Potheary, J. Sevic, and N. Sokal, “Power amplifiers and transmitters for RF and microwave,” *IEEE Transactions on Microwave Theory and Techniques*, vol. 50, no. 3, pp. 814–826, 2002. (cit. on p. 57.)
- [113] A. Saleh, “Intermodulation analysis of FDMA satellite systems employing compensated and uncompensated TWT’s,” *IEEE Transactions on Communications*, vol. 30, no. 5, pp. 1233–1242, 1982. (cit. on p. 57.)
- [114] R. Khanzadi, “Phase noise in communication systems: Modeling, compensation, and performance analysis,” Ph.D. dissertation, Chalmers University of Technology, Göteborg, Sweden, November 2015, ch. 3, p. 15. (cit. on p. 65.)
- [115] A. Chorti and M. Brookes, “A spectral model for RF oscillators with power-law phase noise,” *IEEE Transactions on Circuits and Systems I: Regular Papers*, vol. 53, no. 9, pp. 1989–1999, 2006. (cit. on pp. 65 and 66.)
- [116] M. Abramowitz and I. Stegun, “Elementary analytical methods,” ser. Applied mathematics series. Dover Publications, 1972, ch. 3, p. 11. (cit. on p. 67.)
- [117] S.-Y. Lien, S.-L. Shieh, Y. Huang, B. Su, Y.-L. Hsu, and H.-Y. Wei, “5G new radio: Waveform, frame structure, multiple access, and initial access,” *IEEE Communications Magazine*, vol. 55, no. 6, pp. 64–71, 2017. (cit. on p. 70.)
- [118] (2022) Yahsat 1b. [Online]. Available: <https://spaceflight101.com/spacecraft/yahsat-1b/>, last accessed on 27th Apr. 2022. (cit. on p. 71.)
- [119] (2022) Al Yah 2. [Online]. Available: <https://www.yahsat.com/en/about-yahsat/our-fleet>, last accessed on 27th Apr. 2022. (cit. on p. 71.)
- [120] I. Katzela and M. Naghshineh, “Channel assignment schemes for cellular mobile telecommunication systems: a comprehensive survey,” *IEEE Personal Communications*, vol. 3, no. 3, pp. 10–31, 1996. (cit. on p. 79.)

- [121] D. J. Goodman, S. A. Grandhi, and R. Vijayan, “Distributed dynamic channel assignment schemes,” in *IEEE 43rd Vehicular Technology Conference*, 1993, pp. 532–535. (cit. on p. 80.)
- [122] S. A. Grandhi, R. D. Yates, and D. J. Goodman, “Resource allocation for cellular radio systems,” *IEEE Transactions on Vehicular Technology*, vol. 46, no. 3, pp. 581–587, 1997. (cit. on p. 80.)
- [123] E. L. Lawler, *Recent Results in the Theory of Machine Scheduling*. Berlin, Heidelberg: Springer Berlin Heidelberg, 1983, pp. 202–234. (cit. on p. 80.)
- [124] G. B. Arfken, H. J. Weber, and F. E. Harris, “Complex variable theory,” in *Mathematical Methods for Physicists*, 7th ed. Academic Press, 2013, ch. 11, pp. 469–550. [Online]. Available: <https://www.sciencedirect.com/science/article/pii/B9780123846549000116> (cit. on p. 92.)
- [125] M. Abramowitz and I. Stegun, *Handbook of Mathematical Functions: With Formulas, Graphs, and Mathematical Tables*, ser. Applied mathematics series. Dover Publications, 1972. (Not cited.)
- [126] J. Proakis and M. Salehi, *Digital Communications*, 5th ed. McGraw-Hill, 2008. (Not cited.)
- [127] G. Maral and M. Bousquet, ser. Wiley Series in Communication and Distributed Systems. Wiley, 2009. (Not cited.)